Mixing and Deposition in a Jack Pine Forest Canopy

Kaiti Jiang

A Thesis submitted to the Faculty of Graduate Studies
in Partial Fulfillment of the Requirements for the
Degree of Master of Science

Graduate program in Earth and Space Science, York University
Toronto, Ontario

January 2, 2019

Abstract

To study how aerosols mix and deposit to forests, a tower was erected in a jack pine forest as part of the York Athabasca Jack Pine project. The tower is surrounded by anthropogenic pollution sources from the Alberta Oil Sands operations.

From previous studies, we expected that canopies inhibit mixing and deposition. During the study, the air within the forest was often decoupled from the air above. Mixing at the study site took up to 40 minutes during periods where the canopy was decoupled, compared to less than 2 minutes when the canopy was coupled.

At different times during the campaign, the forest was either a sink or a source of aerosols. The mean aerosol deposition velocity, an important parameter used by deposition models, was measured in this boreal forest. A local minimum of v_d (with respect to particle diameter) of 0.16 cm/s was observed at D = 150 nm.

Acknowledgements

It is a maxim in the discipline of geography that "people make places". Without people, locations are just coordinates on a map, void of any sense of place. Only with people are they ascribed meaning, and only with meaning do they come alive and become places in one's life.

It is just as true that places, in turn, make people. My time at York University has not only made me a better researcher, but also a more prudent and sociable person. As I move on from this place, I would like to thank those who shared in its making and our being made.

To Zheng Qi Wang and Brandon Taylor, without whom this manuscript would have been completed two months earlier; and to Stefan Miller, without whom it would have been completed even later. To my supervisor Mark Gordon, whose youthful ambition, enthusiasm, and brilliance contrasted with mature patience and understanding; to my co-supervisor Ralf Staebler, whose close eye and sharp mind guided the project on issues big and small; and to my committee member Peter Taylor, whose vast reservoir of experience and knowledge significantly enriched not only this thesis but also my time at York.

These, and many others, helped make York University a place where I grew as a scientist. May you too, dear reader, make your place to shine.

Contents

List of Figures

List of Tables

Symbols and Conventions

Bo	Bowen ratio
c	Speed of sound
C	Concentration
$Co(.)$	Cospectrum
c_p	Heat capacity of air at constant pressure
c_v	Heat capacity of air at constant volume
d	Sonic anemometer path length
D	Particle diameter
D_M	Brownian diffusion coefficient
e	Partial pressure of water vapour
f	Frequency
F	Flux
F_r	Uncorrected flux
F_s	Storage flux
H	Sensible heat flux
h_c	Canopy height
$Im(.)$	Imaginary part
L	Latent heat of vaporisation of water
m	Water vapour mixing ratio
M	Molar mass
n	First zero crossing of R_F
P	Pressure
q	Specific humidity
R	Universal gas constant
$Re(.)$	Real part
R_F	Autocorrelation function for aerosol flux
R_w	Gas constant for water vapour
S	Source or sink
$S(f)$	Spectral density
t	Time
T	Temperature
T_a	Averaging period
T_s	Sonic temperature

T_v	Virtual temperature
u	Wind speed
v_d	Deposition velocity
v_g	Gravitational settling velicity
V_l	Component of wind along an axis
w	Vertical wind velocity
z	Height
z_r	Measurement height
γ	c_p/c_v
ϵ	Standard error
κ	Wavenumber
θ	Potential temperature
σ	Standard deviation
τ	Time lag
[a,b]	Set of real numbers a $\leq$ x $\leq$ b
[.]	Concentration
[.]	Units of
$\hat{.}$	Discrete Fourier transform
$.\cdot.$	Schur product
$\bar{.}$	Time average
.'	Fluctuation from the mean
.U.	Union of two sets
$00:00$	Times are local time respecting daylight savings, UTC-6

1 Background

Forests comprise 9% of the land surface on Earth (Adams, 2012) and 40% of the land surface of Canada (Canadian Council of Forest Ministers). Given the importance of forests in several biogeochemical cycles, such as the water cycle, the carbon cycle, and the radiation budget, there have been many experiments measuring fluxes over forests and measuring their contributions to these quantities.

For example, in Jarvis et al. (1997), the seasonal and annual fluxes of energy, carbon, and water were measured in a boreal forest, the forest biome which comprises 55% of Canada's forested area (La Roi, 2013). Using the technique of eddy-covariance (described in **Section 3.2**), they established a balance of energy, water, and carbon in a Saskatchewan boreal forest comprised of black spruce, jack pine, tamarack, and aspen. Also, Baldocchi et al. (1997) conducted a study in a boreal forest during the growing season of 117 days in 1994. The forest, also located in Saskatchewan, was predominantly jack pine. Using soil sensors, radiation sensors, and eddy covariance instruments, they established a water and energy budget for this jack pine forest.

Forests also pose special challenges to scientists who study turbulence and mixing. Crown elements modify the turbulence in canopies. The effects are well known. In Finnigan (2000), an ideal energy spectrum (see **Section 3.10**) with canopy effects is presented in **Figure 1.1** (his figure 14). In addition to a prominent peak of shear production at the canopy height, there is an inflection point due to wake and waving production of turbulence kinetic energy, the so-called "spectral short-cut" whereby the leaves and branches in the canopy convert lower frequency eddies to higher frequency eddies.

Even though there has been much progress made on characterising flow within canopies (a review can be found in Finnigan 2000), currently, the turbulent properties and

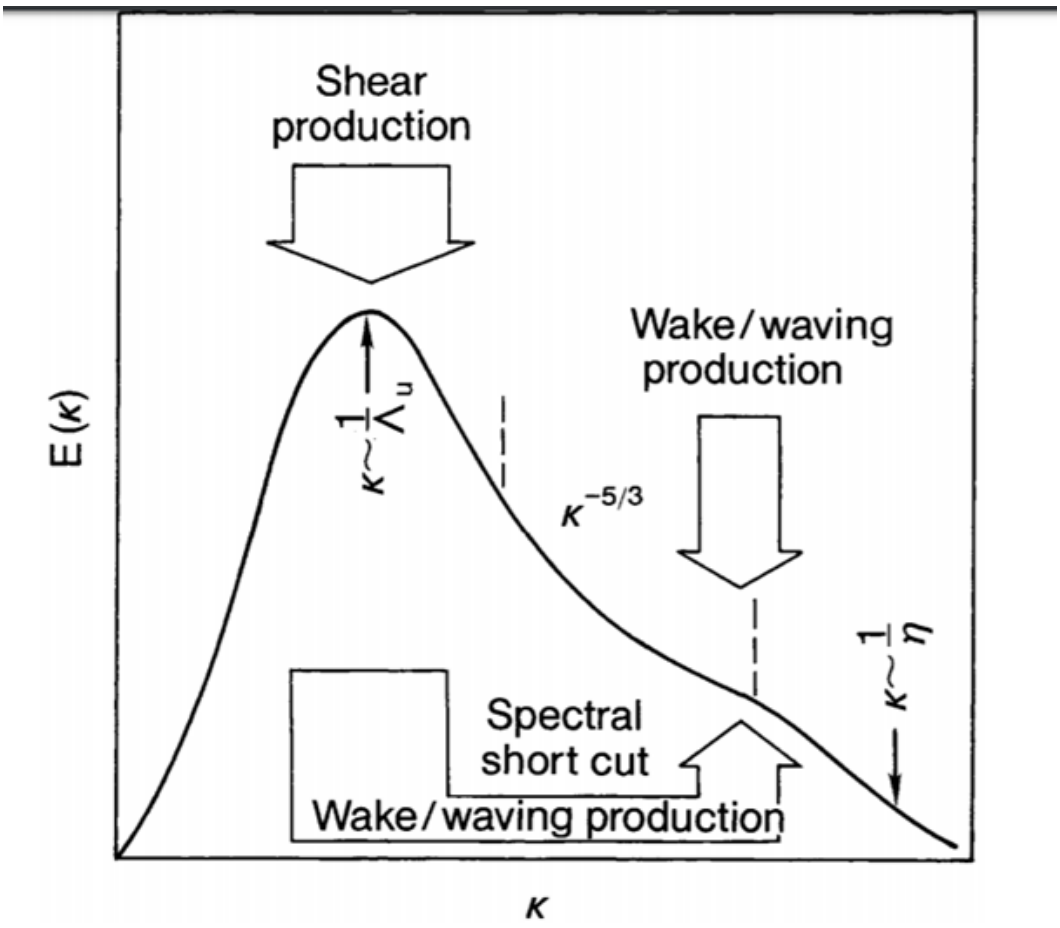

Figure 1.1: Reproduced from figure 14 in Finnigan (2000). An idealised schematic of the energy spectrum in a forest canopy.

structures within a forest are not completely described. For example, several spectra and cospectra, including those of potential temperature and heat flux, are yet to be completely characterised (Kaimal and Finnigan, 1994).

As well, observations and models of aerosol deposition and dispersion within the canopy do not match well (Petroff et al., 2008a). The primary mechanism for the deposition of small particles < 100 nm in diameter is Brownian diffusion, which is more effective for smaller particles (Hicks et al., 2016). The primary mechanism for the deposition of large particles > 300 nm in diameter is impaction and interception due to inertia. There

is an intermediate size of particles for which neither mechanism is effective, leading to the local minimum of deposition velocity of aerosols with respect to particle diameter (ibid). Hicks et al. note that a prominent "well" present in models of deposition velocity of aerosols to forests, an important parameter in models of aerosol deposition given by $v_d = F/C$ (where F is flux and C is concentration), has eluded almost all experiments' observations. Petroff et al. (2008a) suggest that more observations of aerosol deposition in canopies are needed to resolve this discrepancy.

The presence of the crown of a forest canopy leads to frequent decoupling between the sub-canopy space and the free atmosphere - only occasionally (an average of 4 hours per day) does the sub-canopy air exchange energy and matter with the free atmosphere (Thomas and Foken, 2007), and mixing often does not occur for several hours at a time. The canopy is usually decoupled during calm conditions (ibid). Decoupling means that fluxes in and out of forests do not happen continuously but are discrete events (Foken, 2008).

The existence of distinct aerosol growth episodes in forests has also recently been discovered. These episodes consist of the growth of aerosols from the nucleation mode $\tilde{2}$-3 nm to a size around 50 nm over the course of a day. Some hypotheses have been put forth as to the cause of these episodes. For example, in Nilsson et al. (2001), it is proposed that during periods of high background particle concentration, there is competition for limited amounts of precursor chemicals by large background particles. This was examined and tested by Allan et al. (2006), who used aerosol measurements gathered in Finland to show that the growth of biogenic aerosols happens solely when there is advection of clean air and not when there is advection of polluted air. They concluded that the larger particles present in the polluted air collect more precursor gases, leaving less to condense onto smaller particles.

In addition to studies characterizing the turbulent

structures and general chemistry inside forests, there have been several studies on the deposition of aerosols to forests. Deposition of aerosols to forest canopies is important because aerosol deposition depletes the air of aerosols, lowering the concentration of aerosols observed downstream. Also, aerosol deposition to forests affects the health and growth of the forest (Matsuda, 2017). Finally, parallels have been drawn as well between aerosols in forest canopies and aerosols in urban canopies (Petroff et al., 2008b). Therefore, studying the deposition of aerosols to forests will support research on the deposition of aerosols to urban canopies.

Gordon et al. (2011) described two field campaigns in 2006 and 2009 over a mixed forest in Borden (Ontario). Eddy covariance flux measurements (see **Section 3.2** for details of the eddy covariance method) were made using a fast mobility particle sizer (FMPS) particle counter, which operates by electrically charging a particle and placing it in a magnetic field. The instrument offers size-resolved measurements of particles between 6 and 560 nm at 1 Hz frequency.

In the study, it was discovered that 60% of all particle fluxes were upward, indicating a source of aerosols within the canopy hypothesized to be biogenic in origin. During dry periods, the portion of upward fluxes was even higher. Using the previous data, as well as particle concentration data at ground level, they concluded that the trunk space is decoupled from above at night, leading to a storage of aerosols and precursor chemicals. As a result, the size of particles grows though the night. Then, the air mixes during the day, creating an upward flux. In other words, upward fluxes of particles in forests are frequently due to the occasional dilution of particle-rich forest air with clean air from above.

Pryor et al. (2013) described another eddy-covariance experiment, at 25 m in a Colorado pine forest. Using an FMPS capable of detecting and size-resolving particles 6 to 560 nm,

flux into and out of the canopy was determined by the technique of eddy covariance. They also used a pulley system to determine the distribution of particle number distribution by height and size.

Like Gordon et al. (2011), Pryor et al. (2013) found that upward fluxes were present a significant portion of the time. Due to turbulence, the largest fluxes occurred during the daylight hours. In their forest site, upward fluxes were dominated by downward "sweeps" of clean air rather than upward "ejections" of particle-rich air. Sweeps correspond to clean air coming down. Pryor et al. usually observed them in the morning. Correspondingly, ejections correspond to particle-rich air rising out of the canopy and usually occurred in the afternoon. Ejections were observed to be mainly comprised of newly-formed biogenic aerosols and old aerosols containing new biogenic matter.

Through the pulley measurements of particle concentration, it was determined that smaller particles (ca. 12-18 nm in diameter) were in greater concentration above the canopy than below. That is, on average, the number of particles 12-18 nm at ground level was 70% of that above the canopy. The difference between the concentration of larger partcles above and below the canopy was not as great as it was for the smaller particles.

Ahlm et al. (2010) describes eddy covariance measurements made during the wet season at a height of 53 m, in the Amazon rainforest of Brazil. It was found that small particles and medium sized particles (below 500 nm) are almost exclusively deposited. Fluxes of large particles were sometimes upward, especially when clean air was advected over the forest. This indicated that small particles were deposited into the forest, and large particles were being produced in the forest and emitted. It is also possible that these larger particles are formed out of smaller ones. However, it is claimed that these particles are likely to be biogenic in origin due to their being

composed mainly of organic matter. It was also found that there was a correlation of upward fluxes with wind speed, but Ahlm et al. could not determine if this was because of a biological response to higher wind speeds (ejections) or enhanced mixing (sweeps).

In addition to the experiments in the Americas, observations of aerosol flux have also been made in Scandinavia through the BIOFOR experiment (Biogenic aerosol formation in the boreal forest), located at SMEAR II (Station for Measuring Forest Ecosystem–Atmosphere Relation) station (Kulmala et al., 2001). At the station, a 23–m tall eddy covariance tower (among other meteorological instruments) was set up in the boreal pine forests near Hyytiala, Finland. Air quality instruments such as particle counters and aerosol spectrometers were mounted on the tower.

Over the course of several BIOFOR campaigns, many aerosol nucleation events were observed, especially when the air advected into the experiment was from the north. The north was a sector with no anthropogenic activities and sparse particle concentrations. During these aerosol nucleation events, which occurred about 50 days per year, aerosols formed from biogenic particles (Allan et al., 2006) and grew from the nucleation mode to the Aitken mode, about 40 nm, at a growth rate of approximately 2 to 3 nm/h in diameter. These events are important because they are responsible for the growth of small particles to sizes where they can serve as, for example, cloud condensation nuclei (ibid).

Reviews of aerosol deposition to canopies are given in Petroff et al. (2008b) and in Hicks et al. (2016). Several models and observations of the deposition velocity of aerosols over different canopies are presented. The deposition velocity relates fluxes and concentration gradients and is given by $v_d = -F/C$, where F is the flux and C is the concentration. It was shown that over different canopies and for different particle diameters, observed deposition velocity varied by three orders of

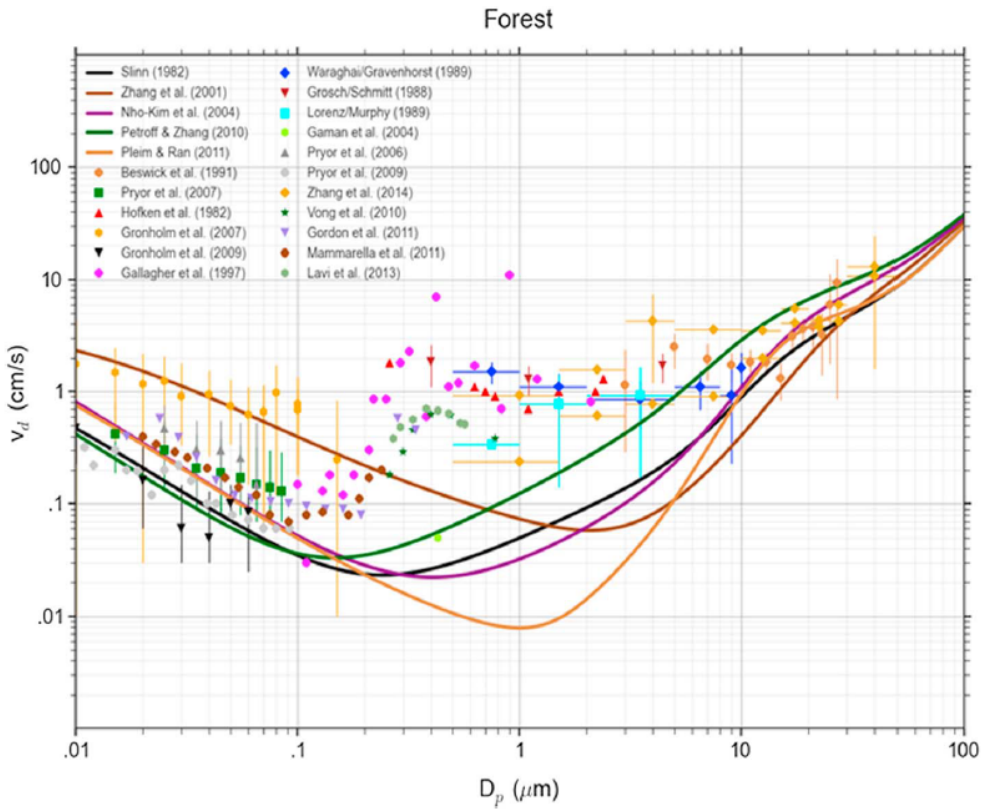

Figure 1.2: Reproduced from figure 7 in Hicks et al. (2016). Measurements and models of v_d of particles of different diameters in forest canopies. While models agree that the deposition velocity of aerosols has a local minimum with respect to particle diameter, only one study has observed this phenomenon.

magnitude. For forest canopies, models predicted a local minimum of deposition velocity with respect to aerosol particle diameter (ibid). The increase in deposition velocity at the lower size range is due to many factors, the most important of which is Brownian diffusion, the effect of which can be expressed by the viscosity of the air and the depth of the laminar layer of air on leaf surfaces (Hicks et al., 2016). However, Petroff et al. (2008b) noted that no single study had observed this minimum.

Since then, the minimum in deposition velocity has been observed in a coniferous forest in Southern Finland by Mammarella et al. (2011). Condensational particle counters and sonic

anemometers collected 5 years of size-resolved aerosol flux data. Local minima of aerosol deposition velocity with respect to particle diameter were observed at diameters 90 nm and 150 nm. The average deposition velocities in these bins were 1.8 mm/s and 1.9 mm/s, respectively.

Despite the Mammarella et al. study, Hicks et al. (2016) note that observations of the well are still rare. Models and observations of aerosol deposition velocity in different forests are summarised in their figure 7 (here reproduced as **Figure 1.2**). It can be seen in the figure that almost all models predict the minimum in deposition velocity, yet very few studies have observed it. Hicks et al. encouraged more measurements of deposition velocity of aerosols to a variety of forest canopies.

An aerosol flux experiment that reported deposition velocities took place in a young Douglas fir forest in The Netherlands. Gallagher et al. (1997) describes a summer 1995 experiment consisting of eddy covariance particle flux measurements at 25 m. They found comparatively large deposition velocities on the order of 1 cm/s for particles of size around 1 μm. Their measurements of deposition velocity vs. particle size corresponded well with theoretical predictions (eg. Sehmel and Hodgson, 1978) in the larger size ranges: the deposition velocity approached the terminal settling velocity as particles increased in size, and the decrease in deposition velocity became less steep as particle size decreased. However, they were unable to observe the increase in deposition velocity predicted by models at particle diameters of less than 200 nm.

It was also found in the study, as predicted (ibid), that there was a strong dependence of deposition velocity on stability. Deposition velocity of aerosols was higher during unstable periods and lower during stable periods. For large particles, it was hypothesized that, due to the increased turbulent kinetic energy in periods of high instability, particles had more momentum to deposit onto rough surfaces.

The studies discussed above demonstrate that forests play an important role in many processes, including aerosol deposition. While forests are usually a sink for aerosols, forests can often be a source of aerosols to the atmosphere, either by adding biogenic mass to anthropogenic aerosols or by aggregation of organic matter. Furthermore, the influence of mixing and coupling on deposition is often significant.

As this brief survey of eddy-covariance aerosol flux studies over forests has shown, aerosol flux over forests has been extensively studied in many environments. In spite of the abundance of aerosol flux studies, there has not yet been such a study in the Oil Sands region, even though the industrial operations in the area have been shown to produce as many secondary organic aerosols as a large city (Liggio et al., 2016). It is therefore of importance to characterise the physical and chemical processes that govern the deposition and evolution of these plumes.

The goal of the York Athabasca Jack Pine (YAJP) project is thus to characterize the deposition of anthropogenic emissions into forests and the effect the forest has on the mixing of aerosols and gases. Previous studies in the geographical area have been investigated the contributions of Oil Sands operations to pollution in the region, finding that the industry was a large source of polycyclic aromatic compounds (Kelly et al., 2009) and elements such as Al, K, S, Ti, and V (Addison and Puckett, 1980). However, aerosol flux studies in the regions have been limited to aircraft measurements of individual plumes (e.g. Liggio et al., 2016; Gordon et al., 2015); the YAJP experiment would be illustrative in the specifics of aerosol deposition to the forests and their evolution inside the canopy, as well as longer-term, inter-plume aerosol dynamics in the region.

The site selection is paramount and is analysed in the following section. A summary of the YAJP site and the scientific instruments deployed are then presented. Next, we introduce the

theoretical tools used in the analysis. Some general properties of our site are shown. Then, mixing of gases and tracers in the canopy is explored. Finally, we discuss the interaction between aerosols and the canopy. We conclude with a summary of results and suggestions for future projects.

2 Methods

2.1 Determination of pollution sources

To assist with site selection, it is helpful to determine the emission sources in the area. While we can predict emission sources from the locations of industrial operations and urban centres (**Figure 2.1**), these should be confirmed by data. For this, we used the network of air quality monitoring stations in the area run by the Wood Buffalo Environmental Association (WBEA

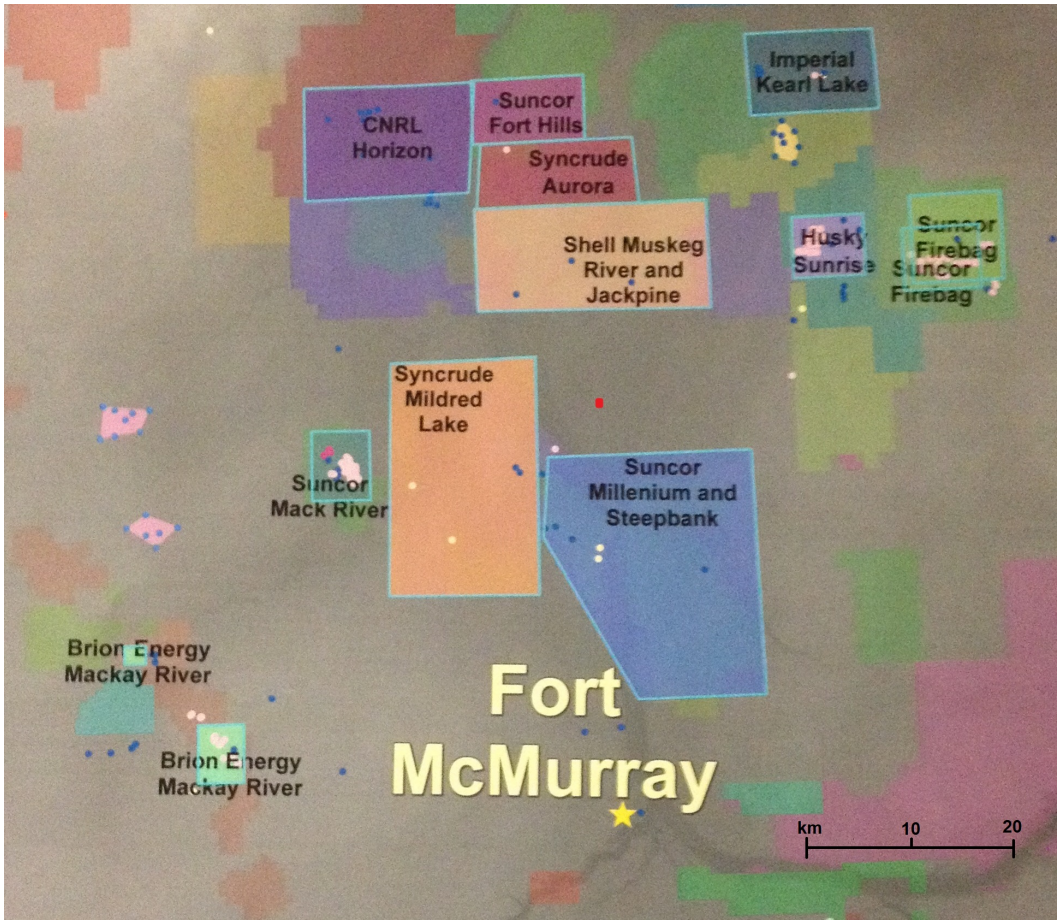

Figure 2.1: Industrial operations in the oil sands area as of 2017. Red dot in centre is the location of the site ultimately selected. Muskeg River and Jackpine are now operated by CNRL. Map from Environment and Climate Change Canada.

2018) and examined the historical data for median particulate concentration by wind direction.

For example, consider site AMS 13 (WBEA 2018). The median particulate matter binned by wind direction (**Figure 2.2**) shows a large source to the south of the station, and possibly to the southeast. Repeating this for the stations that have both air quality and wind direction data, a map of the emissions sources in the area was created (**Figure 2.3**). Angles with elevated values of PM2.5 are delimited by black lines on the map. Polygons indicate likely emission sources, which are based on these angles and the emissions inventory given in (ECCC 2016). The sizes of the polygons represent the possible area where emissions sources could be located, based on the location of mines and smokestacks on satellite imagery.

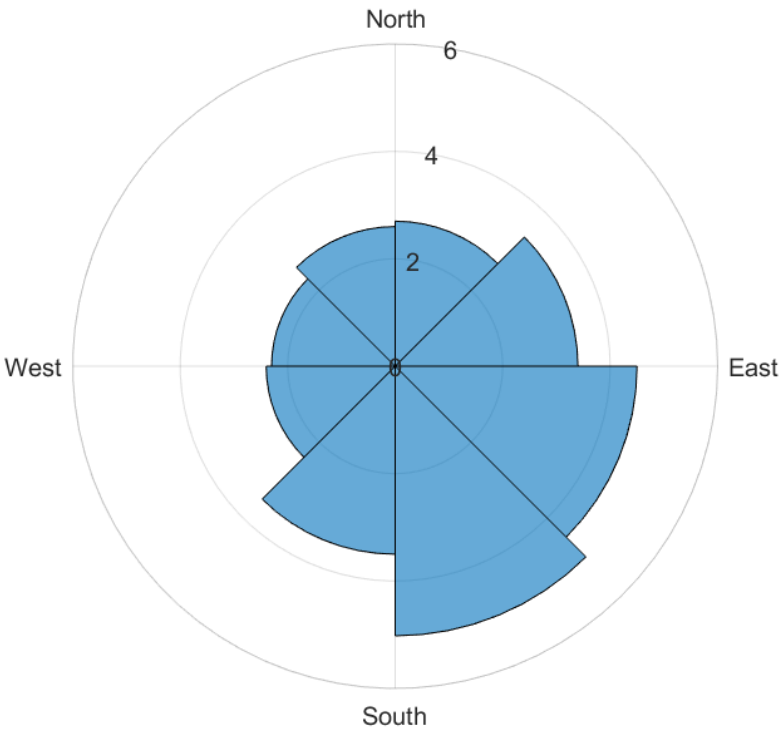

Figure 2.2: Median PM2.5 concentrations from AMS 13 site [µg/m ^{3}], binned by wind angle.

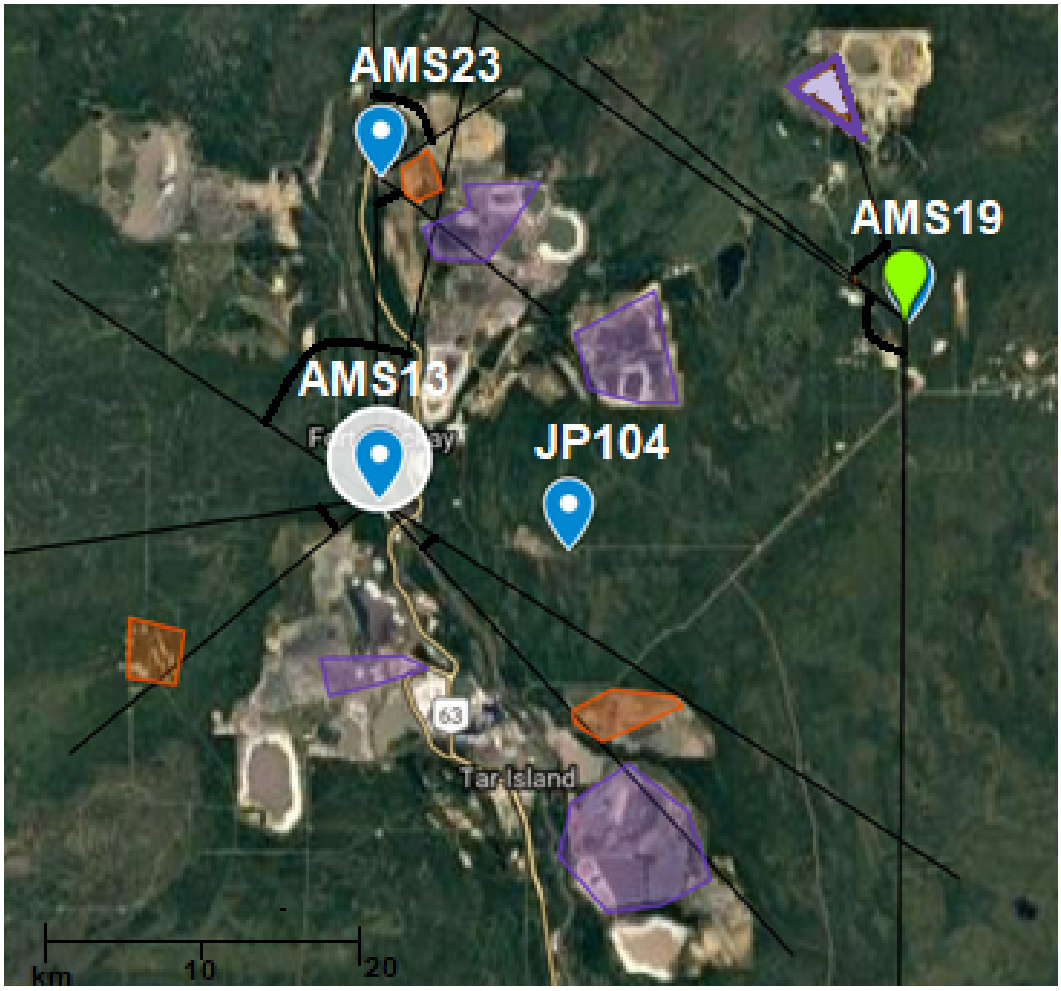

Figure 2.3: Emission sources in the oil sands area. Purple polygons indicate emission sources. Orange polygons indicate possible sources which emit low amounts of particulates. These were determined by the emissions inventory in (ECCC 2016) and analysis from the WBEA data. Blue pointers indicate WBEA towers used in analysis. Blue pointer with a white circle around it is AMS 13. Black lines delimit angles with elevated particulate concentrations; such angles lay in the sector with an arc. Site coordinates are given in the **Appendix**.

2.2 Site selection and clean-air/polluted-air statistics

In selecting the site for our study, we had to consider that we would have a limited time during the campaign to collect aerosol deposition and mixing data. During this time, we will need to sample both clean air and polluted air. Thus, the site selected for the tower should have periods of both polluted air and clean air so as to maximise the chances of having enough data to compare against each period. It should have sufficient fetch in a homogeneous forest, or eddy covariance would not produce results representative of the forest. Finally, the site must be accessible by truck, or we would not be able to transport our tower to the site.

To assist in site selection, it is useful to determine the probability of getting clean or polluted air at all points in a region. In the Athabasca region, there is a network of meteorological towers that provide hourly wind data (WBEA 2018). I developed a technique using these data, which can be used to create a stochastic back-trajectory model. Using a grid area with pollution sources at certain grid points, we can construct a transition matrix corresponding to the wind rose at each grid point. (For an introduction to stochastic modelling see Ross, 2014; Cinlar, 1975; or many other texts.)

At each step, the model traces back a parcel of air to an adjacent cell with probabilities given by wind direction data. This is done by multiplying a transition matrix (a matrix of probabilities) by itself. Once the parcel of air traces to a pollution source, it is deemed "polluted" and moved to a persistent state. Similarly, if the parcel of air traces off the grid, it is deemed "clean" and moved to a different persistent state. A sufficient number of steps are taken such that all air is determined to be either "polluted" or "clean". The percentages of air that is "clean" or polluted" are taken as an estimate of the probabilities of clean and polluted air at a grid point.

The (k,p) entry of the transition matrix is determined based on wind direction data from the closest data source. **Figure 2.4** illustrates the physical meaning of the entries of the transition matrix. One limitation of this model is that it assumes that the wind direction changes with a timescale of approximately the time it takes for the air to move one grid point. Care must therefore be exercised in selecting the grid resolution. A time scale for wind directions should be established. This, along with the mean wind speed, should be considered in determining the grid resolution such that one step roughly corresponds to the amount of time it takes for the wind to be stochastic at each step.

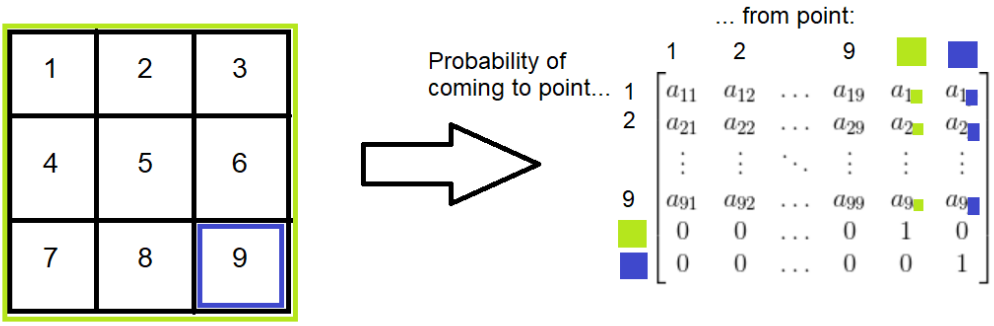

Figure 2.4: Partitioning of the grid in the example in **Section 2.2**, and the meaning of the entries in the transition matrix. Green represents the clean state; purple represents the polluted state.

To illustrate the procedure, let us use an example of a 3 x 3 grid with one pollution source at grid point (3,3), depicted in **Figure 2.4**. Therefore, any parcel of air that passes through (3,3) is polluted, and any parcel of air that exits the grid area without passing through (3,3) is clean. Suppose the grid point we consider is (2,2), and suppose that the wind rose in the area is uniform and isotropic. Then, there is a 1/8 probability that the air will come to (2,2) directly from (3,3). However, there is also a possibility that the air reaching (2,2) could be polluted already by passing through (3,3).

To determine the sum of these probabilities, we use the

method described above. We number the grid points 1 – 9, as in **Figure 2.4.** We construct a matrix where the entry a_{kp} is the probability that the air came to grid point k from grid point p. The matrix constructed in this case would be:

$$\begin{bmatrix} 0 & 1/8 & 0 & 1/8 & 1/8 & 0 & 0 & 0 & 0 & 5/8 & 0 \\ 1/8 & 0 & 1/8 & 1/8 & 1/8 & 1/8 & 0 & 0 & 0 & 3/8 & 0 \\ 0 & 1/8 & 0 & 0 & 1/8 & 1/8 & 0 & 0 & 0 & 5/8 & 0 \\ 1/8 & 1/8 & 0 & 0 & 1/8 & 0 & 1/8 & 1/8 & 0 & 3/8 & 0 \\ 1/8 & 1/8 & 1/8 & 1/8 & 0 & 1/8 & 1/8 & 1/8 & 1/8 & 0 & 0 \\ 0 & 1/8 & 1/8 & 0 & 1/8 & 0 & 0 & 1/8 & 1/8 & 3/8 & 0 \\ 0 & 0 & 0 & 1/8 & 1/8 & 0 & 0 & 1/8 & 0 & 5/8 & 0 \\ 0 & 0 & 0 & 1/8 & 1/8 & 1/8 & 1/8 & 0 & 1/8 & 3/8 & 0 \\ 0 & 0 & 0 & 0 & 0 & 0 & 0 & 0 & 0 & 0 & 1 \\ 0 & 0 & 0 & 0 & 0 & 0 & 0 & 0 & 0 & 1 & 0 \\ 0 & 0 & 0 & 0 & 0 & 0 & 0 & 0 & 0 & 0 & 1 \end{bmatrix}$$

The 9th row is the pollution source at (3,3). Upon reaching this grid point, the air is classified as polluted with probability 1. The 10th and 11th rows are the persistent states of clean and polluted air – that is, once a parcel of air is deemed clean (off the grid) or polluted (has come into contact with a pollution source), it remains clean or polluted. The 10th column is the probability the air parcel goes off the grid and is deemed clean. The initial vector of $< 0,0,0,0,1,0,0,0,0,0,0 >$ [to indicate the grid point (2,2)] is right-multiplied by this matrix many times until the sum of the 10th and 11th entries is one (the air has either left the grid or has gone through the pollution source). In this case, the probability that the air is polluted is 21%.

For a plot of the grid area used, the probabilities obtained using this method, and the site ultimately selected, see **Figure 2.5.**

We assume that the AMS 19 average PM2.5 concentration represents the ambient background PM2.5 concentration. Using this

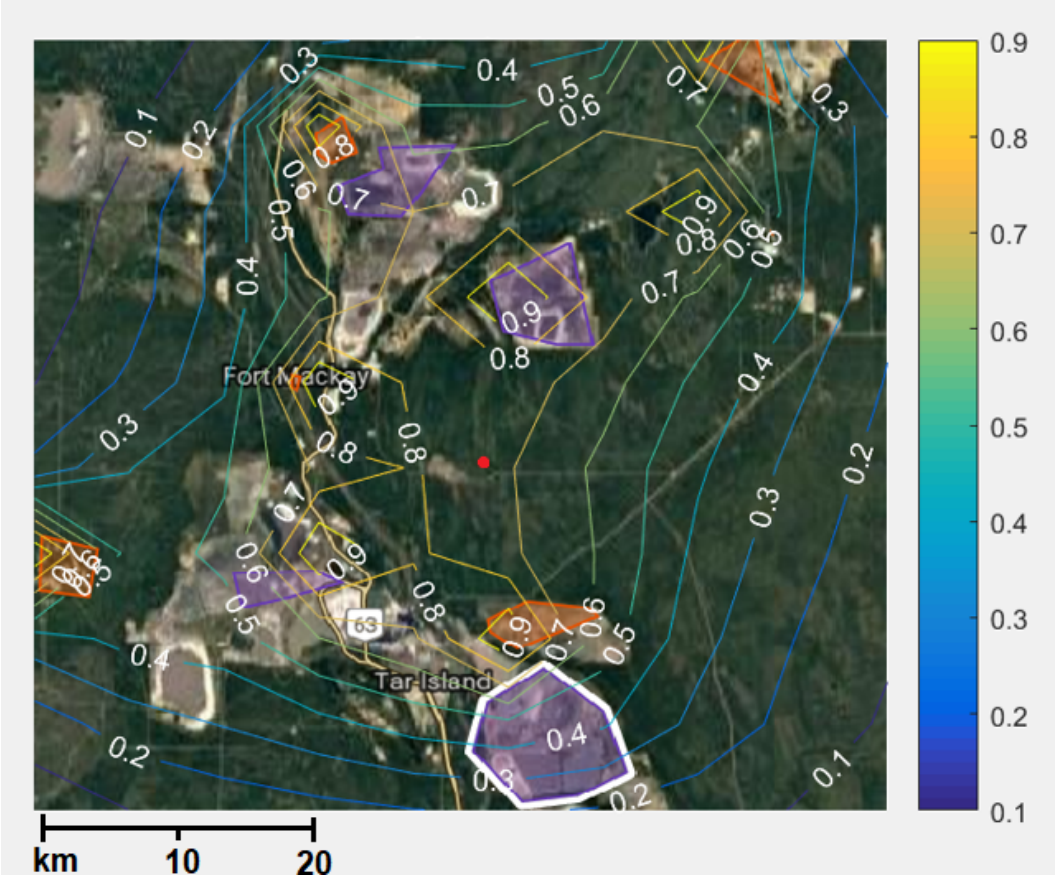

Figure 2.5: Probability of polluted air in the Oil Sands region according to the method described in **Section 2.2** (contours). Red dot is site selected.

value of 2.8 µg/m^3, we can calculate how much of the time this concentration was exceeded to see if the estimate was consistent with the predictions of the above method. According to data from the particle counter during the study period, 2.8 µg/m^3 of PM2.5 was at the 27^{th} percentile, consistent with the predicted percentage of 70% – 80% polluted air in **Figure 2.5** at the YAJP site.

2.3 Extended periods of clean/polluted air

Using the map of emission sources (Figure 2.3) and historical wind direction data, we can see how likely extended runs of good or poor air quality are. This is important because the intensive field campaign with air quality instruments would only last a limited amount of time. For example, we would like at least one pollution episode and at least one clean-air episode. But if there tend to be long runs of wind from a single direction, it is possible that we would not be able to sample a pollution episode or a clean-air episode.

Wind direction data can be gathered from a nearby site, JP104 operated by WBEA (WBEA). Those can be used to provide an estimate of how much time the site and its environs would spend in protracted periods of clean or polluted air.

Figure 2.6 shows time spent in runs of polluted air. There are several extremely protracted runs of potentially polluted air at JP104, up to 3,191 hours. But when we limit the periods considered to only summers, when the campaign would take place, we get **Figure 2.7**, which shows time spent in runs of polluted air during the summer (June through August). The maximum run of polluted air in the summer is only 28 hours, so it is unlikely that the site would encounter long runs of polluted air.

Figure 2.8 shows time spent in runs of clean air during the summer. The maximum run of clean air in the summer is short at 106 hours, yet there are still many runs of length > 20 hours such that it would be possible during the campaign to sample an

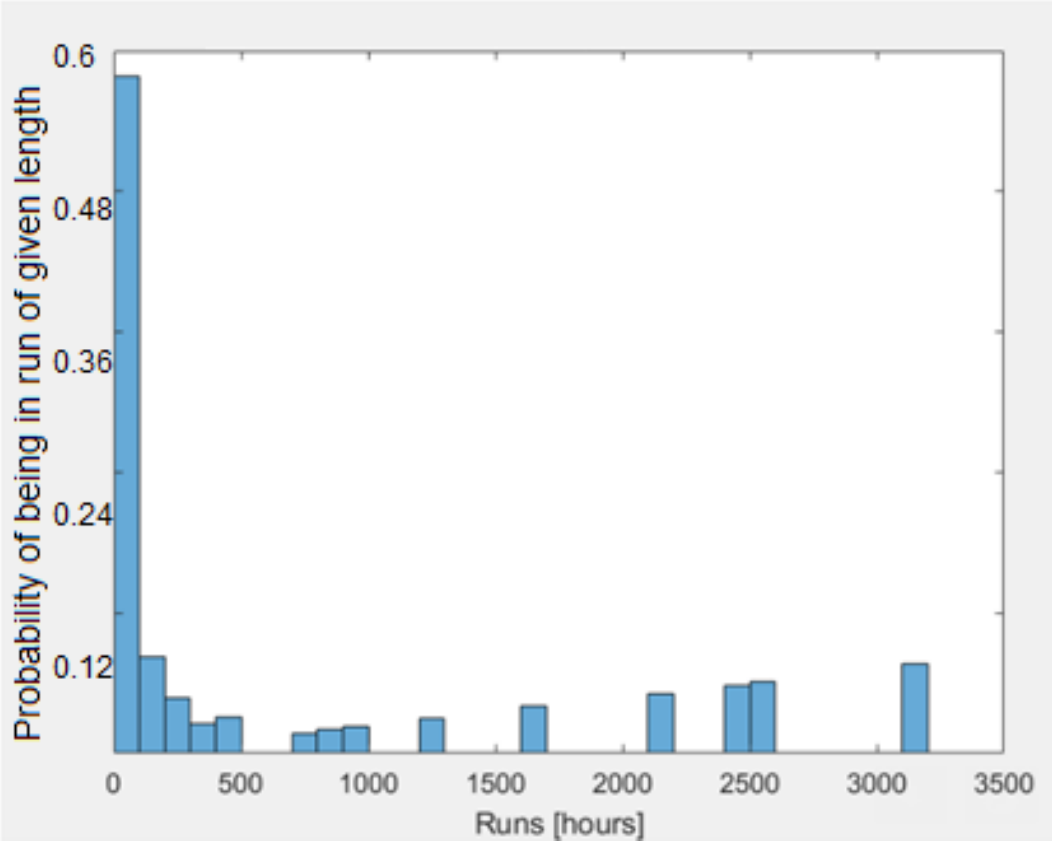

Figure 2.6: JP104 runs of polluted air. While most time is spent in runs of polluted air <100h, there is a significant risk of protracted runs of polluted air.

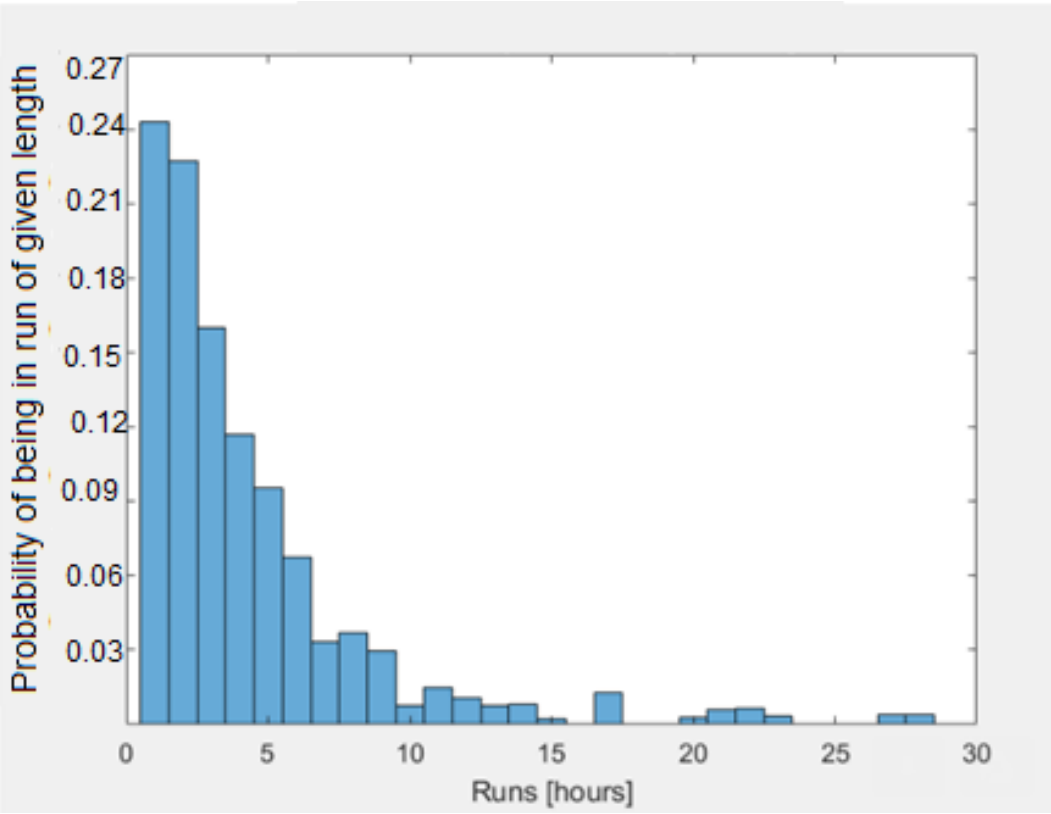

Figure 2.7: JP104 runs of polluted air, considering only June – August. Most runs of polluted wind angles are short in this season.

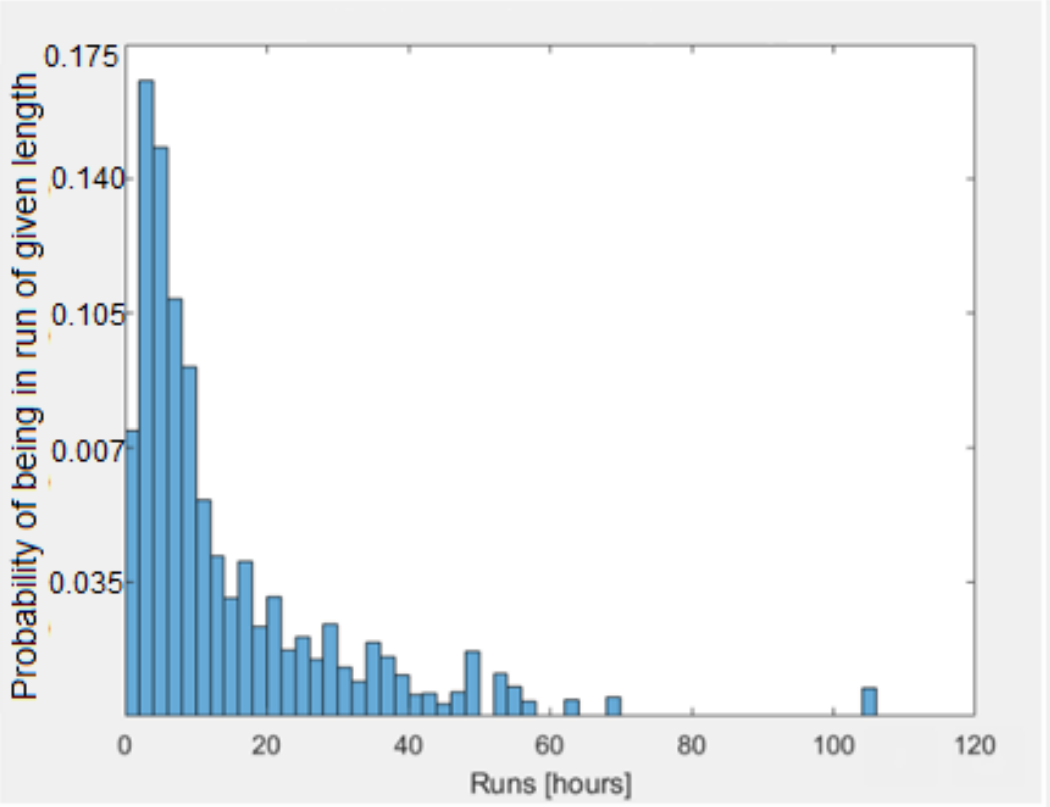

Figure 2.8: JP104 runs of clean air, considering only June – August.

aerosol growth event, which requires moderately long periods of clean air (Allan 2006).

2.4 Site description

Based on the analysis in **Section 2.3**, it was found that a location close to JP104 would be ideal for the YAJP experiment, because it has adequate fetch and high likelihood of sampling both clean and polluted air. Thus, it was decided to place the YAJP tower close to the JP104 tower. However, there is a road within 200 m of the JP104 tower. Therefore, we placed the YAJP tower in the northernmost clearing in the area we could access, 680 m north of the JP104 tower.

The tower was placed on July 18, 2018, in the Regional Municipality of Wood Buffalo. It is located at coordinates 57°7′ 21" N 111°25′ 35" W. The nearest hamlet is Fort Mackay, 16 km northwest, with a population of 742. An urban area, Ft. McMurray, lies 44 km south and has a population of 66,000. Although the area the tower is in is remote, there are many anthropogenic aerosol emission sources nearby from oil sands operations. These include Suncor to the south and north, and Syncrude to the east and southwest.

Pictured in **Figure 2.9** is the tower in its boreal forest surroundings. **Figure 2.1** shows surrounding emission sources. **Figure 2.10** illustrates the surrounding topography, which influences wind direction, as can be seen in **Figure 2.11**. Most winds follow the general axis of the valley, south-south-west and north-north-east.

The tower was situated in a small clearing in a forest. The closest paved road is the East Athabasca Highway, a private road with generally light traffic. The tower is 870 m northwest of that road. Access is through an unimproved road originally used for reflection seismology. The distance from the tower to this road is 26 m. The forest around the tower is pictured in **Figure 2.12**. A view of the crown around the tower is pictured in **Figure**

Figure 2.9: YAJP tower in its surroundings. Photo credit Melissa Dube of the WBEA.

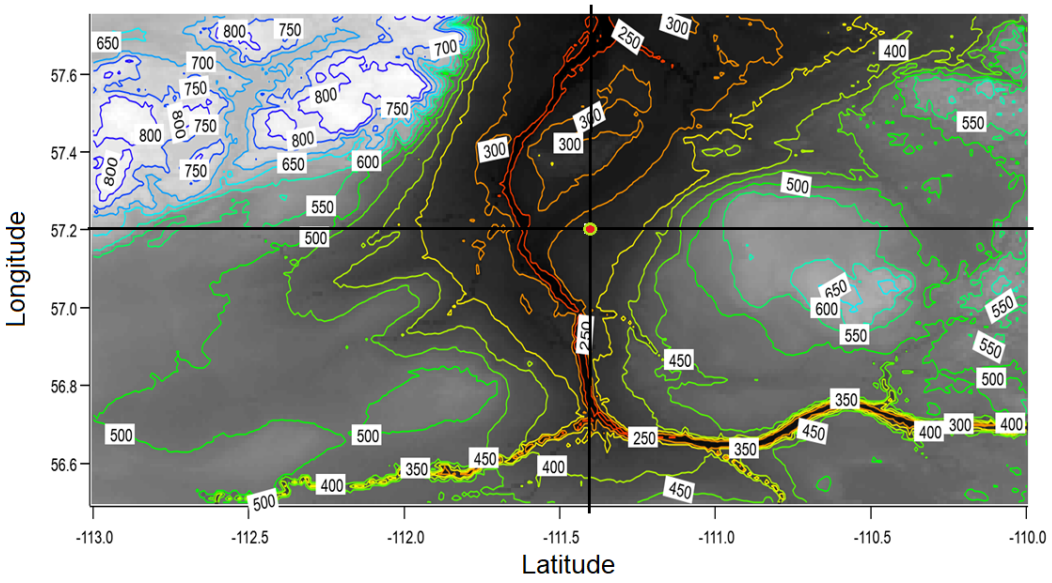

Figure 2.10: Map of topography of Oil Sands region. Elevation contours in [m]. Red dot indicates site selected.

2.13, showing the fairly sparse foliage even in the growing season. Based on the author's analysis using Wernert, ed. (1982) as a reference, the forest is a mature jack pine (Pinus banksiana) forest. The ground is covered in reindeer moss (Cladonia spp.). The undergrowth in the area is limited to some sparsely distributed blueberry bushes.

The forest's canopy height is 16 m tall. Although measurements of foliage density or leaf area index (LAI) were not made, a similar forest in proximity of the YAJP site had a measured LAI of approximately 2 (Gordon, 2013). The ground is sandy and well drained. Snow cover is present through the winter.

The YAJP site is powered by solar panels. It collects and remotely transmits data year-round, as power permits. Certain large instruments used in our project require more power than can be provided through solar panels. These instruments were deployed only during July 2017, when a generator was onsite to provide the power.

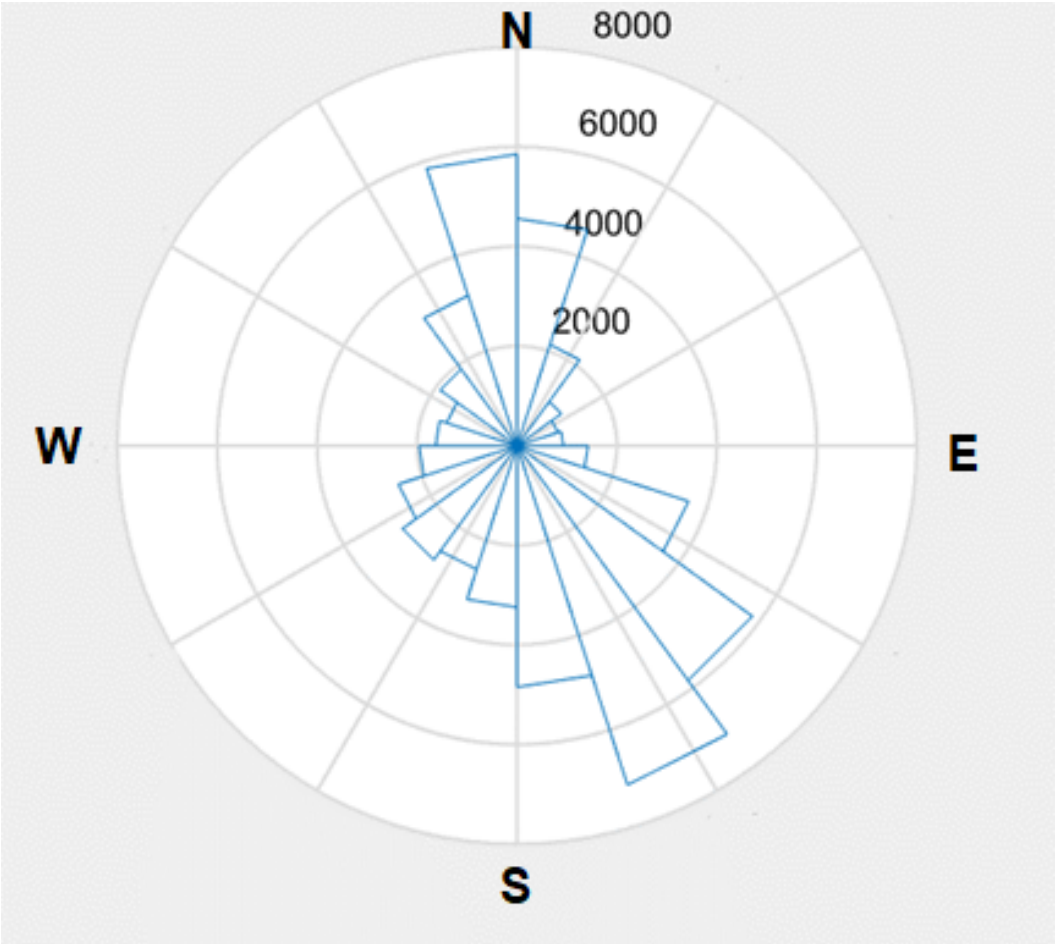

Figure 2.11: JP104 (WBEA) frequency by wind direction [h], at 29 m.

Figure 2.12: Trunk space and understory in the vicinity of the YAJP site. Photo taken July 2017.

2.5 Generator placement

Using data from the nearby JP104 tower maintained by the Wood Buffalo Environmental Association, we were able to determine the frequency distribution of wind direction. **Figure 2.11** shows that, at a tower close to YAJP site, winds were predicted to rarely come from the north-east. To minimise the amount of data rejected because of the generator, it was placed at a distance of 87 m from the tower, at an angle of 50 degrees.

Air quality data with wind direction from 40-60 degrees were rejected. This only occurred during 3 half-hour periods when the UHSAS was operational, out of 198 total periods.

2.6 Instruments

A list of instruments that were deployed is presented in **Table 1.** Their theories of operation and further details about their placement are presented in their respective sections. A schematic of instruments on the tower is given in **Figure 2.14.**

Figure 2.13: Forest crown in the vicinity of the YAJP tower. Photo taken July 2017.

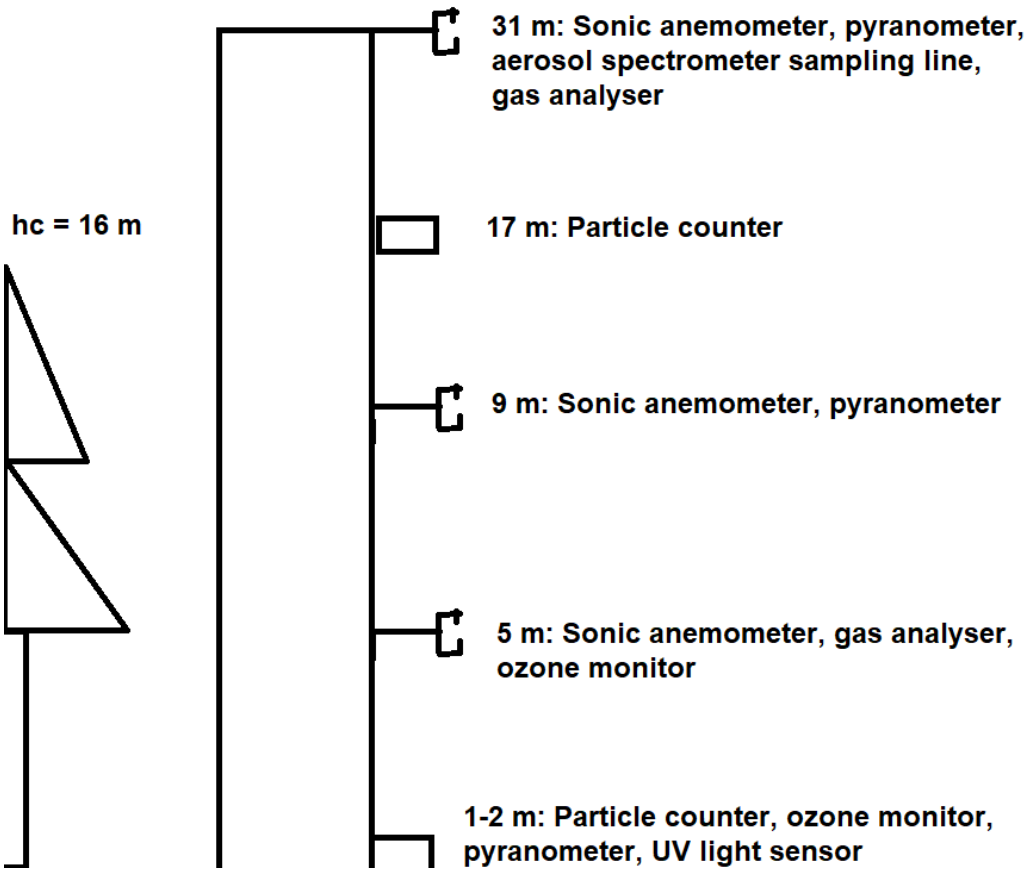

Figure 2.14: Schematic sketch of instrument placement on tower. Not to scale.

Table 1: Instrument placement summary. Intensive measurements are those that were only made during July 2017. Continuous measurements are those that continued through the winter.

Instrument	Sample Height [m]	Model & Remarks	Section	(C)ontinuous /(I)ntensive
Sonic anemometer	5.3	Type V, ATI	2.6.3	C
Sonic anemometer	9	Type Vx, ATI	2.6.3	C
Sonic anemometer	31.4	Type A, ATI	2.6.3	C
Aerosol spectrometer	31.4	UHSAS, DMT. Physical placement on ground	2.6.2	I
Light sensor	1.3	LI-190, Li-Cor	–	C
Light sensor	9	LI-190, Li-Cor	–	C
Light sensor	31.4	LI-190, Li-Cor	–	C
Pyranometer	31.4	Kipp-Zonen CNR4	–	C
UV sensor	1.5	Kipp-Zonen CUV5	–	C
Particle counter	1.85	DRX DustTrak	2.6.4	I
Particle counter	16.6	DRX DustTrak	2.6.4	I
Gas analyser	5.3	Li-Cor LI-7500A	2.6.1	C
Gas analyser	31.4	Li-Cor LI-7500RS	2.6.1	C
Ozone monitor	0.9	2B 205	–	I
Ozone monitor	5.6	2B 205	–	I
Ozone monitor	–	2B 205	–	I

2.6.1 CO_2/H_2O analyser

The CO_2/H_2O analyser measures attenuation of laser light along a path. The Li-Cor 7500 model emits laser light at two frequencies and senses how much they are attenuated with respect to a reference beam. The attenuation is related to the concentration of the gas in its path through a more general form of Beer's law whereby, instead of a linear response, a 5th order polynomial regression is used for CO_2, and a 3rd order polynomial is used for H_2O (LI-COR, Inc., 2016). Both these fits lack constant terms and are automatically corrected for cross-sensitivity effects, which is an imperfection in the sensor's frequency response (ibid).

The open-path model (LI-7500), with a path length of 12.5 cm, makes measurements without an enclosure and is suitable for the remote YAJP site as it needs little power. It uses 10 W during normal operation and 30 W at startup (LI-COR, Inc., 2016), as opposed to the closed-path model, which, in addition to the 40 W required for the instrument itself, needs an external pump.

We did not have access to a gas standard to calibrate the two instruments. However, they had recently been calibrated by the manufacturer, one 7 months and the other 12 months prior to the study. Also, the gas analysers were compared side-by-side in a laboratory environment, where they should yield similar gas concentration readings. However, we found that one gas analyser measured CO_2 and H_2O concentrations respectively 5% and 10% lower than the other. Therefore, for comparison purposes, we made a post-measurement scaling for both gas analysers, assuming that the value of gas concentrations is 2.5% and 5% higher than measured at the top of the tower, and similarly lower than measured at the bottom of the tower. This correction was necessary such that the two instruments would be consistent with each other.

Another correction was necessary for one of the gas analysers, due to the different densities of moist and dry air.

This correction is known as the Webb correction and is discussed in **Section 3.12.**

2.6.2 Aerosol spectrometer

The ultra-high sensitivity aerosol spectrometer (UHSAS) sizes particles between 55 nm and 1 µm with 1 µs temporal resolution. With this instrument, size-resolved particle fluxes can be investigated. It works by light scattering: particles that get into the path of the 1054 nm laser scatter the light onto two magnifiers (one for small particles and one for large ones) that then collect the light for measurement by photodiode. It can process up to 3,000 particles per second, with diameters between 55 nm and 1,000 nm (Droplet Measurement Technologies). However, Cai et al. (2008) have demonstrated that there is more than 50% loss for particles of size 55 – 60 nm, and an underestimation of the size of particles on the smaller end of its range.

Another artefact that may be present in this instrument's measurements is aerosol drying. Particles that are heated may shrink due to the loss of some of their water molecules to evaporation. The magnitude of this effect depends on the composition of the aerosols and the heat generated by the instrument. We did not have the tools to quantify this effect, but due to the power and size of the UHSAS, as well as the sun-heated line aerosols were drawn through, this effect could be large.

Due to the relatively large size of the UHSAS, it was mounted on the ground. It sampled through a 32 m long tube above the top of the canopy. This method will create some delay in the measurement with respect the sonic anemometer measurements. Also, particles tend to get spread-out as well as hit the walls of the tube. The time delay can be quantified with a cross-correlation calculation described in **Section 3.9**. The error introduced by diffusion within the tube and losses to the wall can be estimated as described in **Section 3.7**. With proper adjustments, it is still

possible to make accurate size-resolved flux measurements.

2.6.3 Sonic anemometer

The sonic anemometer is an instrument that can measure wind speed at high frequencies. It works by emitting acoustic waves from each of its three axes in one direction, then the other (ie. +x, −x, +y, −y, +z, −z). If there is a component of the wind that is parallel to the axis, it will take longer for the sound wave going in one direction to reach the other sensor than it will take the other. The velocity can be calculated with the following equation (Applied Technologies, Inc.):

$$V_l = \frac{d}{2}[\frac{1}{t_1} - \frac{1}{t_2}] \tag{1}$$

where V_l is the component of the wind along an axis, d is the path length, and t_1 and t_2 are the times it takes for the sound wave to reach the other end. The temperature can be calculated as follows:

$$T_v = \frac{c^2 M}{\gamma R} \tag{2}$$

where c is the speed of sound, M is the molar mass of the air, $\gamma = c_p/c_v$ is the ratio of the heat capacities of air, and R is the universal gas constant.

The anemometers used in this project are manufactured by Applied Technologies, Inc., models V, Vx, and A. They can sample at up to 200 Hz, but we chose to limit their rate to 20 Hz for easier processing, as higher frequencies offer little additional information. The three anemometers were mounted on the tower at heights within and above the canopy.

2.6.4 Particle counter

Two particle counters (model DustTrak DRX 8533 by TSI) were deployed. They work by measuring the scattering of a laser beam by particles, like the UHSAS, and measuring the amplitude of each

pulse to determine the size of the particle. The particle counters also measure mass concentration by taking the offset of the signal as representative of the density of the particle "cloud" that crosses the laser's optical path.

The particle counters have a detection limit of 1 $\mu g/m^3$ of particulate matter concentration. While they have a sampling frequency of 1 Hz in the lab, they are unable to sample so quickly in the field. This is because use of their auto-zero module, required in the field, limits their sample rate to once every two minutes.

One counter was mounted at the top of the canopy and one near the ground for gradient measurements of particulates. At a sampling frequency of once per 2 minutes, they are not fast enough for eddy covariance measurements, but they are still useful for monitoring particulate matter concentrations and deposition episodes.

The DustTrak was also compared against the UHSAS using paper-generated particles (that is, we ripped a piece of paper to simulate high particulate concentrations). The two instruments sampled beside each other for a period of 300 seconds. The coefficient of determination between these two instruments' time series was 0.54. Assuming an average particulate density of 1400 kg/m^3 (e.g. Rissler et al., 2014), the DustTrak overestimated particulate mass concentration by a factor of 3. This is consistent with Yun et al. (2015), who have found that a correction factor of 0.29 was required to bring the DustTrak in line with reference measurements.

The lower correlation between the DustTraks and the UHSAS is possibly in part due to the different ways the instruments measure particulate size and concentration. The DustTraks use a 655 nm laser and capture scattered light at 90 +/- 62°(Wang et al., 2009). They were calibrated using Arizona Road Dust. In contrast, the UHSAS uses a 1054 nm laser and captures scattered light at [33, 75.2] U [104.8, 147] degrees. It was calibrated

using National Institute of Standards and Technology standard spherical particles.

Differently-shaped particles scatter light at different angles which may be captured by one instrument but not the other (Sinclair and La Mer, 1949). A particle which scatters most of the light incident on it at a low angle may be detected as smaller than it really is by the UHSAS. Therefore, some discrepancy between the Dusttrak and the UHSAS can be expected.

Viana et al. (2015) and Rivas et al. (2017) have found that DustTrak data sometimes contain artefacts in the form of sudden, sustained jumps in particulate matter concentration until the following calibration. To counter this, the Dusttraks were calibrated through the use of an auto-zero module every 15 minutes, so that the jumps would not last longer than 15 minutes.

2.7 Instrument placement details

The tower was placed in a small clearing. The ozone sensor at a height of 0.9 m and the particle counter at a height of 1.85 m were placed 6 m west of the tower. Anemometers faced south. The paths of the H_2O/CO_2 analysers were 40 cm north and 10 cm above their respective anemometers. The bottom light sensor was placed on the support of the tower at a height of 1.5 m. It was placed slightly in the shade of a tree. The tower itself does not cast a shadow on the light sensors, because they are placed due south of the tower.

3 Theory

3.1 Flux calculations

Fluxes represent the transport of various quantities such as momentum, gases, and aerosols, per unit time per unit area. They are of the form $F = \overline{w'n'}$, where an overbar indicates a time mean, a prime sign indicates a fluctuation quantity, w represents the vertical wind, and n is the quantity of interest.

To calculate fluxes, we subtract out the mean quantities for each averaging period before multiplying the two quantities at each time and adding each point's contribution to the flux for the averaging period. Mean values are not turbulent effects that should be included in flux calculations (Wilczak, 2001).

3.2 Deposition and eddy covariance

To obtain flux values, this experiment uses the theory of eddy covariance. The derivation follows Gordon et al. (2011). It assumes a particulate matter concentration flux, but can be generalised to other quantities. We first start with the mass conservation equation:

$$\frac{\partial C}{\partial t} + \frac{\partial (u_i C)}{\partial x_i} + \frac{\partial (v_g C)}{\partial z} = D_M \frac{\partial^2 C}{\partial x_i^2} + S \tag{3}$$

where C is concentration, D_M is a Brownian diffusion coefficient, S is a source or sink term, v_g is the gravitational settling velocity, $i = 1, 2, 3$, and $z = x_3$. If we assume that particles are very small (v_g = 0) and that the concentration is horizontally homogeneous, then, taking the Reynold's average and integrating over z gives:

$$\int_0^{z_r} \frac{\partial \overline{C}}{\partial t} \mathrm{d}z + \overline{w'C'}(z_r) = \int_0^{z_r} \overline{S} \mathrm{d}z \tag{4}$$

where $\overline{w'C'}(z=0)$ is absorbed into the source/sink term. The second term is the diffusion flux. The third term is the source/sink. The first term, the storage flux term F_s, goes to zero if averaged over many diurnal cycles, assuming constant concentration with height. Then:

$$F_s = z_r \frac{C(t+\Delta t) - C(t)}{\Delta t} \tag{5}$$

In practice, we work with averages over short periods (the length of which will be determined in **Section 3.3**), and aggregate them together for a net flux. The flux $\overline{w'C'}$ is then equal to the sum of all sources and sinks below the measurement height, over a long period of time.

According to Foken (2008), this method has a 5-10% margin of error with proper correction, depending on how uniform the surroundings of the site are. The technique should not be used in areas of heterogeneous land surface, because if it is applied it will yield values for fluxes over multiple surface types.

3.3 Averaging period

The selection of an averaging period is of importance for the analysis that follows. It must be long enough to be statistically practical and include some lower frequencies, yet short enough to avoid longer-term diurnal effects. Wesley and Hicks (1977) suggest that for eddy covariance methods $z/(u \cdot T_a)$ should be greater than 10^{-3}, where z is the height, T_a is the averaging period, and u is the wind speed. Putting in the highest sustained value of u observed in the intensive field campaign period, 9 m/s, we get a maximum averaging period of 3,300 seconds, or just under an hour. Given that some effects of the diurnal cycle may be observed at an hour, and that it is customary to use a half an hour for an averaging period (eg. Burba, 2013), we will use that period for our analysis.

Some averaging periods are disrupted by power interruptions

and instrument issues. If a period consisted of less than 10 minutes of data, it was appended to the previous or the next period to avoid giving the short period undue weight in the analysis. If a period was longer, it was given its own point. There were 198 averaging periods during the intensive field campaign in 2017 when the anemometers were operational.

3.4 Rotation and planar fit

To account for the possibly imperfect mounting of the anemometers on the tower, an adjustment was made to the wind speed by "rotating" the anemometer measurements. This is done by assuming that the average vertical and zonal wind speed in each averaging period are zero (Wilczak et al., 2001). The horizontal rotation is made without loss of generalisation – we assume that we correctly measured the angle that the anemometers are facing, so the angle is simply indicative of the mean wind direction. However, by assuming that the vertical wind speed during each averaging period is zero, we are assuming that all vertical motions have a timescale of less than the averaging period.

In general, this is not true. Due to mesoscale dynamics or other local effects, sometimes there are different pitch angles for the anemometer for different time periods. If the anemometer is stationary, as in our case, then it should not have different values for the pitch angle over different averaging periods. The planar fit method attempts to correct this by assuming that the mean vertical wind speed is zero for the whole experimental period, but not necessarily for each time-averaging period of 30 minutes (Wilczak et al., 2001).

A planar fit is appropriate if the terrain we are sampling over is uniform in all directions around the site. **Figure 2.8** shows that the land use is fairly homogeneous in all directions. Since there seems to be little dependence of terrain on direction, the anemometers were rotated using the planar fit method.

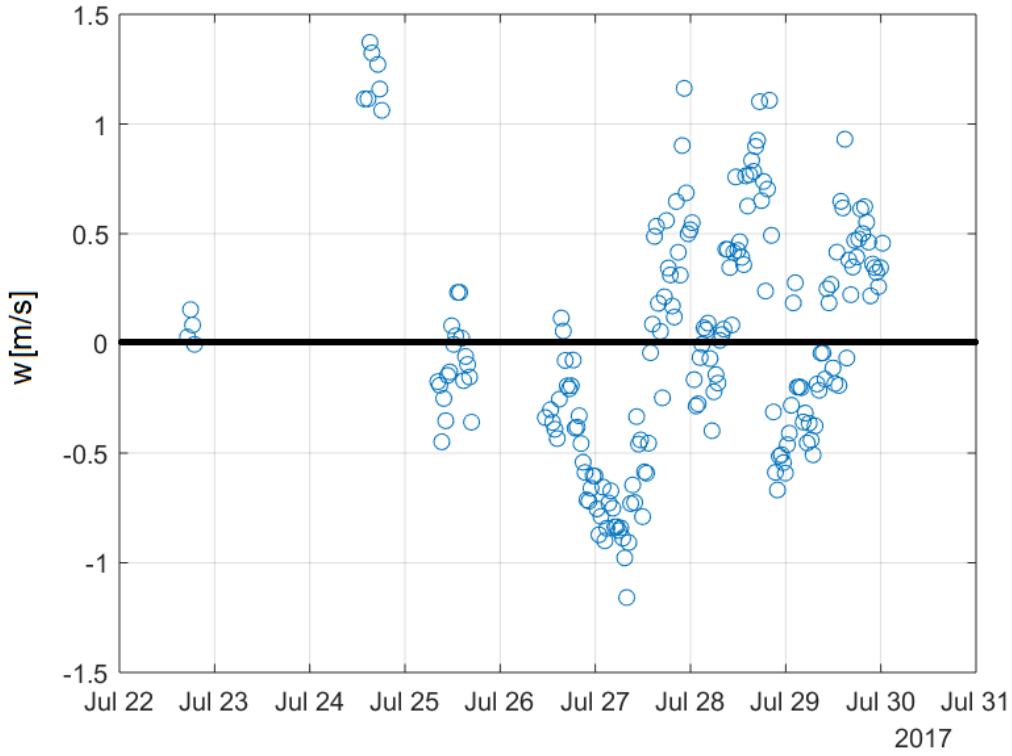

Figure 3.1: Mean vertical wind velocity for the 31 m anemometer. Most periods are within +/- 0.5 m/s.

Table 2: Anemometer pitch correction angles.

Level	Angle [Degrees]
5 m	−12.5
9 m	−13.3
31 m	−14.2

One issue with adopting a planar fit is that we must, in calculating fluxes, subtract out the mean vertical wind for each period. Mesoscale and synoptic vertical motions are not turbulent effects we wish to take into account when calculating eddy-covariance fluxes (Wilczak, 2001). **Figure 3.1** shows the mean vertical wind speed for each averaging period. While the mean vertical wind speed is usually small, there are periods where it exceeds 1 m/s, which could cause significant error in fluxes were it not subtracted out by counting mean motions as turbulent fluxes.

Table 2 lists the pitch angle correction for each anemometer. As expected, they are similar because they were mounted on the same tower, and they were levelled relative to the tower. These angles were larger in magnitude than expected. It is likely that the tower is not exactly vertical, being tilted to the south, or that the ground is sloped.

3.5 Despiking

Sharp spikes in data are usually artifacts, caused by electronic noise, processing errors, or phenomena such as rainfall. In analysing data, spikes should not be treated as true measurement data, because although the duration of the spikes may be short, their magnitude is often large and capable of distorting analysis.

For the gas analyser, spikes in the time series can be caused by rain and snow through the measurement path. This is caused by the hydrometeor being in the path during the reference measurement but not the attenuated measurement (Li-COR, Inc.,

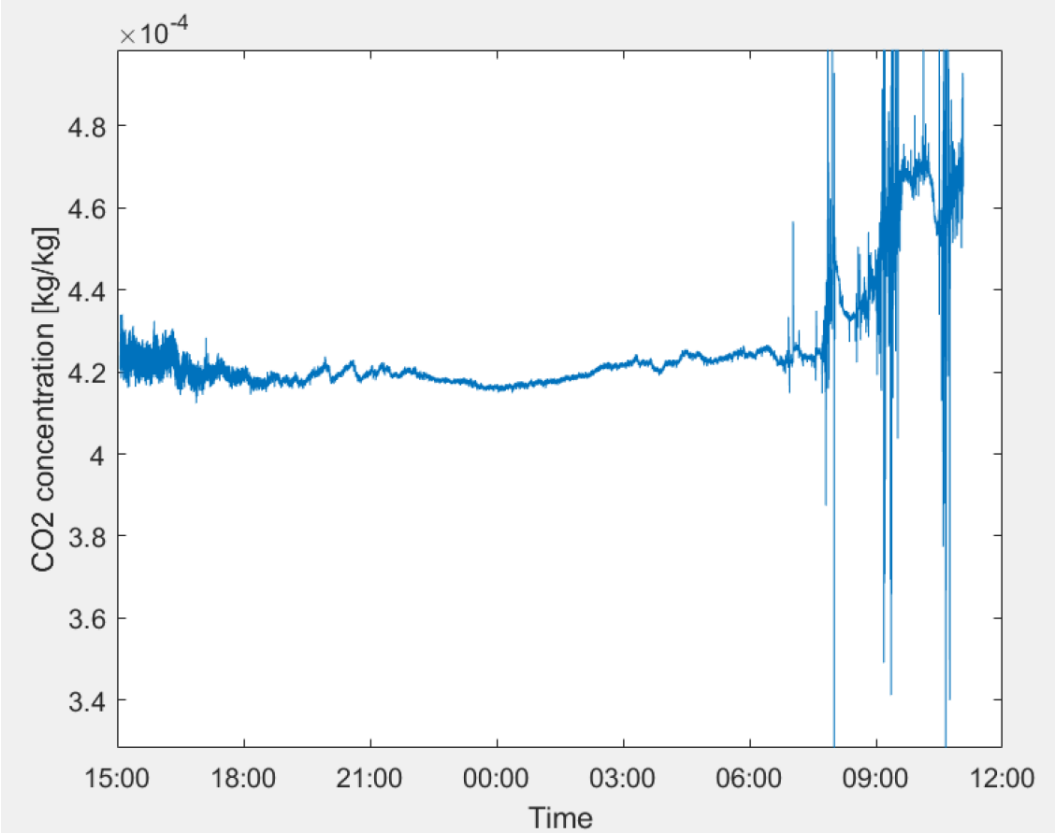

Figure 3.2: An example of raw data, with spikes. At approximately 8AM, it started raining, and it continued to rain through the end of the sampling period.

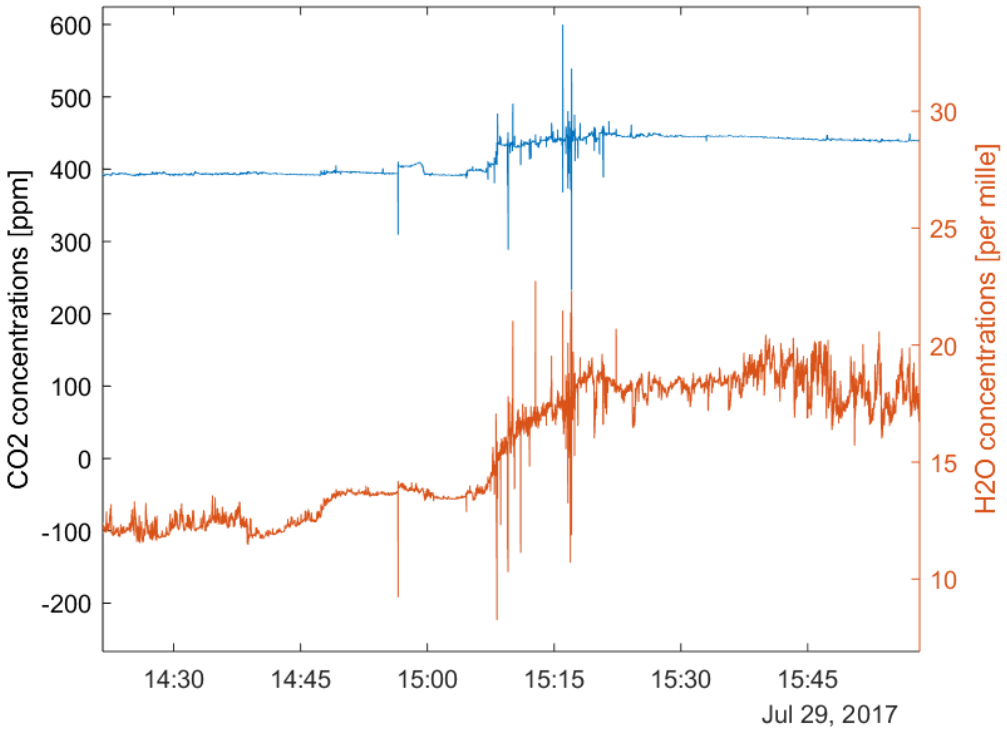

Figure 3.3: Raw data from the YAJP campaign. Some of the spikes were reflected in both channels, likely due to hydrometeors in the path.

2016), causing the ratio of the two to peak for one measurement. An example of data with spikes may be found in **Figure 3.2**. During this series, it started raining quite heavily, and the gas analyser was not able to accurately measure concentrations whenever a hydrometeor fell through its path. Another example, from the campaign, is in **Figure 3.3**, where there was significant rainfall.

For the sonic anemometers, spikes in the time series can be caused by objects (like hydrometeors) on the transducer or in its path. This is because these objects attenuate and scatter the acoustics in the path, affecting the transducer's ability to capture the correct signal (Applied Technologies, Inc). Also, during the intensive field campaign, there were occasional errors in processing anemometer data, yielding false values and spikes.

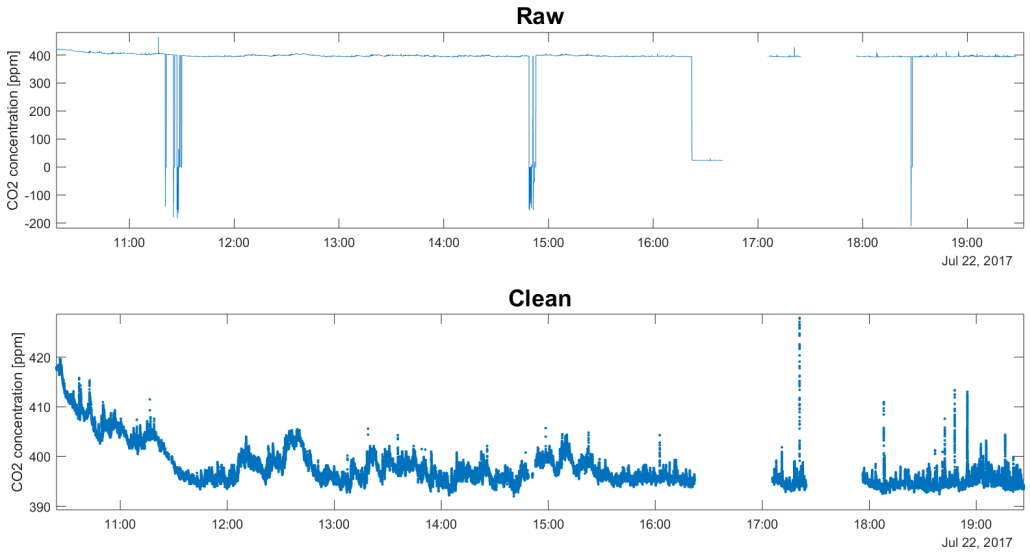

Figure 3.4: A comparison between clean data and raw data from the gas analyser (not on the same vertical scale). While the clean data also included some sudden peaks between 17:00 and 19:00, they were of low magnitude and were not rejected by the 5 standard deviation criterion used.

To despike the data, we process each 30-minute time period, rejecting for measurements that fall outside a certain number of

standard deviations of the mean and replacing them with a linear interpolation of the surrounding points (e.g. Foken, 2008). When spikes were one or a few points, they were replaced with a linear interpolation; when unrealistic values were sustained beyond 20 points, they were removed entirely. Analysis in this paper used a rejection criterion between 5 and 8 standard deviations depending on the time series. The procedure is repeated on the new series with a more stringent standard for what constitutes an outlier (that is, more standard deviations outside the mean are required to reject a point, as in e.g. Aubinet et al., 2012).

In **Figure 3.4** is a sample of clean data (spikes removed) and raw data (with spikes). In this manuscript, all analysis unless noted will have been done using clean data, and any remaining peaks that exhibit sharp increases could not be rejected.

3.6 Schotanus–Nieuwstadt–DeBruin correction

The Schotanus–Nieuwstadt–DeBruin (SND) correction, summarised in Schotanus et al. (1983), is necessary for temperatures measured with the sonic anemometer, because the temperature the sonic anemometer measures is not the true temperature, but closer to a density temperature. This is because the density of air (and therefore the speed of sound of air) is affected not only by its temperature, but also by its composition.

The correction is given by the following equation:

$$T = \frac{T_s}{1 + 0.32\frac{e}{P}} \tag{6}$$

where θ_s is the sonic potential temperature and e is the partial pressure of water vapour.

To obtain e, the partial pressure of water vapour, the output molar density of water vapour [mol/m^3] is converted to a pressure.

$$e(1 + 0.32\frac{e}{P}) = mT_sMR_w \tag{7}$$

where m is the observed water vapour mixing ratio, M is the molar mass of water, and R_w is the gas constant for water vapour. This is a quadratic equation for e which can be solved algebraically.

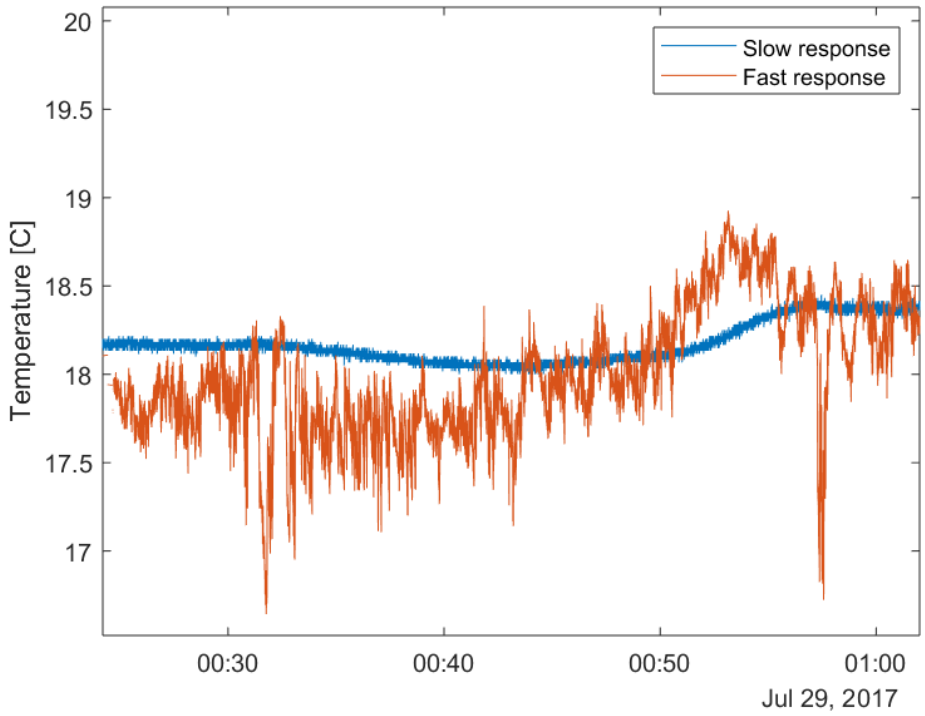

Figure 3.5: 31 m temperature as measured by a thermocouple vs sonic means (post-SND correction). Note the poor response of the thermocouple, its behaviour as a low pass filter, and its inability to capture eddies.

Although the site has separate temperature probes which do not need this correction, the temperature measurements of the sonic anemometers have a faster response time, because they are determined through sonic means, not thermocouples. For example, see **Figure 3.5** where the sonic anemometer was better able to capture high-wavenumber eddies and responded to a change in temperature more quickly. So in order to calculate heat flux at a high temporal resolution and accuracy, this correction will need

to be applied.

3.7 Line loss

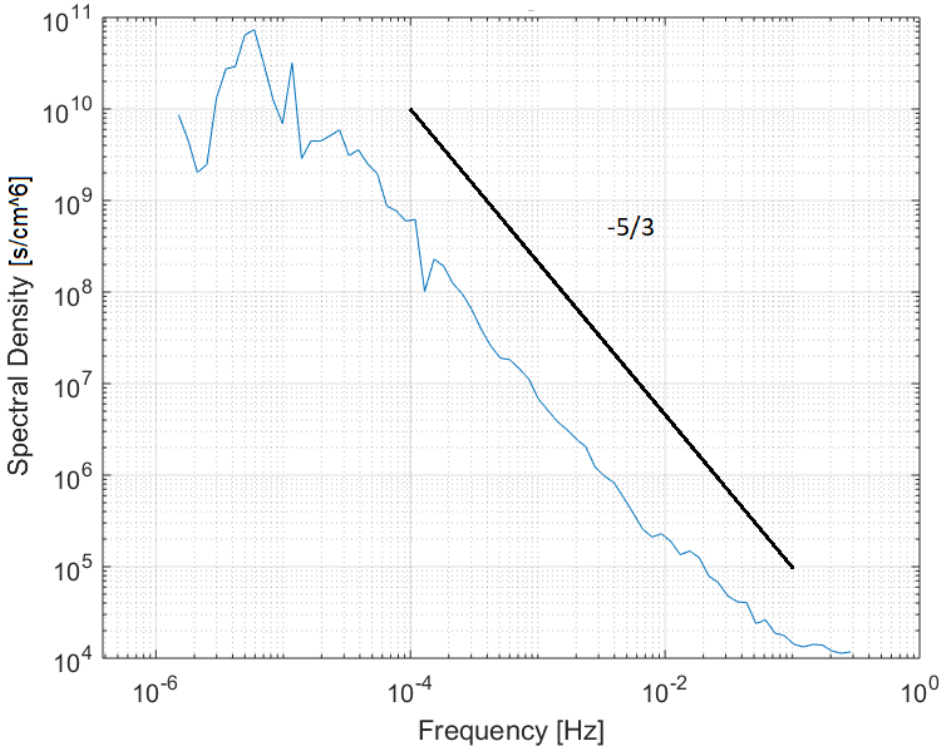

Figure 3.6: Spectrum of aerosol number density, not normalised.

Sampling for the UHSAS was made through a 31 m long line. A pump drew air through an opaque static-dissipative rubber tube from the top of the tower, and the UHSAS sub-sampled air from the bottom of this line at 50 mL/min. Because of the line length, there may be significant line loss of aerosols. Axial diffusion and bends may deposit aerosols onto the tube instead of into the instrument. To quantify this, we measured the particle number and mass concentration in an ambient environment with and without the line. The UHSAS sampled 96.5% of the mass without the line as with the line. Therefore, mass flux calculations were scaled by 1.036.

Table 3: Adjustments due to drawing down a 31-m line

Quantity	Scaling factor
Number density	1.036
Diam. at Peak Volume	0.970
Particle size distr. st. dev.	1.004

Besides line loss, Rosner and Tassopoulous (1991) show that changes in the peak size and distribution variance due to drawing air down a line could be calculated. **Table 3** presents values for the YAJP setup. The adjustment factors are close to unity and well within measurement error. The adjustment for the diameter at peak volume is less than the width of one size bin (about 28% of one bin), and the adjustment for the standard deviation of particle size distribution is less than 0.5% (or 3.6 % of one bin).

While air is travelling through the line, it forms a boundary layer within the line, with air near the surface of the line moving slower than the air in the middle (see Ch. 5.2 of Tennekes and Lumley, 1972). High-frequency aerosol signals may thus mix out into low-frequency signals, and the instrument may be sampling air that entered the line at different times.

In **Figure 3.6** is a spectrum for the aerosol number count density. Note that instead of the expected slope well past the Nyquist frequency, there is a flattening at high frequencies. This may be caused by mixing and "smoothing out" of high frequencies within the long line we sampled from. Therefore, due to this line effect, fluxes carried by high-frequency eddies may not have been captured .

Another possible contribution to the spectrum at high frequencies is aliasing, whereby energy at frequencies higher than the Nyquist frequency is folded back into resolvable frequencies. An instrument response issue is unlikely because the internal precision is 1 μs.

3.8 Generator angles

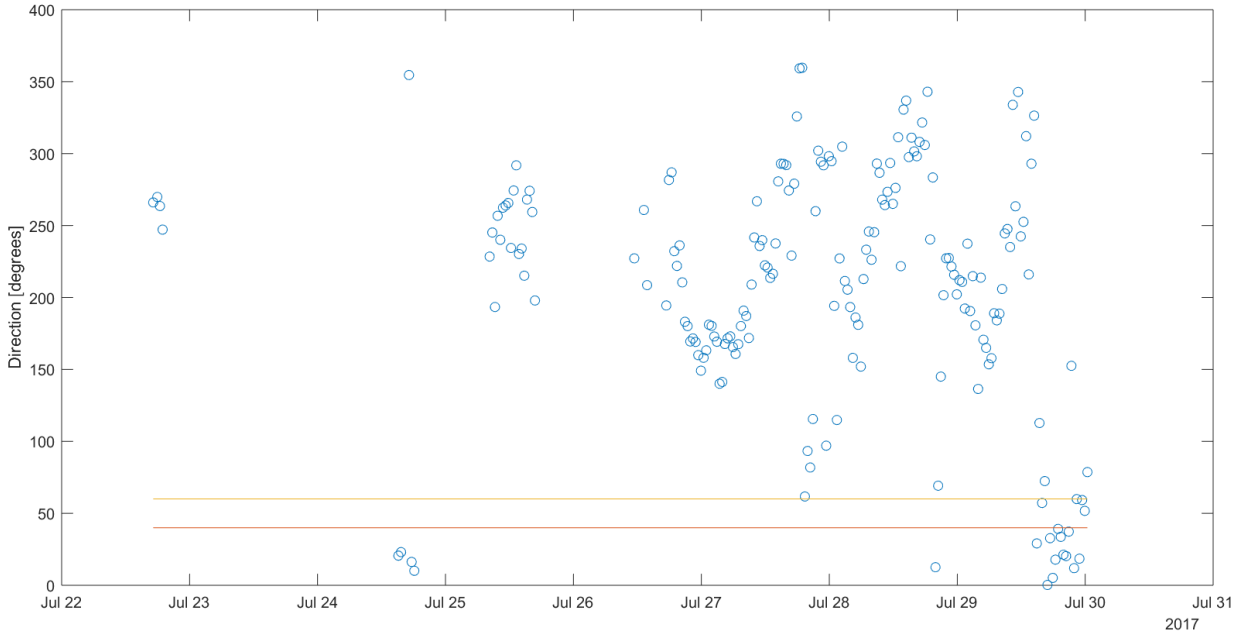

Figure 3.7: Wind angles from the lowest anemometer. 40 and 60 degrees marked with lines. Only 3 averaging periods fall within this range.

The generator consumed approximately 60 L of gasoline per day, or about 45 kg per day. Combined with about 4 kg of O_2 consumed per hour, the generator would emit about 6 kg/h of CO_2 and H_2O. At these quantities, even 87 m upstream, it could have a significant impact on CO_2, H_2O, and aerosol concentrations and fluxes.

For example, assuming a Gaussian plume in neutral stability conditions (Seinfeld and Pandis, 2006), a wind speed of 1 m/s, and no ground absorption, the increased CO_2 concentration due to the generator at the measurement location would be 560 ppm on average. The ambient CO_2 levels are approximately 400 ppm, so the generator would more than double the ambient CO_2 concentration.

We do not wish to include spurious measurements of trace gases and particulates in our results due to the generator. We noted any time the wind came from an angle of between 40 and 60

degrees. These are the angles corresponding to winds coming from the location of the generator. Wind angles outside this range would not cause more than 5% of the peak concentration of the plume to reach the sampling system, assuming a Gaussian plume under neutral conditions with a wind of 1 m/s (Seinfeld and Pandis, 2006).

Wind angles at a height of 5 m are shown in **Figure 3.7.** There were only 3 averaging periods out of 198 where the mean wind at a height of 5 m was coming from the generator.

3.9 Time-delay adjustments

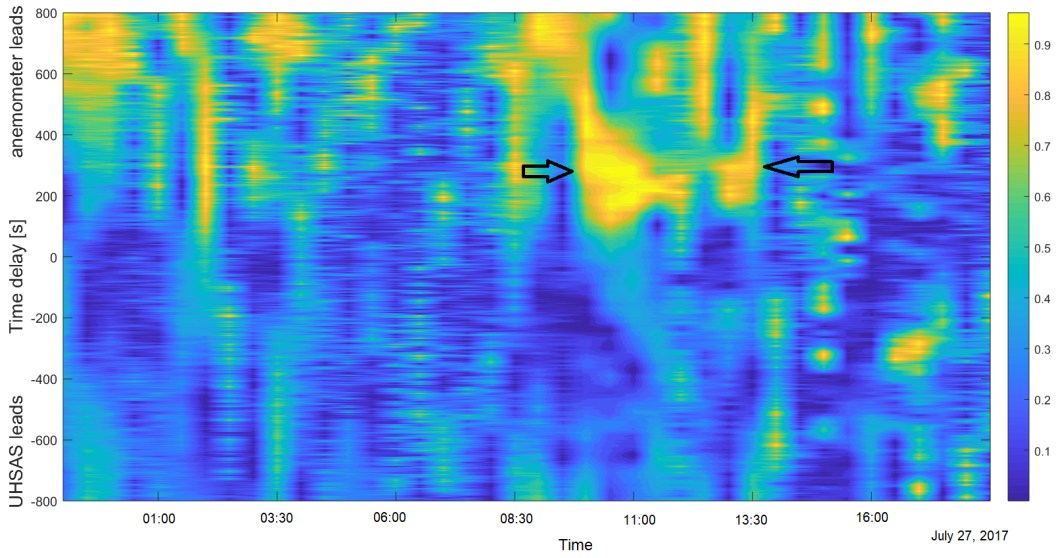

Figure 3.8: Cross correlation of aerosol flux, over many successive averaging periods. Colour indicates fraction of maximum flux observed in the averaging period. During times of significant flux episodes, indicated by the arrows, the time delay that maximised flux was 330 s (anemometer leads)

Various factors can result in an instrument being desynchronised with respect to other instruments by a constant amount of time. For example, the anemometers and the UHSAS were logged to different computers, with different timestamps.

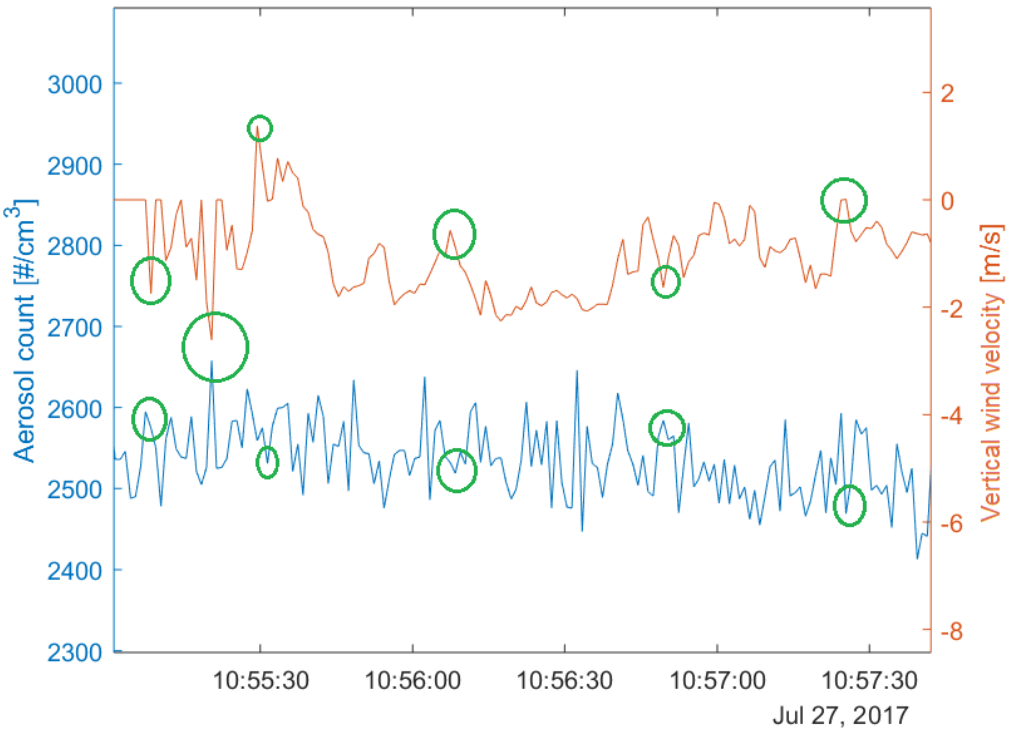

Figure 3.9: Selected peaks showing the negative correlation between the time series of aerosol number density (corrected for the time delay) and vertical wind velocity during a deposition episode.

Normally, these times would be synchronised, but in the study, we mistakenly did not do so. In other words, data from the UHSAS were had timestamps corresponding to one computer, while data from the anemometer had timestamps corresponding to another computer. These computers were not synchronised and could be different by a few minutes. An underestimation of fluxes would result if calculated with these mis-matched data.

This situation requires an analysis of the cross-correlation between the two time series; the time delay at which the cross-correlation is maximised is adopted as the true delay. This adjustment was performed in **Figure 3.8**. The delay between the instruments was established as 330 s, where the fluxes from the highest-flux periods were maximised. To confirm the adjustment, we can examine a short time-series of vertical wind speed and aerosol number concentration, noting that with the time-delay adjustment, the spikes anti-correlate, as in **Figure 3.9**.

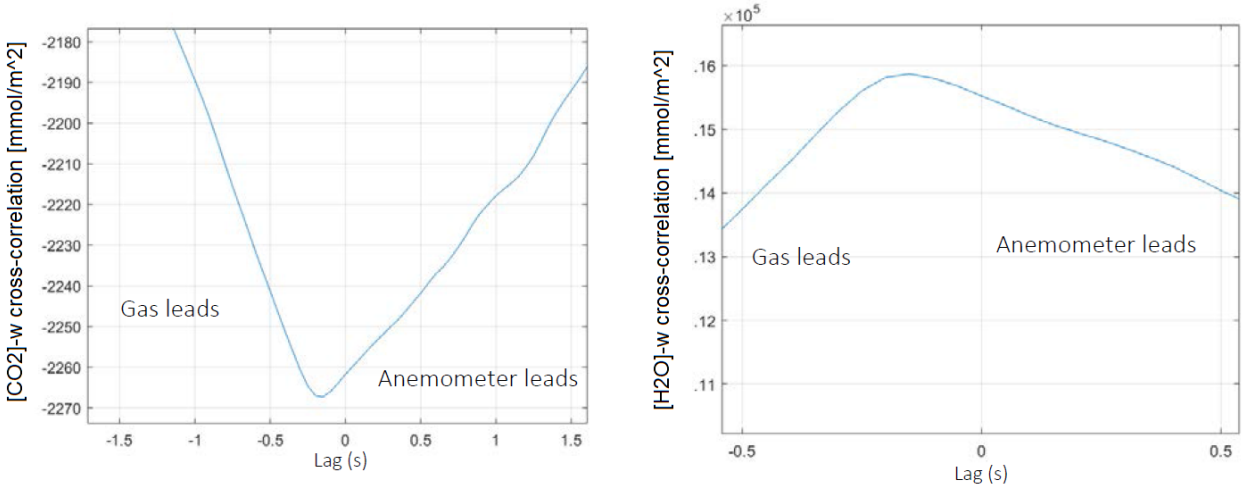

Figure 3.10: Cross correlation between the anemometer and CO_2 (left) and H_2O (right), during July 27, 12:30 PM to 1 PM, at 5 m. The cross-correlation of both gases have an extremum at 0.15 s (gases lead).

Likewise, in calculating CO_2 and H_2O fluxes, we also need to

make sure that there is no time delay between the gas analyser measuring these concentrations and the sonic anemometer. In this case, since both signals are being processed on the same micro-processor, we expect the time delay to be relatively small. In **Figure 3.10**, we see that the time-delay adjustment is close to zero. As a check, the time delay for H_2O should be identical to that for CO_2. Indeed, both are –150 ms (gas leads).

Since the adjustment would make only a small difference, 0.22% for CO_2 and 0.35% for H_2O, it was deemed unnecessary to make the shift for these instruments. The only time-delay adjustment made was for the aerosols, where the difference between the unadjusted and adjusted fluxes was often significant. For example, a significant deposition episode on July 27 was underestimated by 65% without the time-delay adjustment.

3.10 Spectral analysis

Spectral analysis can help in determining the length and time scales of mixing in the forest. Using the discrete Fourier transform (DFT), a time series can be decomposed into each frequency's contributions up to the Nyquist frequency, half the sampling rate.

The DFT only works on evenly spaced time series with no missing values. Stull (1988) notes that one cannot simply remove missing values from a time series and perform a DFT with the rest of the values, as such an operation would distort true time scales and introduce significant errors. Instead, we must replace these values with other data, either a Gaussian-distributed random number according to the data mean and variance or an interpolated value. However, too many such false values are liable to create misleading spectra when analysed with the DFT.

Alternative methods exist for spectral analysis of time series with many missing values. One can perform a least-squares fit of sine and cosine waves at each integer frequency such that the correlation coefficient at each frequency indicates the

contribution at that frequency. Such a technique is called periodographic analysis and is the preferred way to spectrally analyse time series with large and frequent gaps. For equally spaced time series, Stull (1988) shows that periodographs yield the same values as the normalised spectral intensity given by a DFT. The main disadvantage to this method is its computational inefficiency (ibid).

In this analysis, the DFT was used when no gaps of more than 20 consecutive points were in an averaging period. Any gaps present were filled with interpolated values. Anemometer readings often contained gaps larger than 20 points. In those cases, periodographic analysis was used.

3.11 Co-spectral analysis

The co-spectrum of the flux of n is given by

$$Co(w'n') = Re(\hat{w}) \cdot Re(\hat{n}) + Im(\hat{w}) \cdot Im(\hat{n}) \tag{8}$$

where · is a Schur product, a hat over a quantity indicates a DFT, Re(.) is the real part, and Im(.) is the imaginary part. Co-spectra represent flux density against wavenumber. We can use them to determine the size of eddies responsible for most of the fluxes.

Co-spectra are useful because they indicate which frequencies contribute the most flux over a period of interest (Stull, 1988). If, for example, the co-spectrum for aerosol number flux shows a peak followed by an inertial subrange, both at a frequency lower than 1 Hz, then we can be fairly confident we are not missing a large amount of flux if we perform flux calculations at 1 s resolution. However, if the spectrum shows the inertial subrange starting at frequencies greater than 1 Hz, we may be concerned that we are not capturing most of the fluxes if we calculate them at 1 s resolution (Wolf and Laka, 2007).

Because they depend on the phase of the spectrum and not

just the magnitude, co-spectra do not lend themselves to periodographic analysis, which would yield only the magnitude. Thus, only DFT methods can be used to perform co-spectral analysis.

3.12 Webb correction

In calculating gas fluxes, a correction is sometimes needed to account for the density fluctuations of air from water vapour and temperature. The density of water vapour being less than that of dry air, a water vapour flux of the same sign as the CO_2 flux leads to the overestimation of the magnitude gas fluxes as calculated by eddy covariance. Also, the density of warmer air being less than that of cooler air, a heat flux of the same sign as the CO_2 flux also leads to the overestimation of the magnitude of eddy covariance gas fluxes.

The Webb correction (Webb et al., 1980) is the name given to the adjustment to the raw flux based on air density variations correlated with gas gradients. It is given by the following equation:

$$F = F_r + \frac{\bar{C}H}{c_P\bar{T}}(1 + 1.61\frac{c_P\bar{T}}{L}(1 - 0.61\bar{q})Bo^{-1}) \quad (9)$$

where F_r is the uncorrected flux, C is the concentration of the gas whose flux is measured, H is the sensible heat flux, c_P is the heat capacity of air at constant pressure, L is the specific latent heat of vaporisation of water, q is the specific humidity, Bo is the Bowen ratio, and an overbar denotes a time mean over the averaging period.

The Webb correction is applicable to gas fluxes at the YAJP site at a height of 31 m. These fluxes were calculated from a gas concentration analyser which measures gas concentrations in mmol(gas)/m^3. Since the density of air is used when converting sensor output to a flux value, flux calculations should be adjusted as per the equation above. Because positive heat flux values and negative CO_2 flux values were observed during the day,

raw fluxes were likely underestimated.

The gas fluxes at a height of 5 m are not subject to the Webb correction. The gas concentrations measured by the instrument were in units of molar concentration (ppm for [CO_2] and parts per thousand for [H_2O]). The instrument has, at each measurement, already calculated the density of air and adjusted for it. Therefore, applying the Webb correction will not yield a more accurate flux result for the measurements made at a height of 5 m.

4 Results

4.1 General meteorological properties

Shown in **Figure 4.1a** is a plot of wind direction by frequency during the intensive field campaign at a height of 31 m. As expected from past meteorological data from nearby station JP104 (**Figure 2.10**), there are few northeast winds, but there were more south winds this year than previous years at JP104. Observations at YAJP site correspond well with JP104 data at a height of 29 m from the study period (**Figure 4.1b**).

Figure 4.1: Wind direction at a height of 31 m at YAJP site (left) [averaging periods], and wind direction at a height of 29 m at JP104 site (right) during IFC 2017 period [h].

YAJP measured wind speed distributions match less well with JP104 data at lower levels even during just the intensive field campaign, perhaps due to the influence of the canopy – JP104 is placed in a significantly larger clearing than our tower is. **Figure 4.2** compares the wind at a height of 16 m as measured at JP104 and the wind at a height of 9 m as measured at the YAJP site, and **Figure 4.3** compares the wind at a height of 2 m at JP104 with the wind at a height of 5 m at the YAJP site.

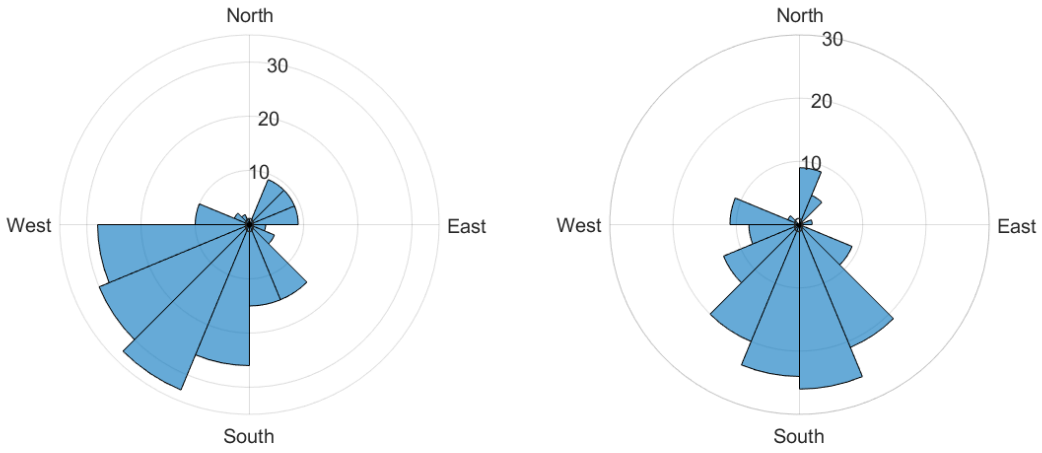

Figure 4.2: Wind direction at a height of 9 m at YAJP site (left) [averaging periods], and wind direction at a height of 16 m at JP104 site (right) during IFC 2017 period [h].

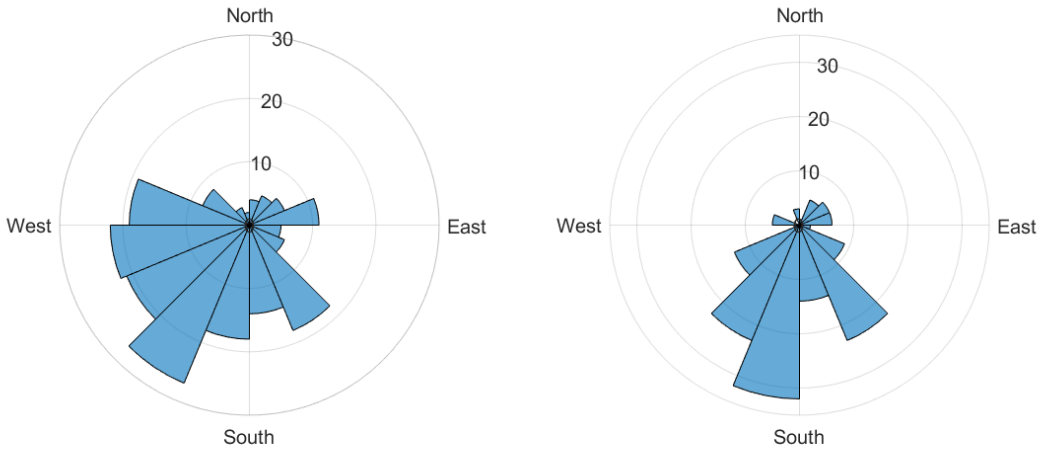

Figure 4.3: Wind direction at a height of 5 m at YAJP site (left) [averaging periods], and wind direction at a height of 2 m at JP104 site (right) during IFC 2017 period [h].

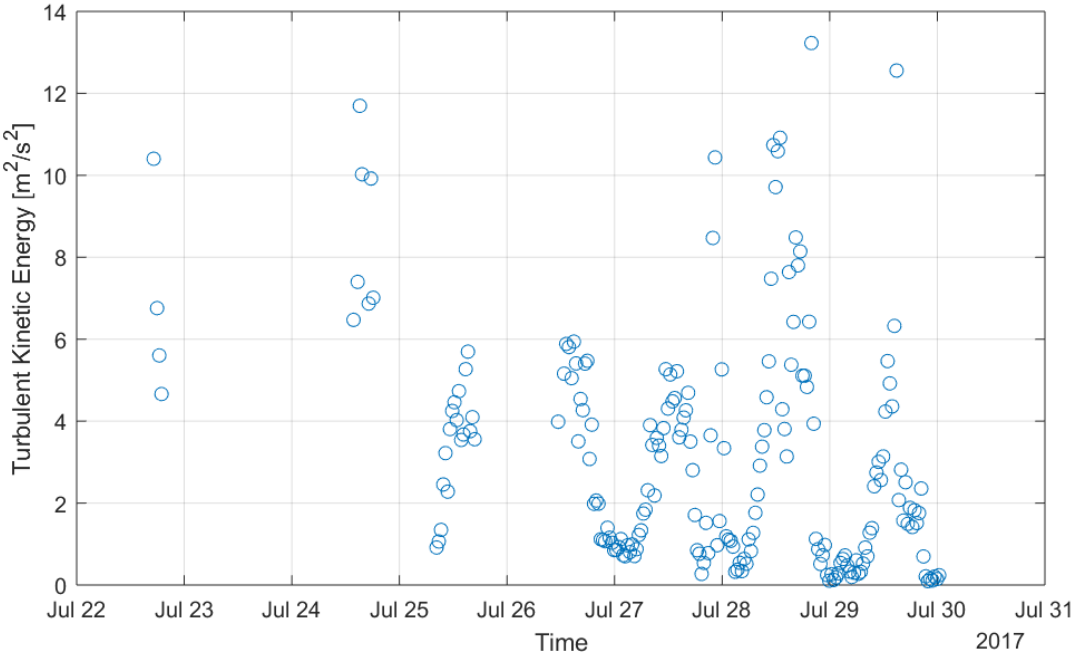

Figure 4.4: Turbulent kinetic energy at a height of 31 m.

The turbulent kinetic energy (TKE) is the variance of wind speed. It is a measure of the intensity of turbulence in the air. It is plotted in **Figure 4.4**. Since the thermal generation of turbulence is greatest during the day, the TKE follows a diurnal cycle. Generally, with greater turbulence, there is greater mixing and flux, so periods with larger values of TKE exhibit larger fluxes and greater mixing.

Forests modify the meteorology within the canopy sub-layer, which extends to about twice the canopy height h_c = 16 m (Foken, 2008). Canopies decrease the wind speed in this area. The leaves, crown, and trunk of the trees create drag on the flow. The two lower anemometers, in and below the crown, are subject to these effects. **Figure 4.1a** shows a wind rose for the intensive field campaign period for the upper anemometer, just outside of the canopy sub-layer, compared with a wind rose in the canopy in **Figure 4.3a**. Besides the slight rotation attributable to the

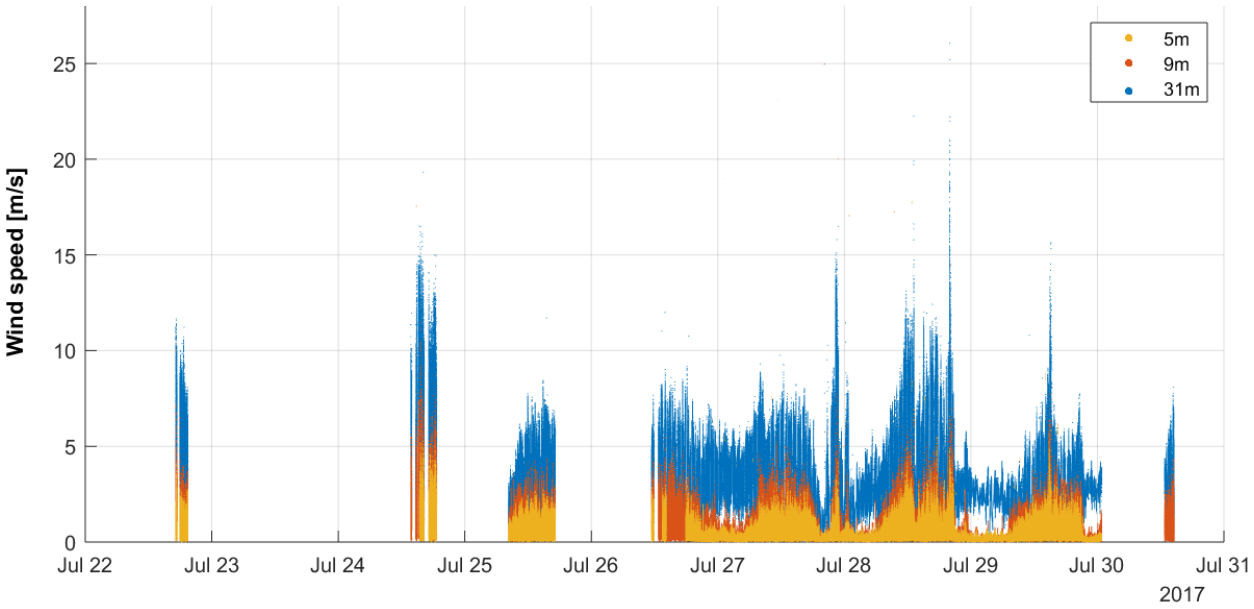

Figure 4.5: Wind speed as measured by sonic anemometers.

surface roughness (see §3.1.2 in Garratt, 1992 for a discussion), the wind directions in the canopy are more evenly distributed and are less regular in distribution compared to those above the canopy.

In addition, **Figures 4.5 and 4.6** show that the wind speed outside the canopy is greater than the wind speed inside the canopy. Over an open surface, we expect an increase in wind speed with height as well. However, extrapolating from a log wind profile, the observed increase in wind speed at the YAJP site is much greater than the 1.8-fold increase expected over the same heights from a log wind profile over a flat, open surface (e.g. Garratt, 1992). If we instead extrapolate downward from the two upper measurements, we get an unphysical negative mean wind speed. Instead, in a canopy, an exponential wind profile is expected (Oke et al., 2017).

Canopies also affect the vertical profile of temperature. The temperatures inside and outside the canopy can be contrasted

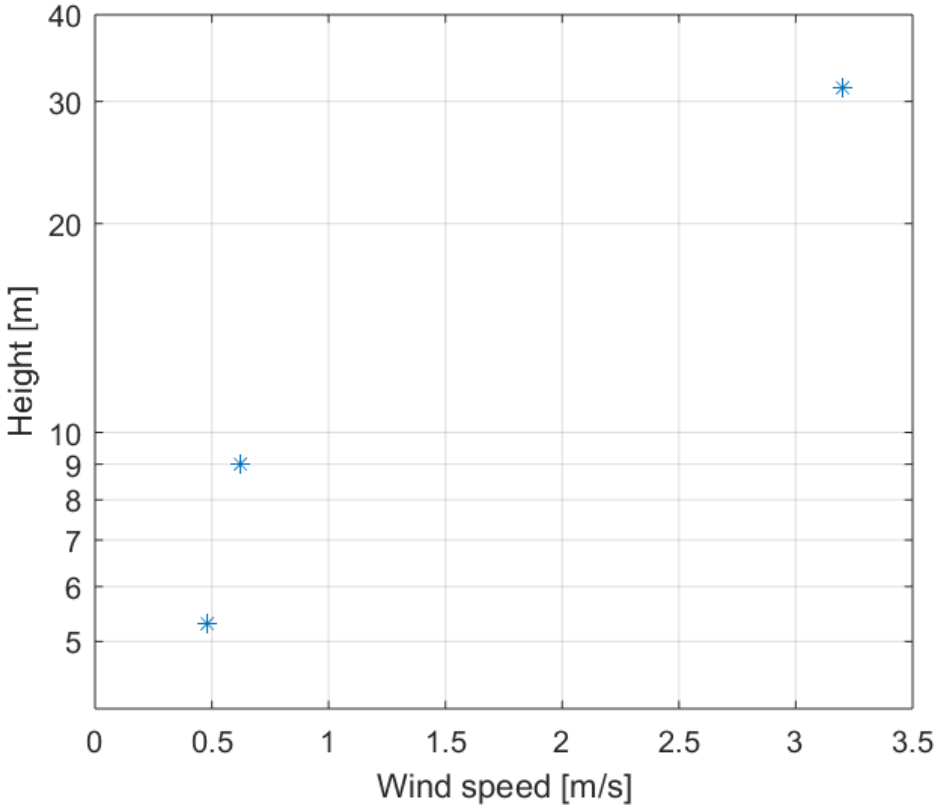

Figure 4.6: Mean wind speed during the 2017 field campaign. Error bars show ± 1 standard deviation.

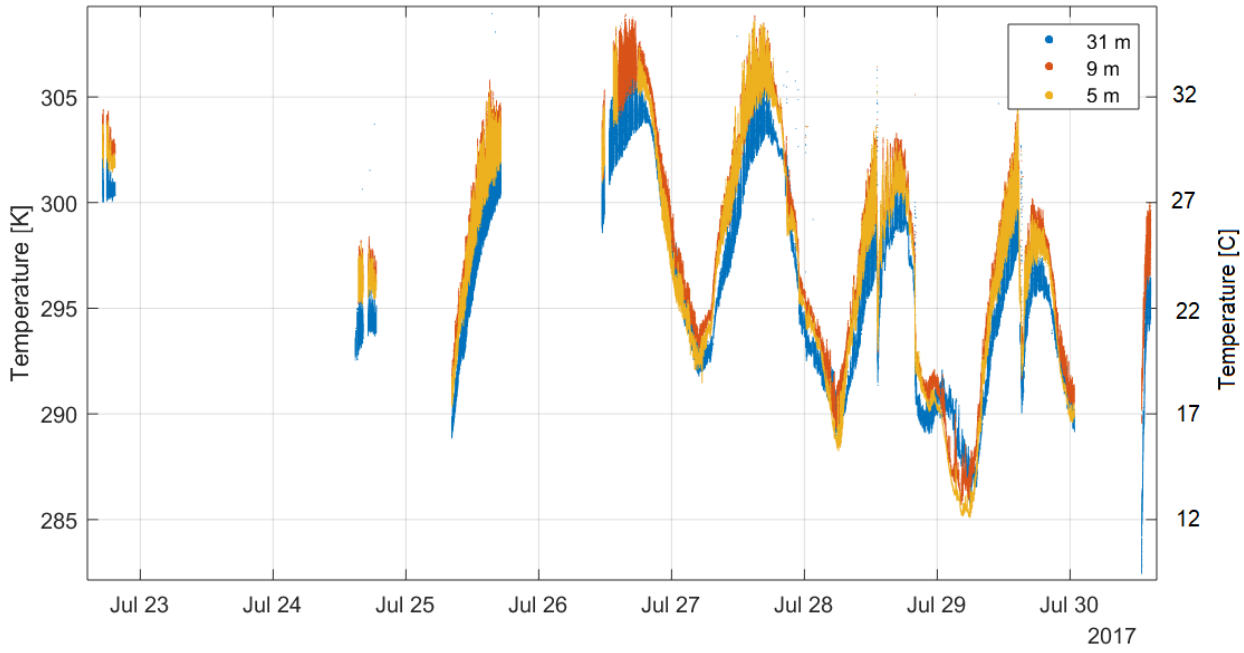

Figure 4.7: Temperature as measured by sonic anemometers and corrected with the SND correction (**Section 3.6**)

in **Figure 4.7**. During the day, the temperature inside the canopy was higher than the temperature outside the canopy. At night, the temperature inside the canopy was sometimes higher and sometimes lower than the temperature above the canopy.

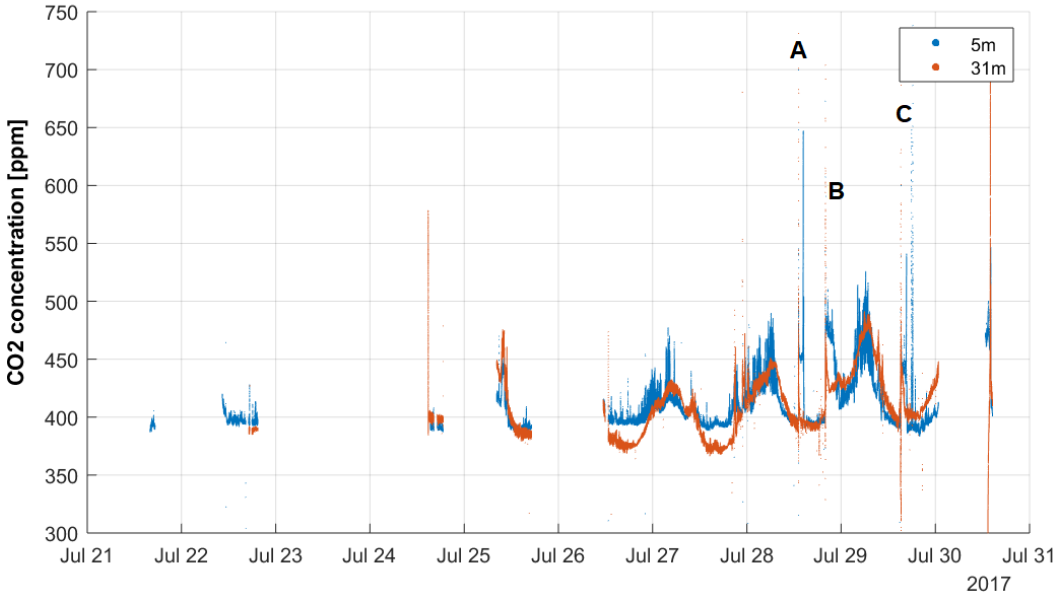

Figure 4.8: CO_2 concentration. A, B, and C refer to episodes discussed in **Section 5.1**.

Forest canopies can also affect the concentration of different gases. For example, see **Figures 4.8 and 4.9**, where the concentrations of CO_2 and H_2O are shown. Besides the diurnal cycle evident in these measurements, peaks and subsequent plateaux are labelled in the [CO_2] series. As will be discussed in **Section 5.1**, the difference between the concentration of these gases at 31 m and 5 m during these events is likely due to the canopy inhibiting exchange.

4.2 Aerosols and aerosol flux

Data from the UHSAS were used to determine aerosol number concentration. **Figure 4.10** is a time series of size-resolved

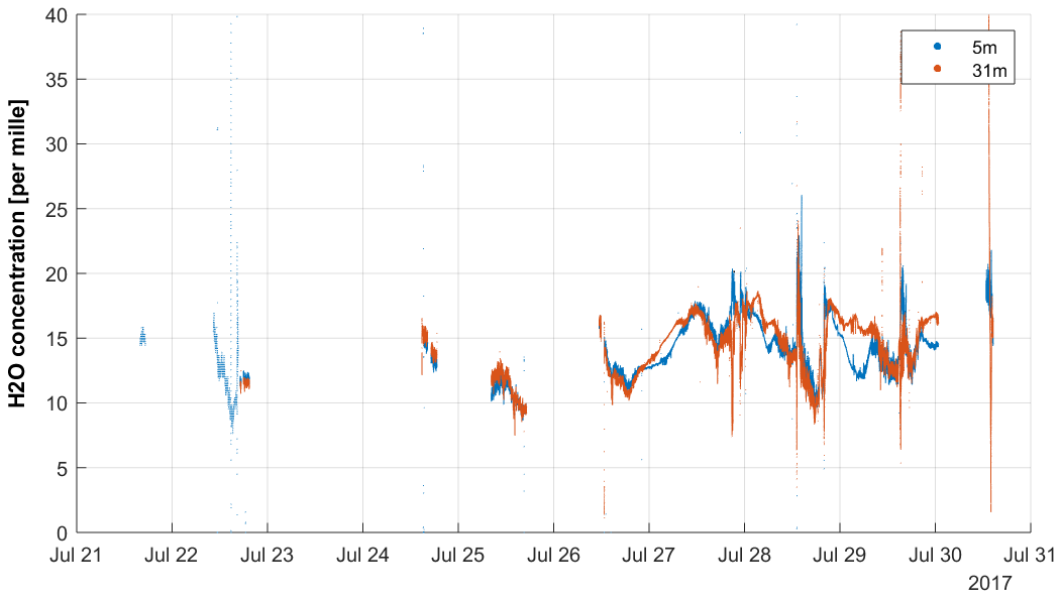

Figure 4.9: Water vapour concentration.

aerosol number concentration. The majority of the time, most particles are below 100 nm in diameter. However, the median particle size was sometimes larger, for example during the afternoon of July 27.

Masses derived from the particle diameters optically measured, assuming a mass density of 1,400 kg/m^3 (Rissler et al. 2014), are shown in **Figures 4.11 and 4.12. Figure 4.11** shows that most aerosol mass is contained in particles of diameter around 300 nm. Contrast with **Figure 4.10**, where it is shown that most particles are below 100 nm in diameter.

Figures 4.13 and 4.14 show the size-resolved and total particle flux, respectively. An upward flux was observed during 82 averaging periods, or about 45% of valid averaging periods. This is less than what was observed in Gordon et al. (2011), where upward fluxes were observed 60% of the time in a rural mixed forest. However, there were more upward fluxes than were reported in Pryor et al. (2013), in a pine forest in Colorado, where over one third of fluxes were reported to be upward.

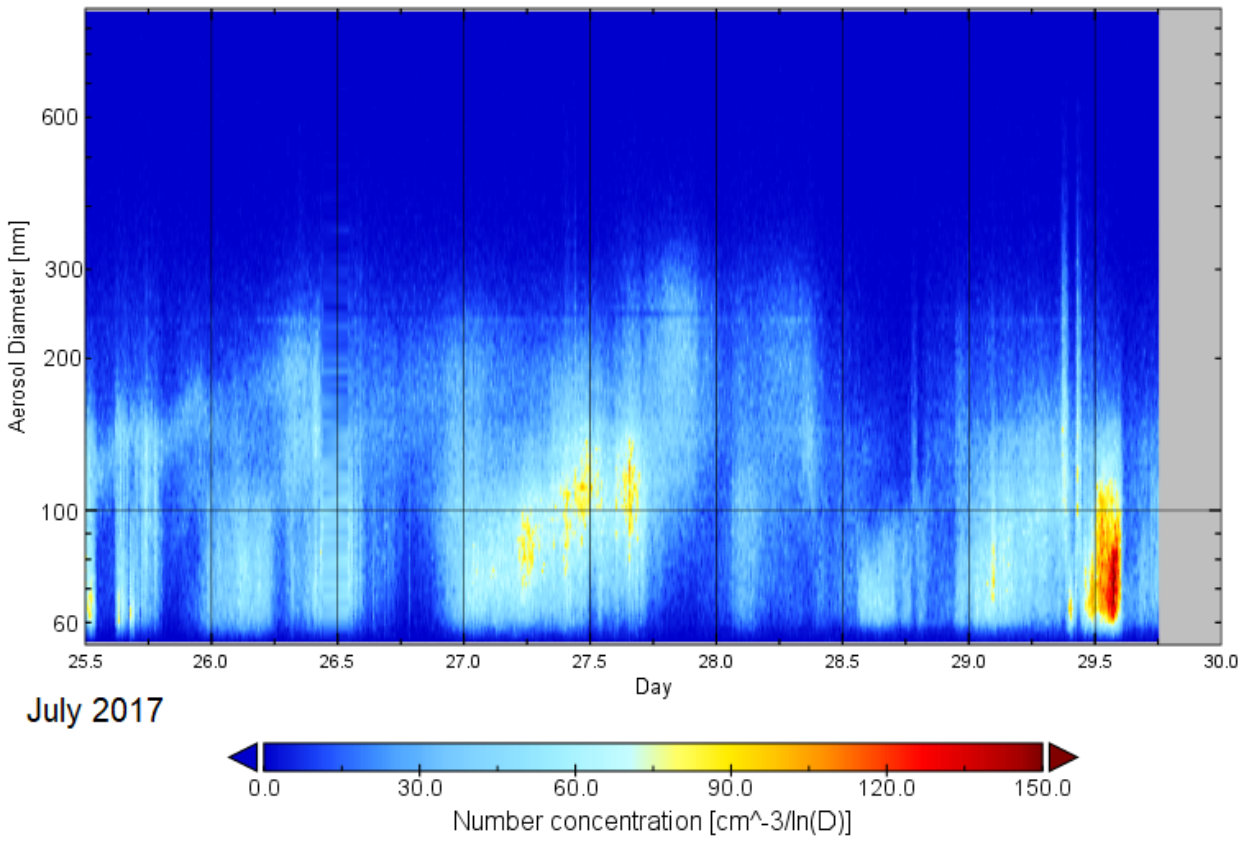

Figure 4.10: Aerosol number concentration (55–1000 nm) as measured by the UHSAS.

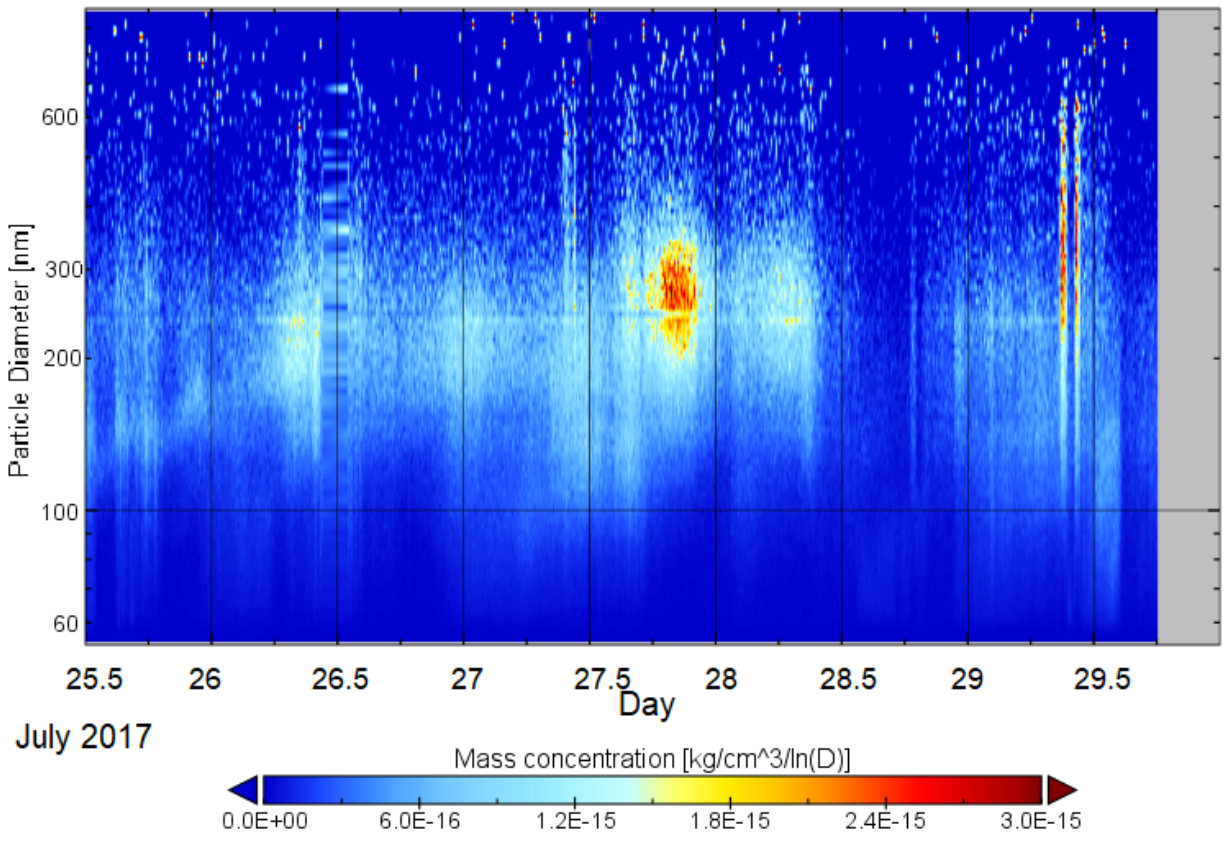

Figure 4.11: Particle mass concentration (55–1000 nm) as measured by the UHSAS.

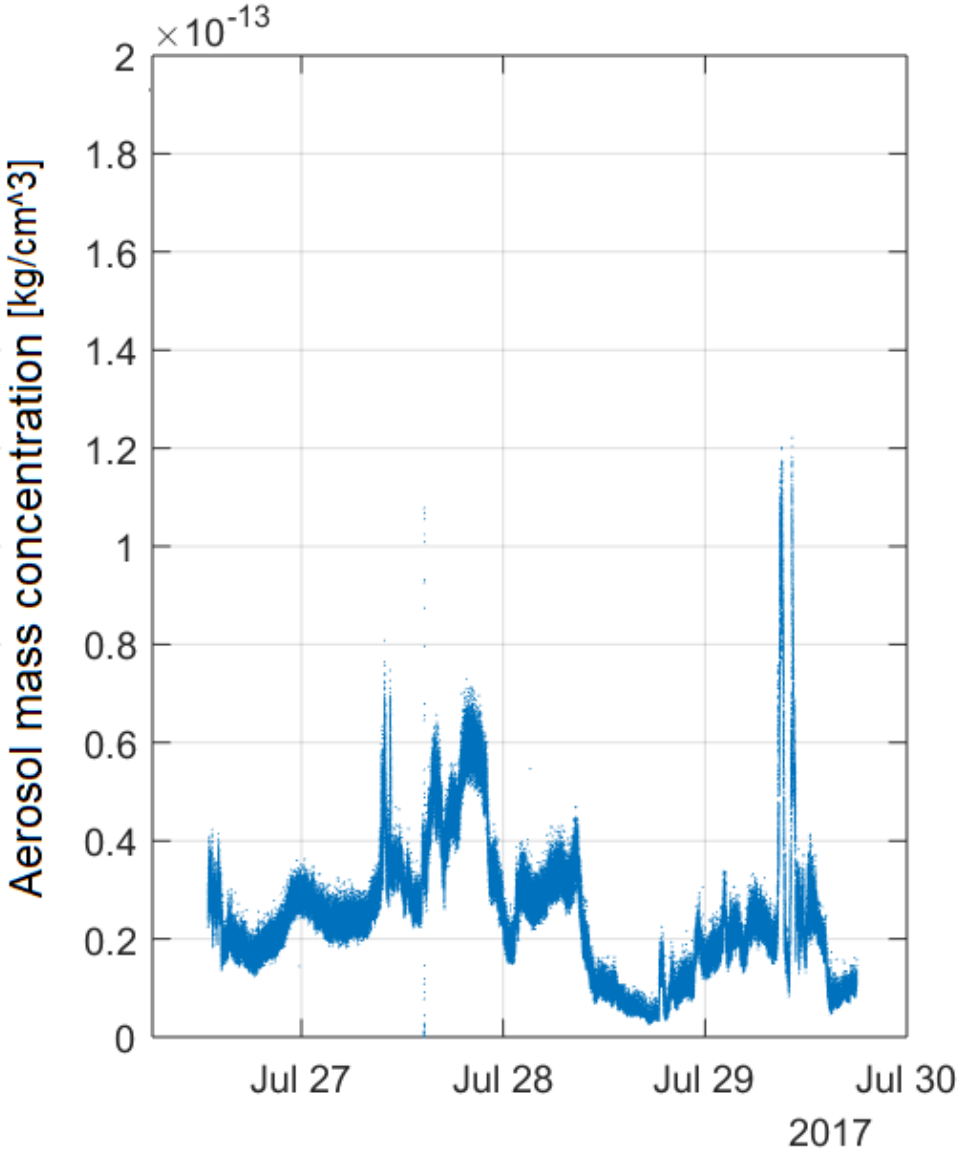

Figure 4.12: Total particle mass concentration (55–1000 nm) as measured by the UHSAS.

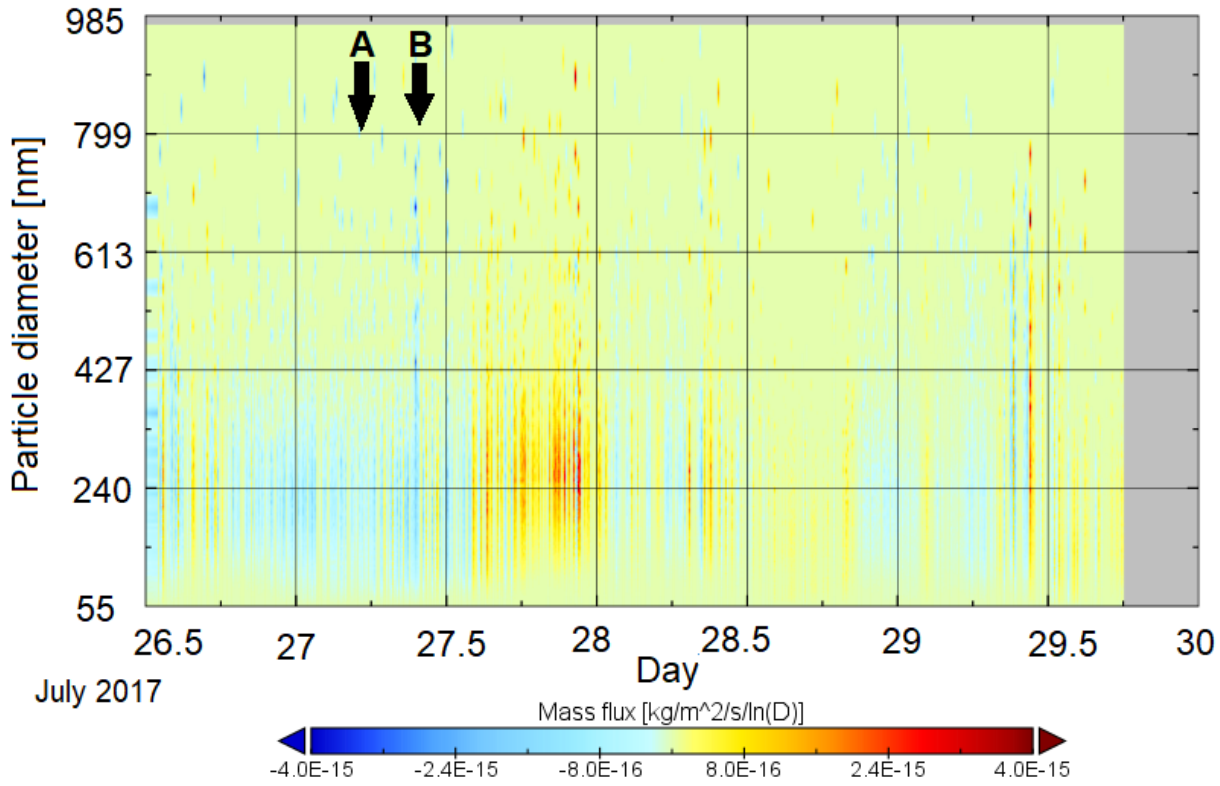

Figure 4.13: Size-resolved particle mass flux at 31m, as determined by the UHSAS, and assuming a density of 1400 kg/m^3. Particle size distribution at points A and B in the figure are compared in **Section 5.3.**

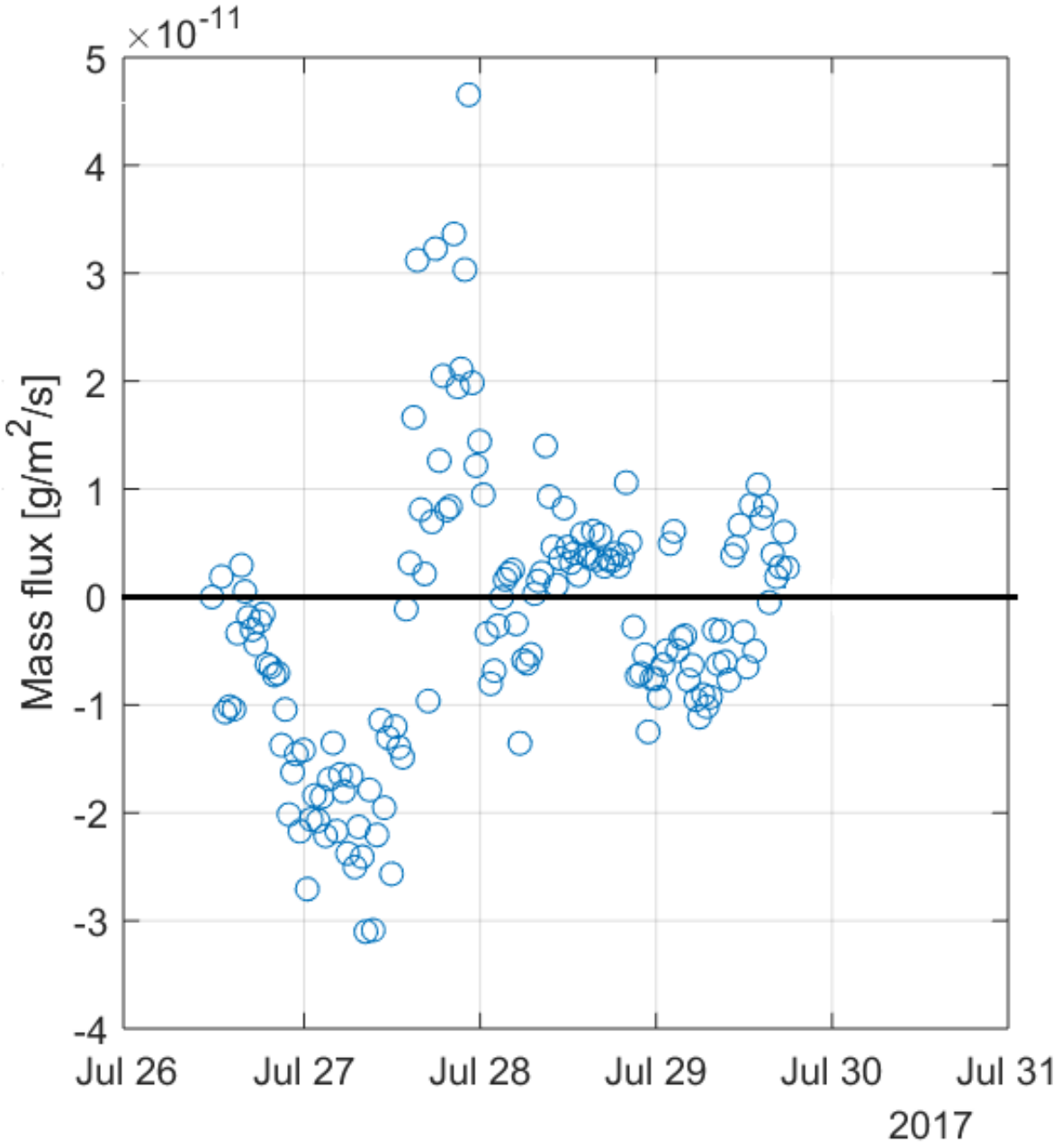

Figure 4.14: Total particle mass flux (55-1000 nm) as measured by the UHSAS at 31m.

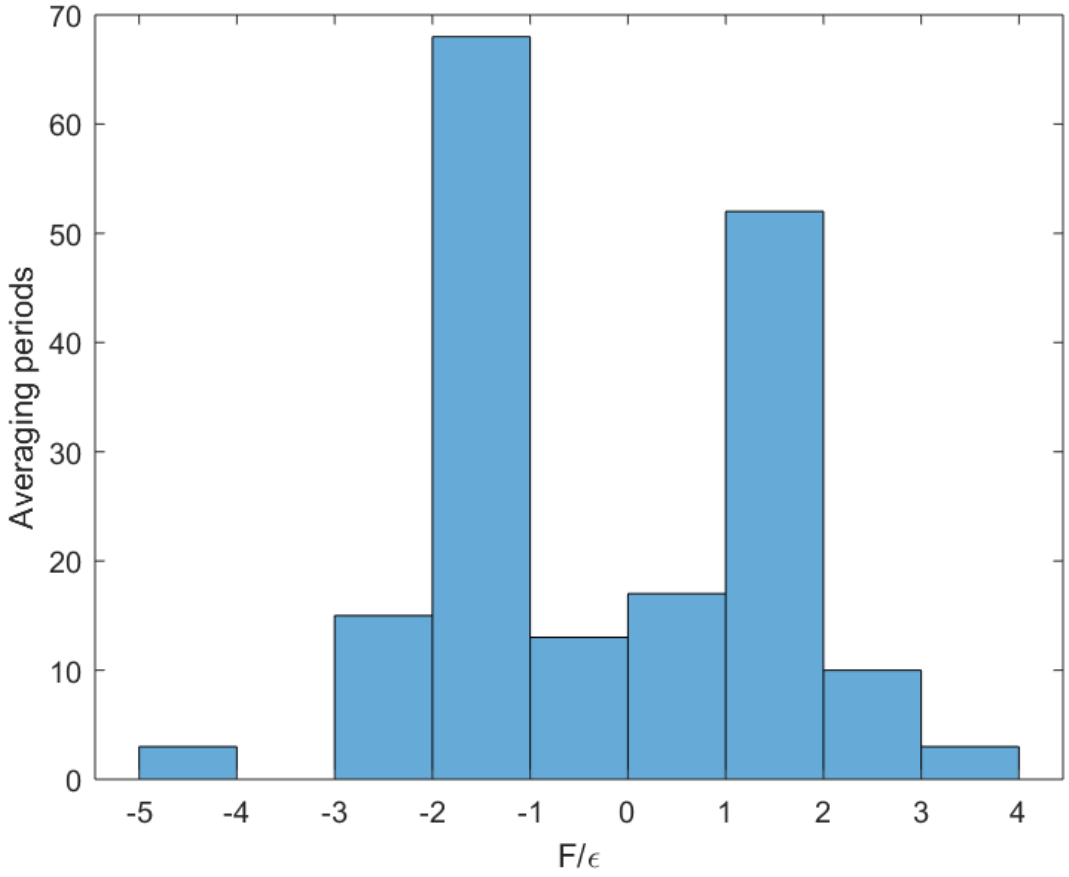

Figure 4.15: Distribution of F/ϵ for total particle mass flux (55-1000 nm). Measurements outside of ±2ε are considered significant.

Uncertainty analysis was performed on the fluxes obtained. As described in Gordon et al. (2011), the standard error of particle fluxes is given by

$$\epsilon^2 = 2\frac{\int_0^n R_F \mathrm{d}\tau}{T_a} \tag{10}$$

where R_F is the autocorrelation of flux measurements, τ is the time lag, and n is the first zero crossing of R_F.

Fluxes are considered significant if they fall outside of two standard errors. A distribution of F/ϵ is plotted in **Figure 4.15**. 17 % of particle fluxes were outside of ± 2ε, meaning that 17 % of particle fluxes were significant. More downward than upward particle fluxes were significant by a factor of 1.4.

Aerosol fluxes will be further examined and discussed in **Section 5.3**.

4.3 Heat, gas, and momentum flux

Investigation of the mixing and exchange of heat, gases, and momentum may help in characterising the mixing and exchange of aerosols. Although the behaviour of these quantities differs somewhat from that of aerosols, with different densities, states, and modes of deposition, they can be used to infer the state of mixing in the canopy (e.g. Thomas and Foken, 2007). Thus, research into the mixing of these accurately measurable quantities is of value in the investigation of exchange in a forest canopy. In addition, there are more projects that focus on heat, gas, and momentum exchange which are in forests similar to that near the YAJP site (e.g. Baldocchi et al., 1997, which described the energy balance in a jack pine forest in Manitoba; and Jarvis et al., 1997, which explored gas exchange and mixing in a Saskatchewan mature black spruce forest). Therefore, comparison of measurements of heat, gas, and momentum will allow us to compare the measurements at our site with those obtained at other sites.

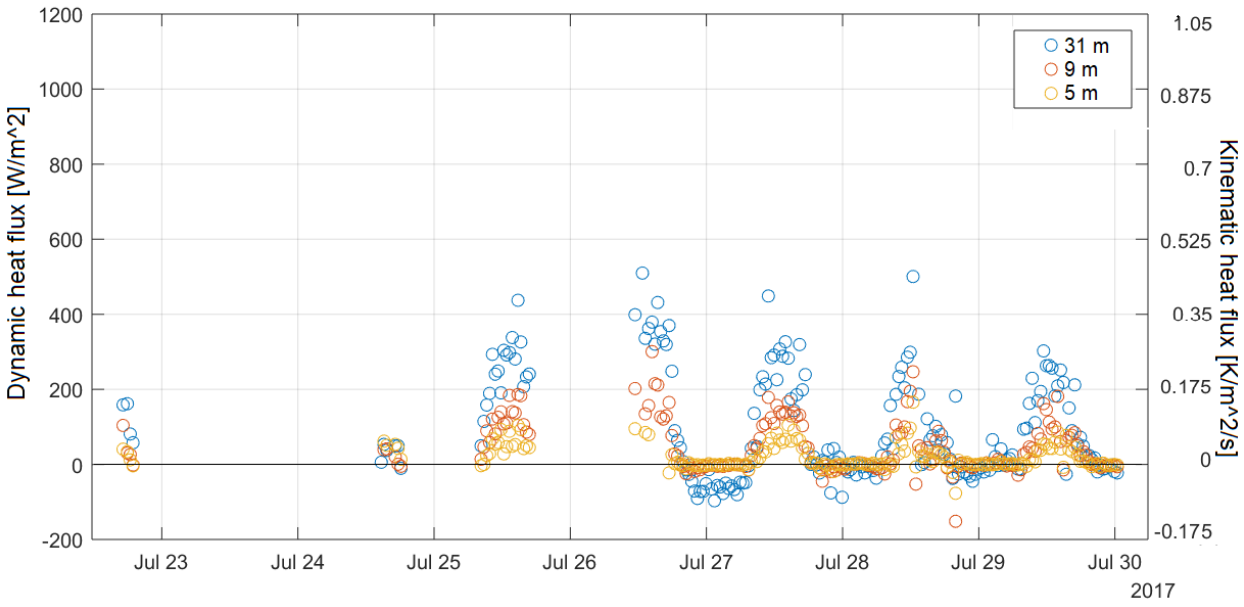

Figure 4.16: Heat flux, dynamic (corrected for temperature and pressure). Approximate kinematic flux values are given on the right axis and are accurate to within 5%.

Sensible heat flux is the vertical transport of thermal energy through the direct heating of the air by the ground. It represents a large part of the energy budget. The sensible heat flux at the YAJP site is plotted in **Figure 4.16**. During the day, heat flux values are generally positive; they approach 400 W/m^2 at their maximum on a typical day. For comparison, 400 W/m^2 is between 80% and 90% of the maximum net radiation in July at the site, with the rest lost as latent heat (in the form of H_2O vapour flux), radiated away, or stored in the ground.

These values are higher than other projects in the boreal forest. Baldocchi et al. (1997) measured values of around 90 W/m^2 of sensible heat flux over a jack pine forest in southern Saskatchewan in late July, when averaged over one day. This value was approximately 75% of the sensible heat flux observed during the study period at the YAJP site. Also, in Jarvis et al. (1997),

mid-day sensible heat values were around 230 W/m^2, about 55% of those observed at the YAJP site. YAJP sensible heat flux values were more consistent with some other projects in equatorial regions (e.g. Yakir, 2013, where values were measured in the forests of the Sahel; and Denmead and Bradley, 1985, in a ponderosa pine forest in Australia).

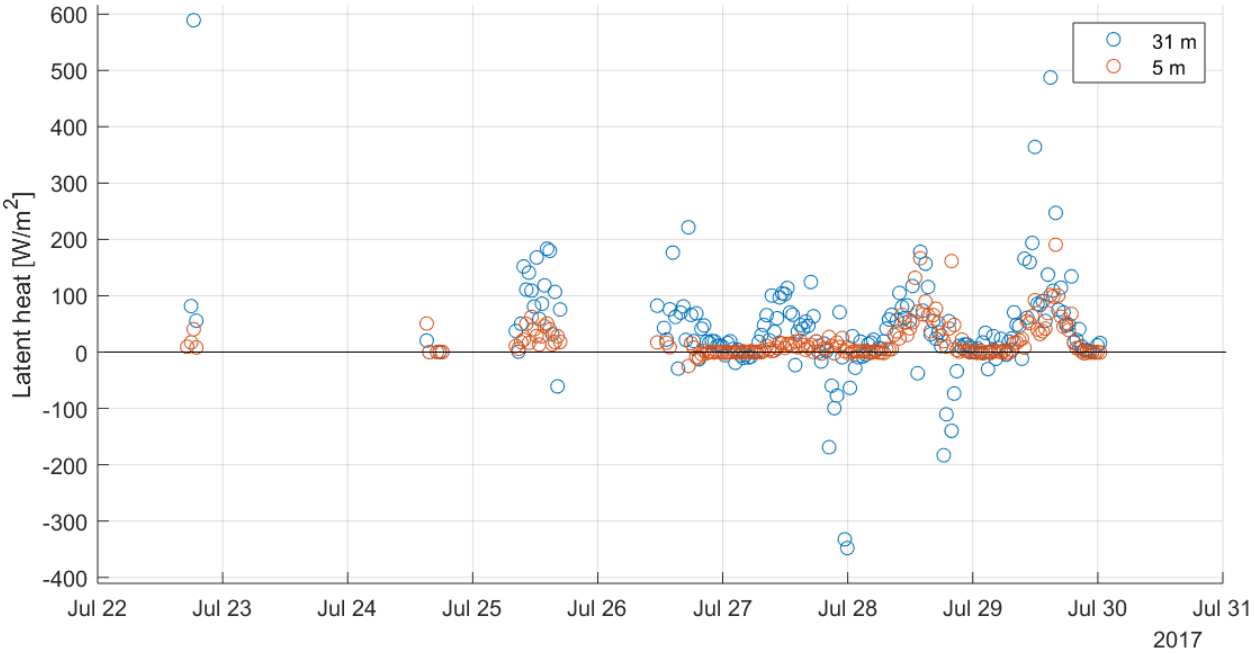

Figure 4.17: H_2O latent heat flux.

The ground at the YAJP site was generally dry and well drained, with no understory, whereas Jarvis et al. (1997) noted that the surface at their site was generally wet. This could be the reason for the disparity between sensible heat flux measurements at our site and theirs. It was noted in Rotenberg (2013) that a dry forest could be responsible for large sensible heat fluxes, as latent heat fluxes would be unavailable. In many forests, especially those with a moist ground and an understory, latent heat will be more prevalent. YAJP latent heat values (**Figure 4.17**) are slightly higher than in the Yatir forest

project (ibid), but not nearly as high as those presented in Jarvis et al. (1997), the flux study closest to YAJP in location.

The Bowen ratio (Bowen, 1926), defined by $Bo = H/L$, where H is the sensible heat flux and L is the latent heat flux, is an indicator of soil humidity and is a useful quantity in modelling the humidity in the surface layer and the soil (Carson, 1982). In the YAJP forest, while it varied day-to-day, a typical value during the campaign was Bo = 3, higher than was observed in Jarvis et al. (1997) and Baldocchi et al. (1997). However, after a period of rain during the campaign, Bo over the forest briefly attained a value of 0.5 before increasing again. In the month after the campaign, Bo was generally around 1.5.

At night, heat flux values are close to zero. Note that only the top level anemometer exhibits values significantly below zero at nighttime, especially prominent the night of July 26. This is a result of the crown radiating heat at night, creating a cool layer which means heat flux is into that layer. Below the crown, there is no such effect, so the lower levels see no heat flux at night.

Momentum flux is the transport of horizontal wind velocity. Since the wind speed usually increases with height, momentum flux is expected to be into the canopy. It is predicted that momentum flux increases exponentially with height within the canopy and logarithmically above the canopy, with possible positive momentum fluxes caused by a local maximum in wind speed (Bailey et al., 1997). Typical values of momentum flux in a deciduous canopy were presented in Evans (2008). For a wind speed of 4 m/s above the canopy, values of approximately -1 m^2/s^2 were measured.

Figure 4.18 shows the momentum flux for all levels. The middle anemometer was located in the crown, the top anemometer was above the canopy, and the lower anemometer was in the trunk space. Above the canopy, momentum flux attains its minimum value of around -1 m^2/s^2 during the day and is near zero during the night. In the crown and the trunk space, the momentum flux was

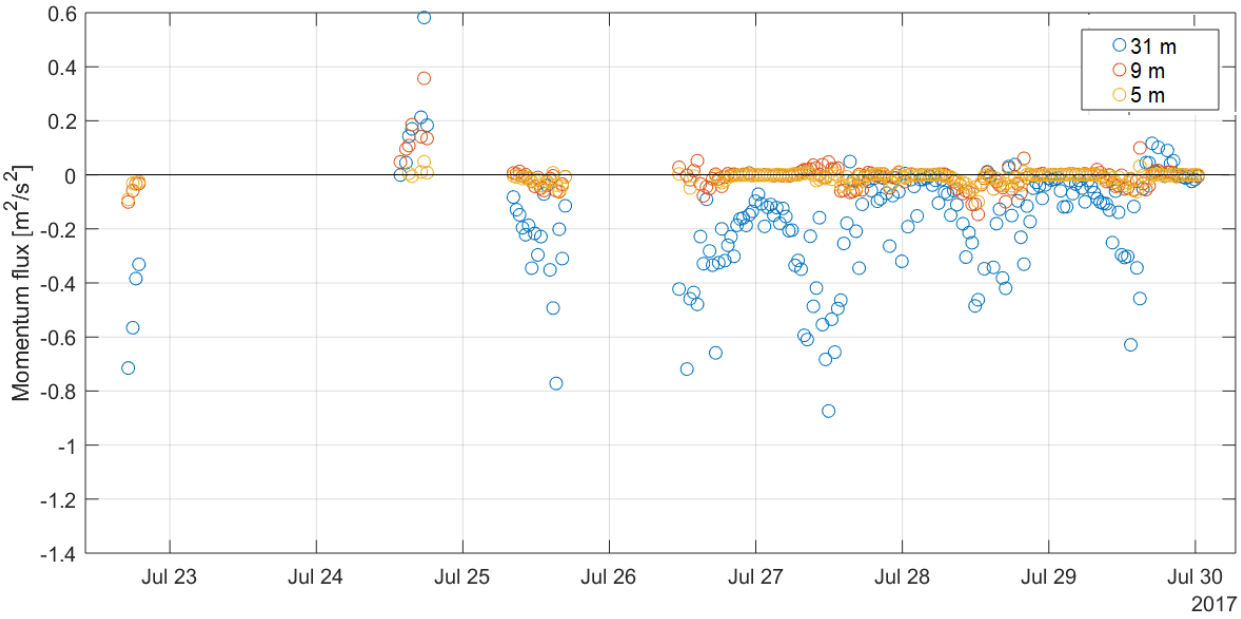

Figure 4.18: Momentum flux.

much closer to zero, with minimum mid-day values of around −0.1 m^2/s^2.

A momentum flux into the canopy, as was predicted and observed, is consistent with increasing with speed with height. Plotted in **Figure 4.6** is the mean wind speed after rotation. It is clear that the average wind speed increases with height, although the increase in speed between the lower and middle anemometer is slight, owing partly due to the small vertical distance between the anemometers and partly due to the crown exerting more drag on the wind at a height of 9 m but less drag at a height of 5 m.

H_2O and CO_2 gas fluxes are plotted in **Figures 4.19 and 4.20.** These have been subject to a Webb correction. Some points in the CO_2 flux series have been removed because they violate stationarity assumptions of eddy covariance, an example of which can be seen in **Figure 4.21.** Detrending the series is not possible in this instance because the concentration change in CO_2 is too

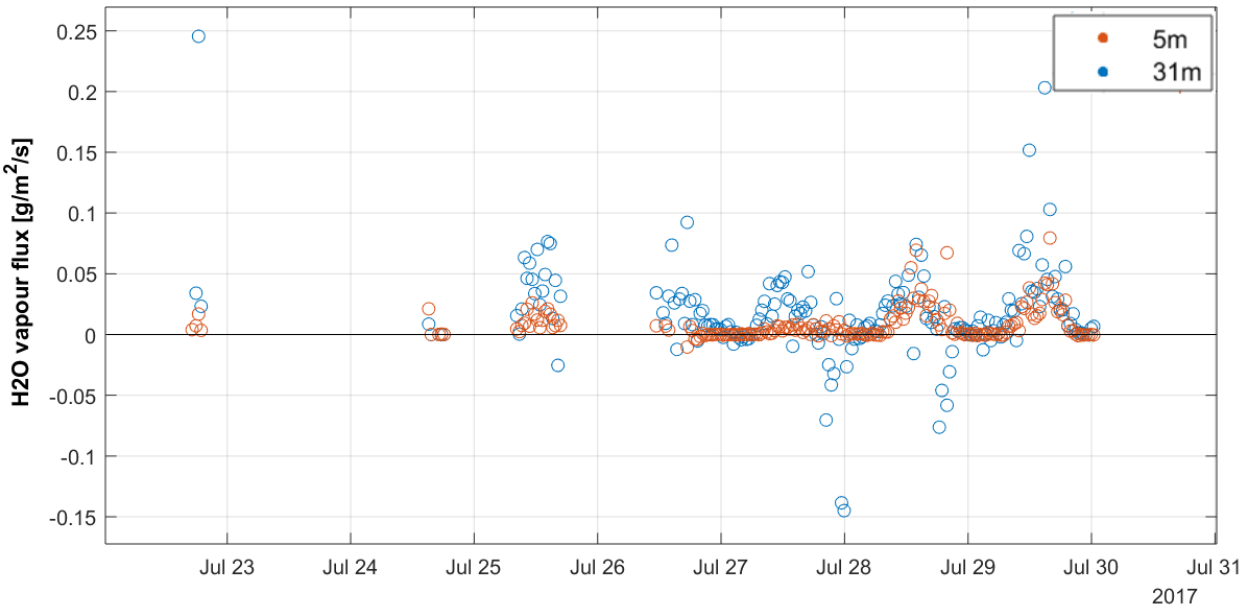

Figure 4.19: Water vapour flux.

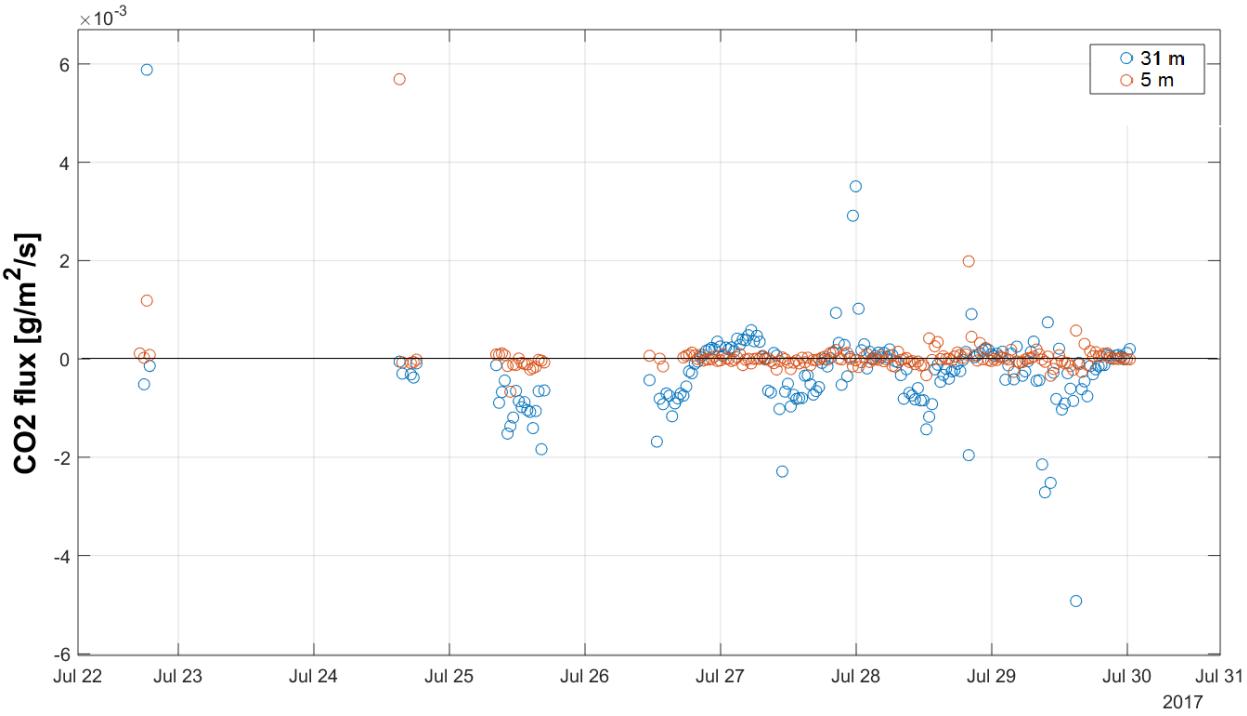

Figure 4.20: CO_2 flux.

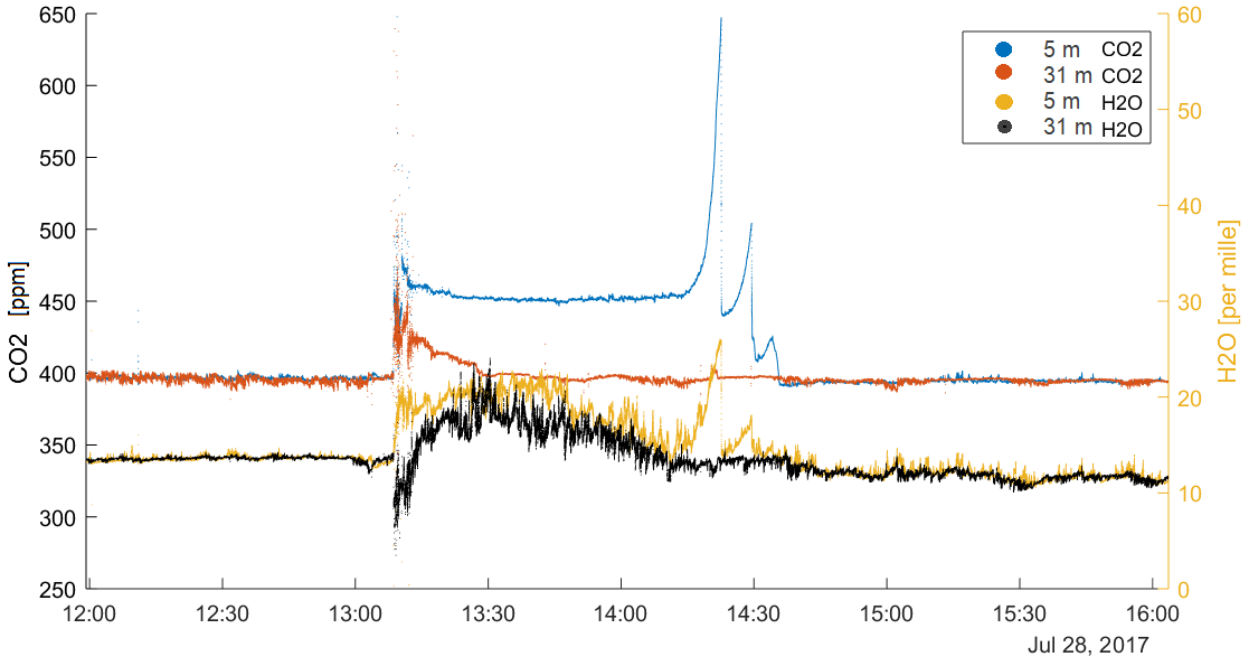

Figure 4.21: A period where eddy covariance will not produce accurate fluxes. The rapidly changing concentration of CO_2 at 13:10 and at 14:20 violates stationarity assumptions.

rapid.

CO_2 fluxes are generally negative during the day and positive during the night. This is a result of photosynthesis, whereby trees take up CO_2 during daylight hours and eject CO_2 during the night. Thus, the concentration of CO_2 in the canopy is lower during daylight hours and higher during the night.

The flux of CO_2 as measured by eddy covariance serves as an upper limit for the sink of carbon over a forest (Grünwald and Bernhofer, 2007). Integrated over a typical day, the flux of CO_2 through the canopy at YAJP is -4 g/m^2 of CO_2 per day during the July 2017 campaign period, similar to July values observed in a boreal forest in Malhi et al. (1999), who observed a July average of -3.4 g/m^2 of CO_2 flux into a boreal forest.

4.4 Energy spectra

Figures 4.22–24 are representative energy spectra for all levels at midday. As predicted by Kolmogorov (1941) for isotropic 3D turbulence, they should feature a $f^{-5/3}$ slope in the inertial subrange ($f^{-2/3}$ when scaled by frequency). The energy spectrum at a height of 31 m has an inertial subrange extending into high frequencies but the spectra at heights of 9 m and 5 m have energy input into high frequencies.

As was described in **Section 1**, energy spectra within canopies are modified by canopy elements. Through interaction with leaves and branches, turbulent kinetic energy is input to smaller scales. Since the upper anemometer is outside of the canopy sub-layer, we do not expect the spectrum at a height of 31 m to be affected at all by the canopy. But in the crown, canopy effects on the energy spectrum may be large enough to resolve with the middle anemometer.

A spectrum for the crown (9 m) without normalisation by frequency is presented in **Figure 4.25**, along with the spectrum at a height of 31 m for comparison. At a height of 9 m, a prominent flattening out is present at frequencies around 1 Hz, and the

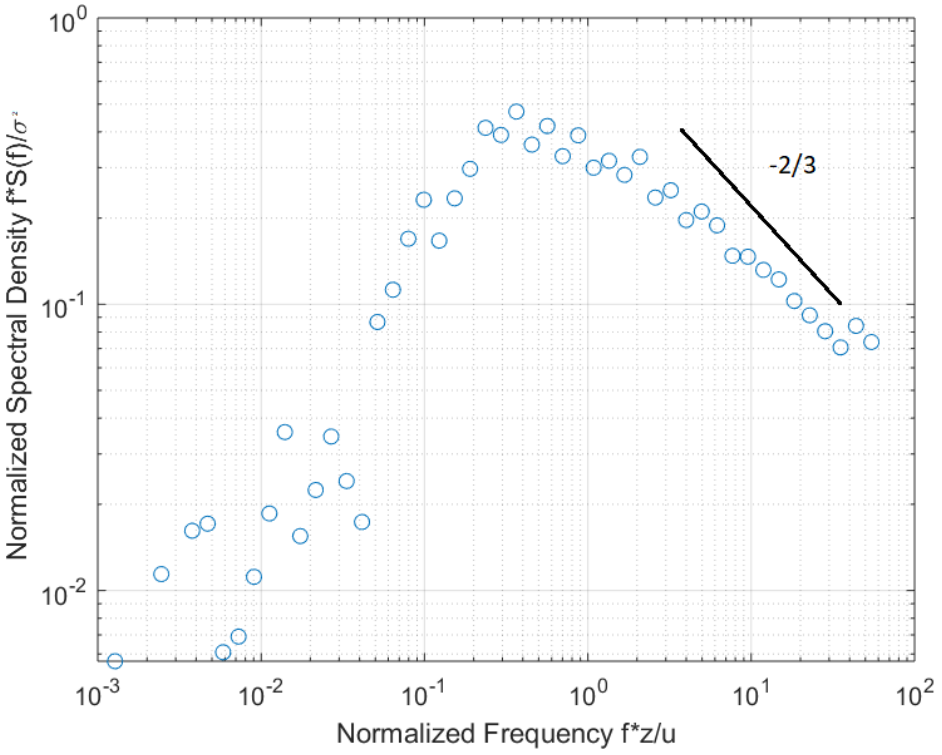

Figure 4.22: Normalised energy spectrum at a height of 31 m.

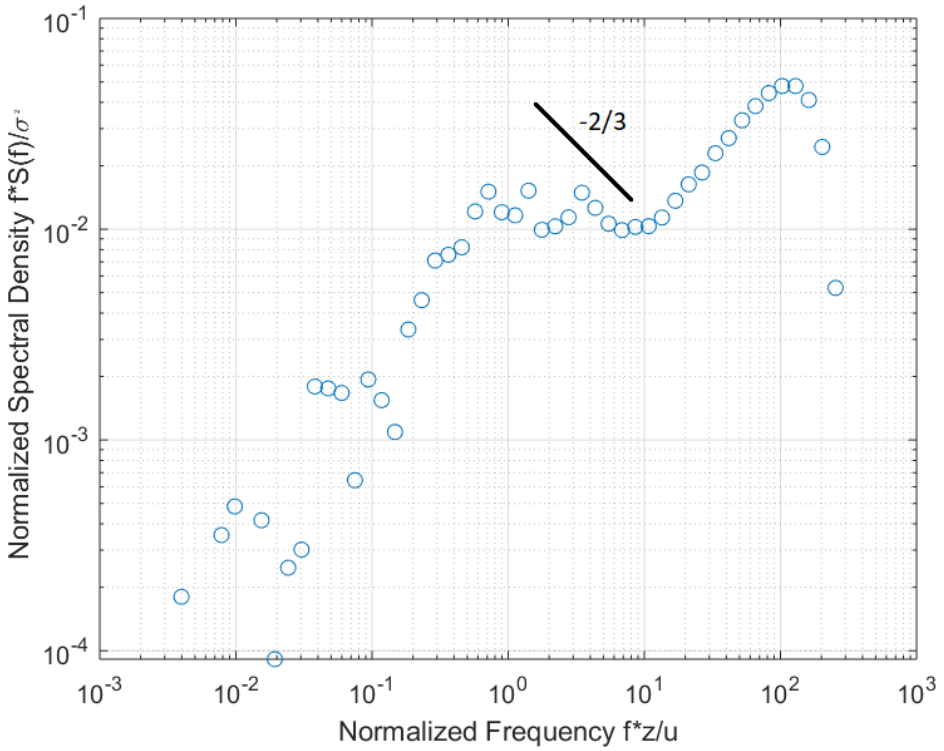

Figure 4.23: Normalised energy spectrum at a height of 9 m.

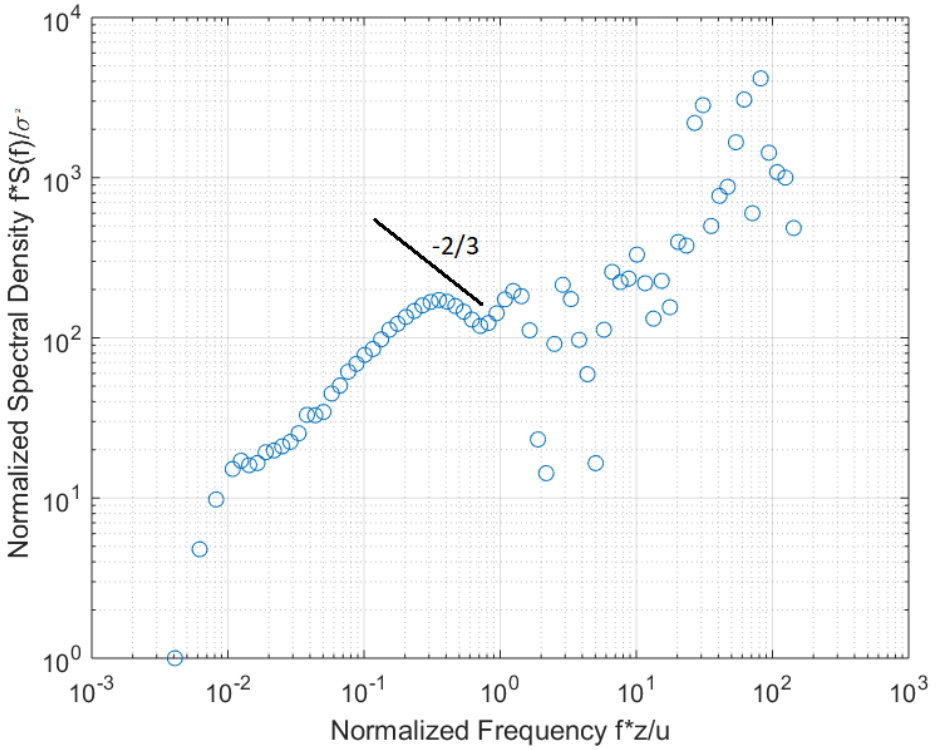

Figure 4.24: Normalised energy spectrum at a height of 5 m.

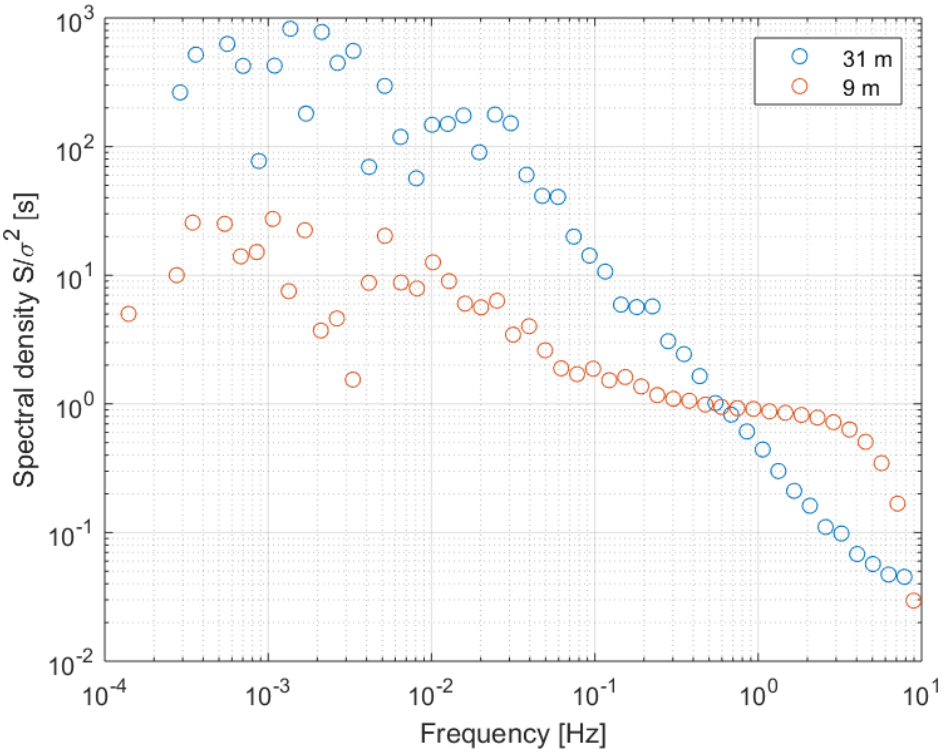

Figure 4.25: Energy spectra at heights of 9 m and 31 m, normalised by total energy (σ^2 = 7.8 m^2/s^2 at a height of 31 m and σ^2 = 0.9 m^2/s^2 at a height of 9 m during this period) but not scaled by frequency. Spectra taken July 28 at 11 AM to 11:30 AM.

beginnings of a steep drop back to the standard cascade at frequencies approaching 10 Hz. Contrast with the energy spectrum for the top anemometer, which does not have an energy input into the inertial subrange except by the cascade process.

The spectra in this section show that forest canopies affect the transfer of turbulent kinetic energy. It is reasonable, then, to expect forests to affect the mixing and deposition of aerosols.

4.5 Other spectra

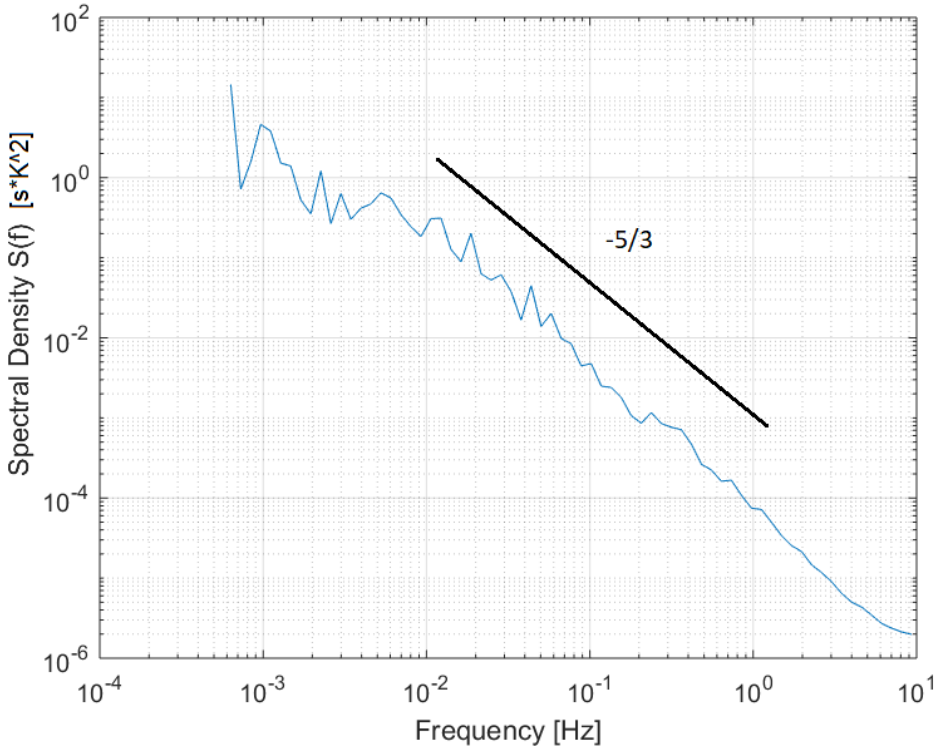

Figure 4.26: Potential temperature spectrum at a height of 5 m.

Potential temperature spectra in forests are not well characterised, as described Kaimal and Finnigan (1994) and Finnigan (2000). They are expected to exhibit a $k^{-5/3}$ slope in the inertial subrange, just like over land outside canopies. The

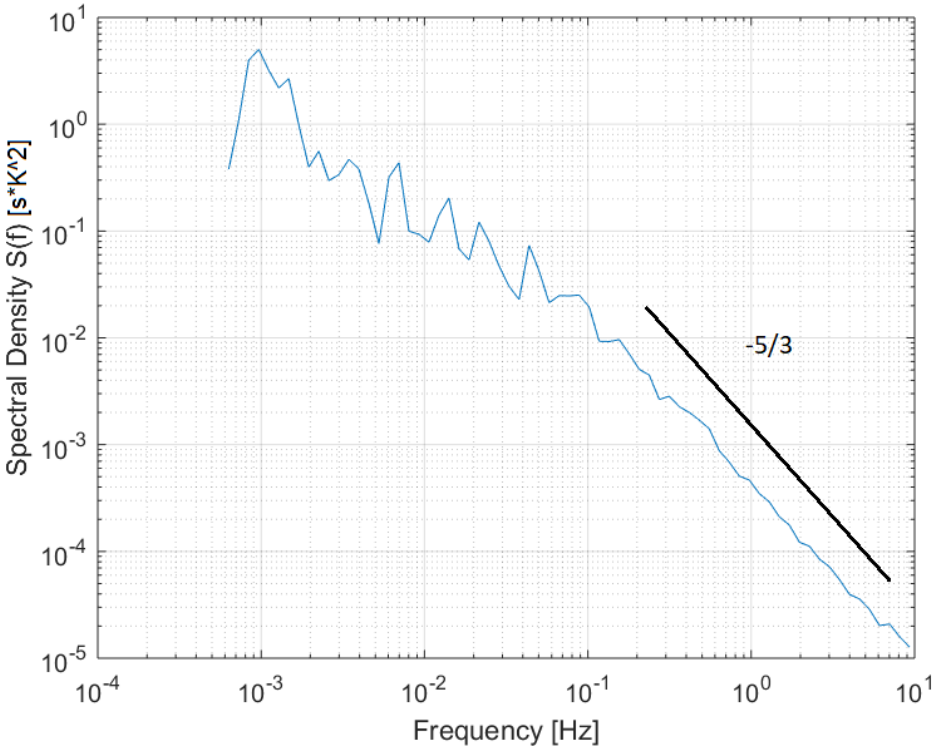

Figure 4.27: Potential temperature spectrum at a height of 31 m.

potential temperature spectrum within the canopy during a mid-day averaging period on a sunny day is shown in **Figure 4.26.** It exhibits a $f^{-5/3}$ slope over an inertial subrange of more than three decades, comparable to the potential temperature spectrum at the YAJP site above the canopy during the same period (**Figure 4.27**). Thus, there is little effect of the canopy on the potential temperature spectrum at the YAJP site.

For cospectra, in the inertial subrange, a $f^{-4/3}$ slope is expected for all passive scalars, which all cospectra here presented are assumed to be. Of particular interest (Kaimal and Finnigan, 1994) are cospectra of u'w', which have been predicted to have a $k^{-7/3}$ slope in the inertial subrange ($k^{-4/3}$ if normalised), and of $w'\theta'$, which have been predicted to have a $k^{-7/3}$ slope as well.

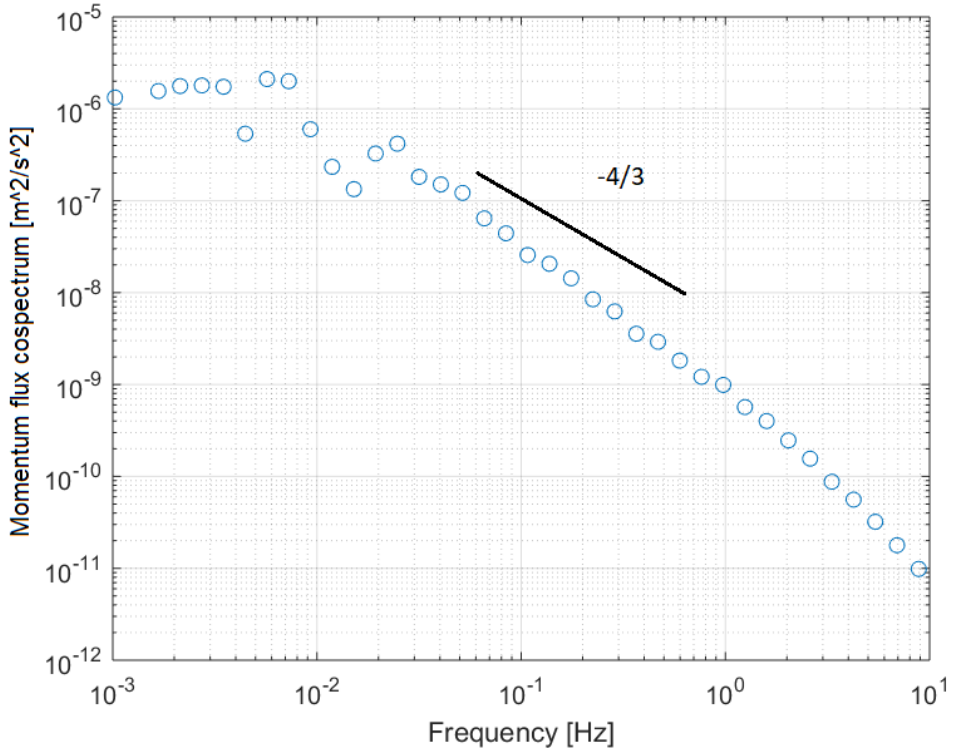

Figure 4.28: Momentum flux cospectrum at a height of 5 m, multiplied by frequency.

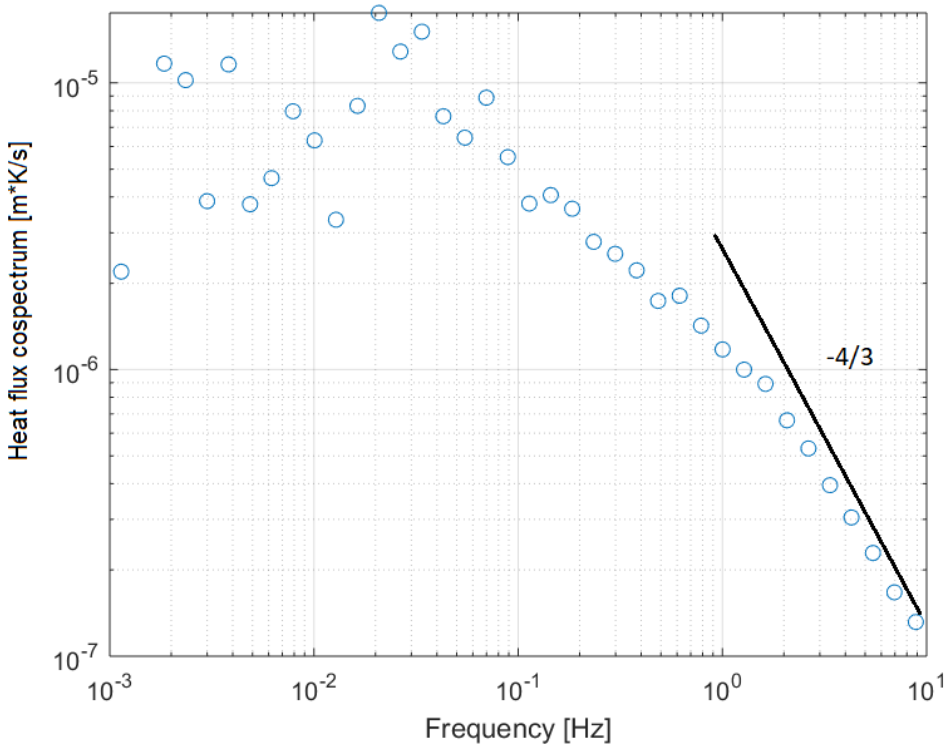

Figure 4.29: Heat flux cospecturm at a height of 5 m, multiplied by frequency. Heat flux measured with sonic anemometer, subject to SND correction.

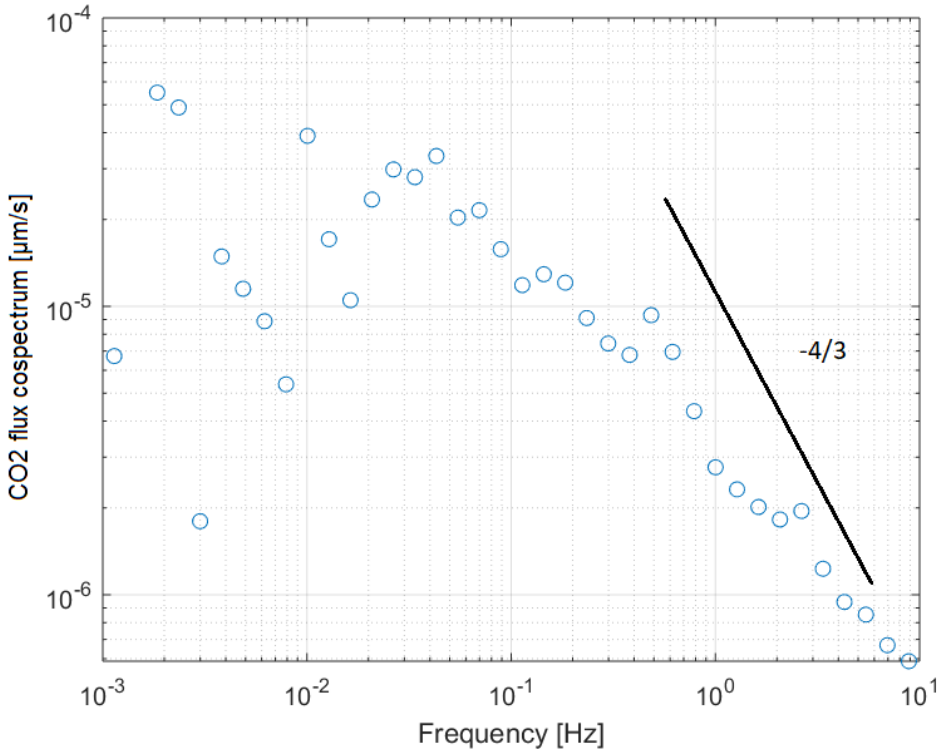

Figure 4.30: CO_2 flux cospectrum at a height of 5 m, multiplied by frequency.

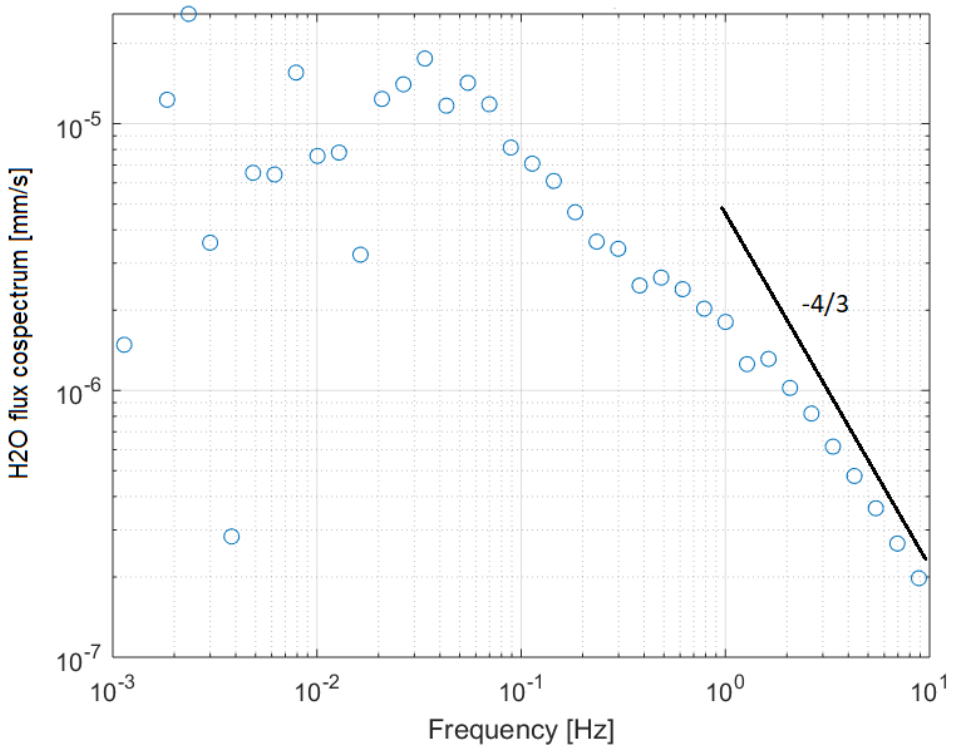

Figure 4.31: Water vapour flux cospectrum at a height of 5 m, multiplied by frequency.

In **Figures 4.28–31** are cospectra for momentum, heat, and gas fluxes at a height of 5 m. Contrast with **Figures 4.32–35**, which are the same quantities at the top level, unaffected by the canopy. These spectra were all taken from the same morning averaging period.

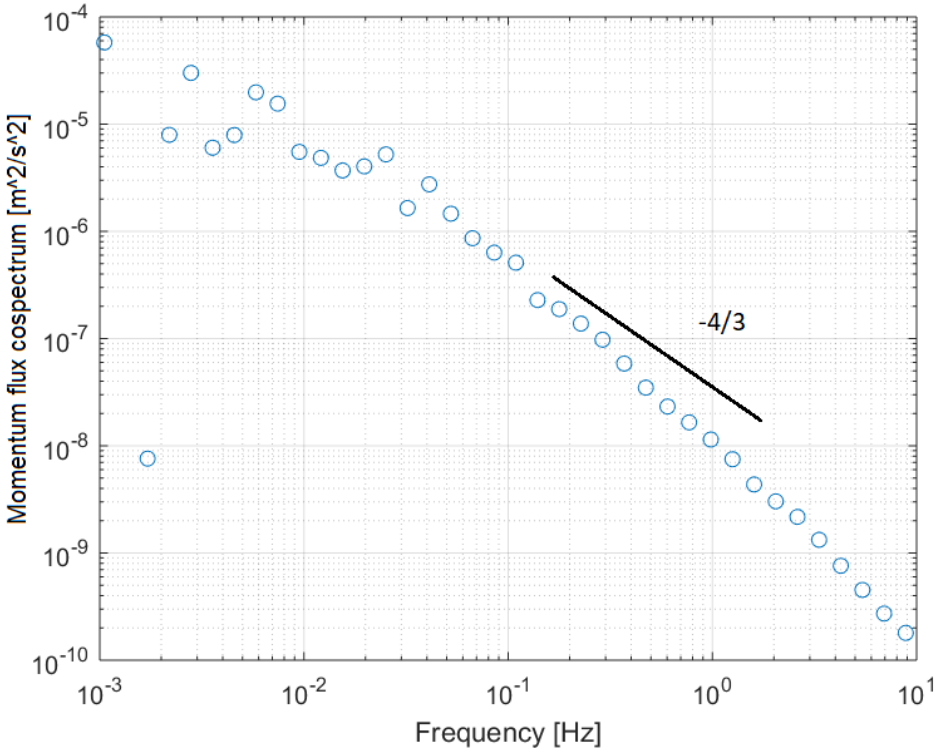

Figure 4.32: Momentum flux cospectrum at a height of 31 m, multiplied by frequency.

Figure 4.28 shows the cospectrum of momentum flux in the canopy as measured by the lower anemometer. It is steeper than expected, with approximately a k^{-2} slope. In theory, we expect a $k^{-4/3}$ slope when multiplied by frequency. This is in contrast to Amiro (1990) who measured a shallower than expected k^{-1} slope for the cospectrum of momentum flux in a similar pine forest in Manitoba. However, the cospectrum of momentum flux above the canopy, as measured with the top anemometer(**Figure 4.32**), is comparable to that of the lower anemometer. It exhibits a slope

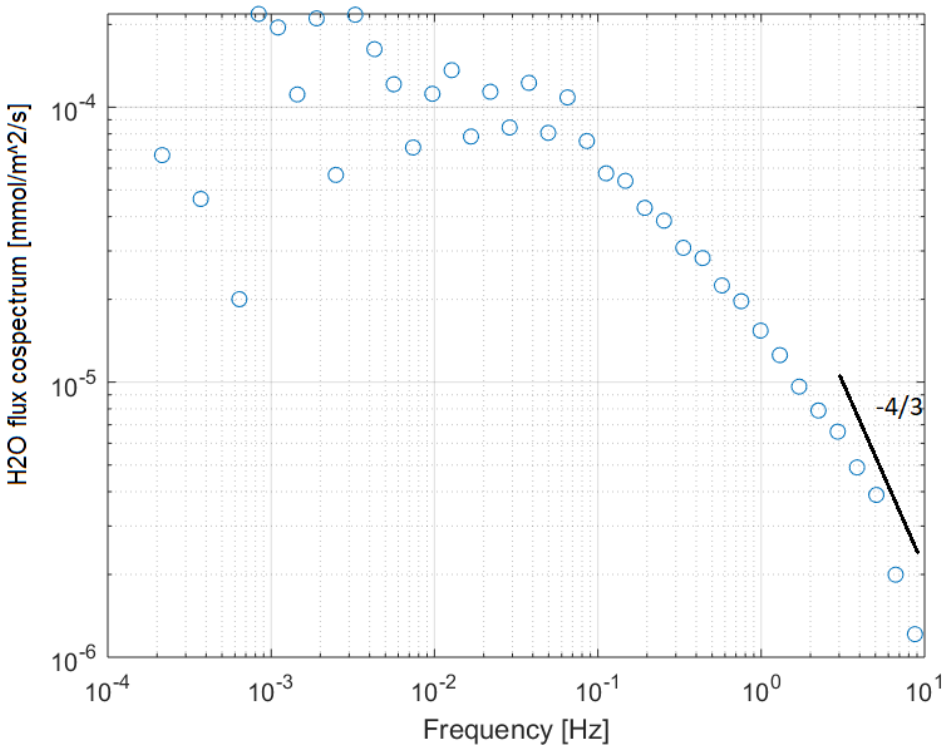

Figure 4.33: Water vapour flux cospectrum at a height of 31 m, multiplied by frequency.

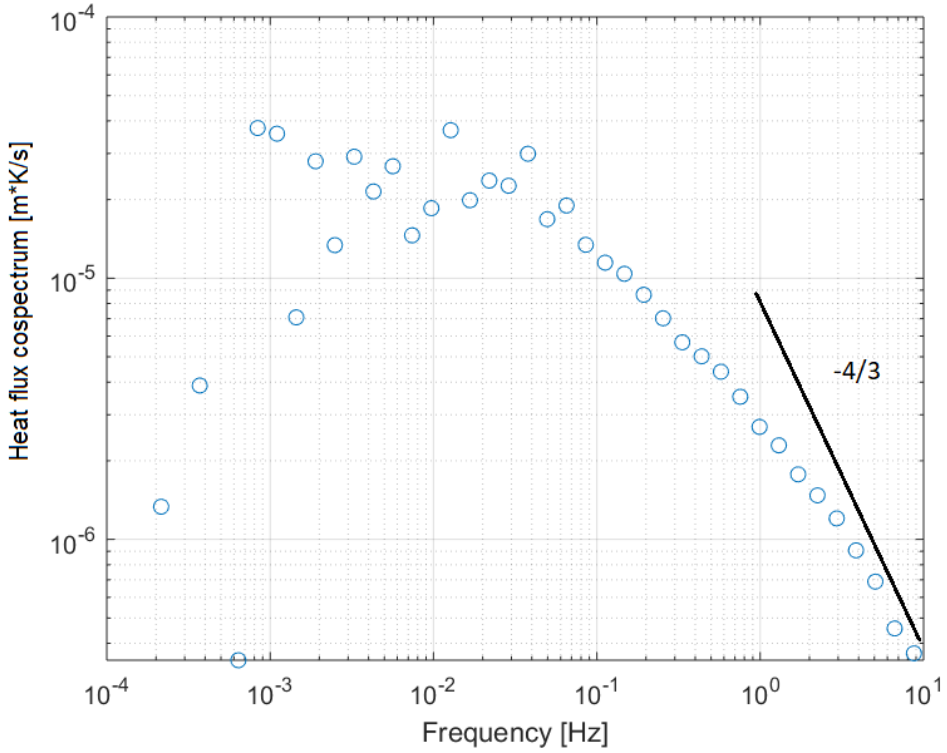

Figure 4.34: Heat flux cospectrum at a height of 31 m, multiplied by frequency. Heat flux measured with sonic anemometer, subject to SND correction.

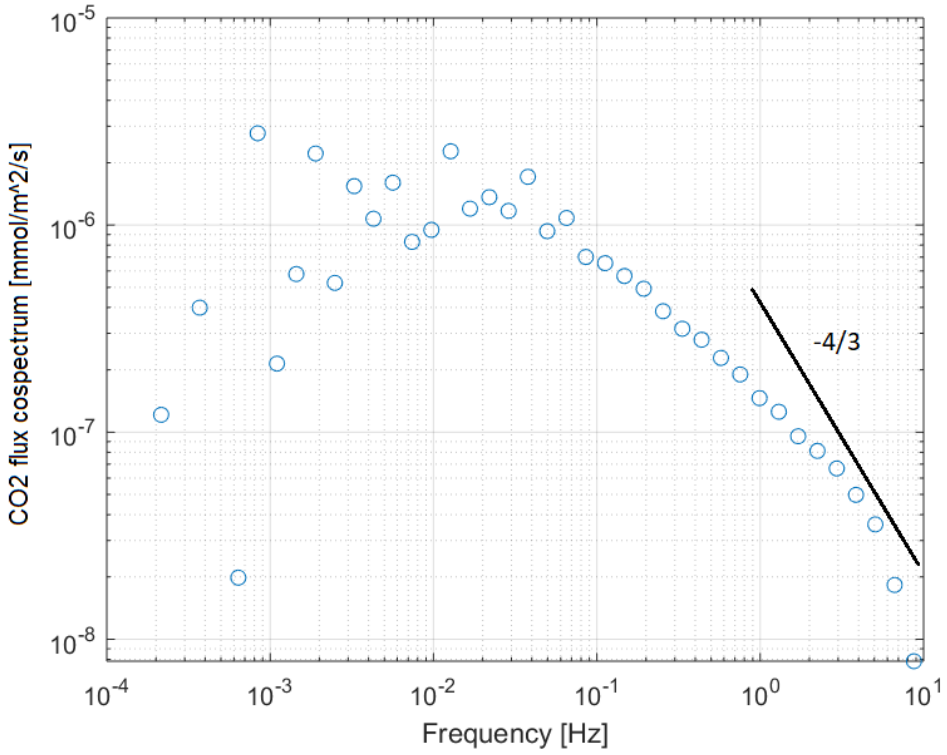

Figure 4.35: CO_2 flux cospectrum at a height of 31 m, multiplied by frequency.

slightly shallower than the k^{-2} slope observed within the canopy.

In **Figure 4.29**, the $w'\theta'$ cospectrum in the canopy as measured by the lowest anemometer exhibited a $k^{-4/3}$ slope, the same slope as observed above the canopy at the YAJP site (**Figure 4.34**) and in theory without a forest canopy (Kaimal and Finnigan, 1994). Only at very high frequencies (f > 2 Hz) does the slope approach the $f^{-4/3}$ of the inertial subrange.

The cospectra of gas fluxes are similar at the the upper and lower levels. They both have a $f^{-4/3}$ slope at high frequencies. The cospectra above and below the canopy are similar, with one difference. At the upper level, they attain their maxima at around f = 0.02 Hz, meaning eddies of about 50 seconds transport the most gas fluxes. At the lower level, they attain their maxima at around f = 0.04 Hz, meaning eddies of about 25 seconds transport the most gas fluxes. It is well known (e.g. Garratt, 1992) that at greater heights scalars are transported more by larger eddies.

Finally, the cospectrum of aerosol flux is shown in **Figure 4.36**. This was the aerosol flux during a mid-day deposition period. Most aerosol flux that is being observed is at low frequency eddies of around 8 minutes. The inertial subrange slope of $k^{-4/3}$ is observed only over a small range, less than a decade. The $k^{-4/3}$ range occurring at such low frequencies indicates that it is possible what is being observed is not the inertial subrange at all, as other cospectra have their inertial subrange at higher frequencies around f = 0.1 Hz to f = 1 Hz.

As was shown, most of the YAJP cospectra measured match fairly well with theory, with momentum being steeper and gas fluxes being shallower. Aerosol flux was likely affected by line effects, which were discussed in **Section 3.7**.

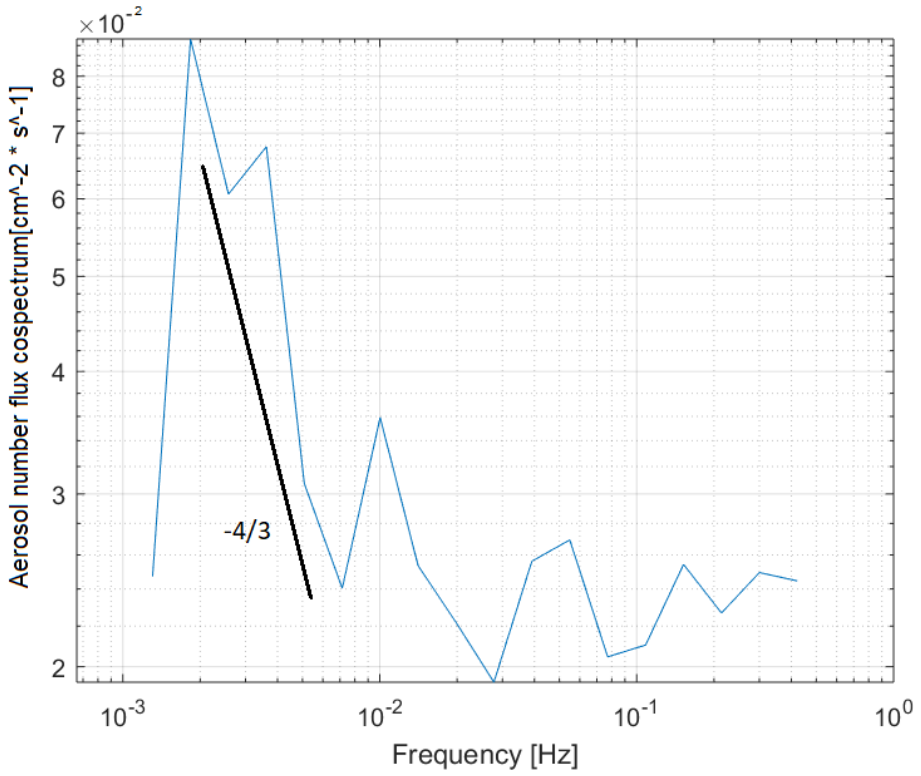

Figure 4.36: Aerosol number flux cospectrum at a height of 31 m.

5 Discussion

5.1 Sudden gas concentration changes

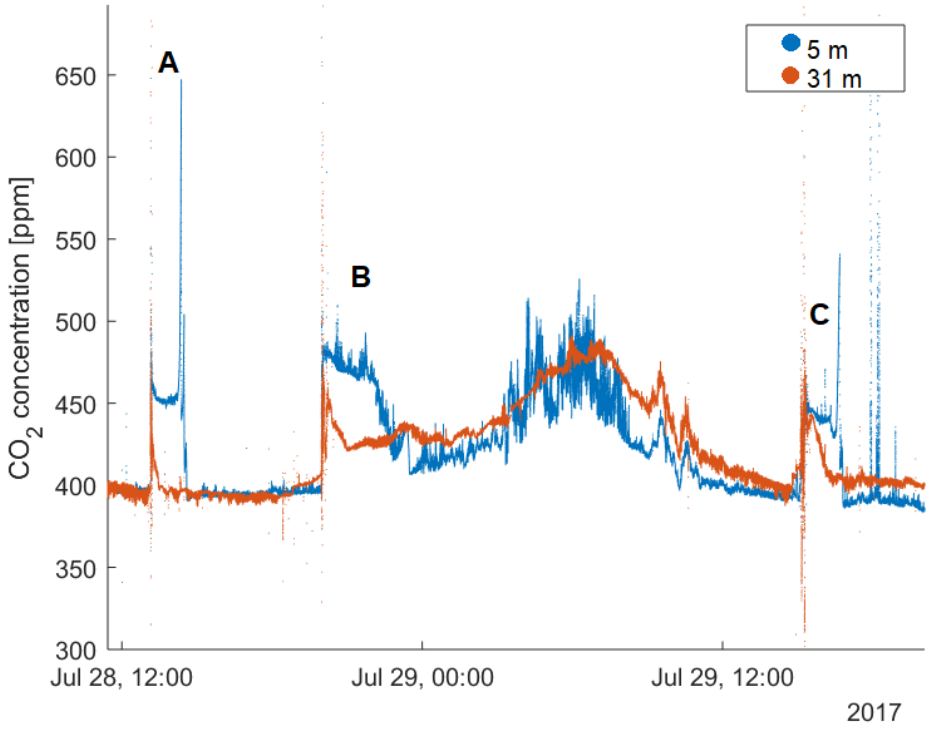

Figure 5.1: CO_2 spikes and plateaux observed during the intensive field campaign 2017.

On July 28 and 29, the gas analysers measured occasional sharp increases in [CO_2] which lasted for about 100 minutes, followed by sharp decreases in [CO_2]. These occurred simultaneously at the upper and lower levels. These events lasted between one and two hours before concentrations dropped back to the original values.

At the time indicated by point A in **Figure 5.1**, the CO_2 concentration at a height of 5 m rose sharply from 400 ppm then stayed level at 455 ppm for 75 minutes before dropping back to 400 ppm. At a height of 31 m, the CO_2 concentration increased to 440 ppm before gradually decreasing to the previous value of 400 ppm over the course of 20 minutes. At the time indicated by point

B, the CO_2 concentration rose in the same manner from 400 ppm to 480 ppm at the lower level and from 400 ppm to 470 ppm at the upper level. Again, the decrease in CO_2 concentration started immediately at the upper level (lasting 30 minutes before reaching a diurnal cycle value) but [CO_2] decreased only slightly over the course of two hours before decreasing to 415 ppm, an increase expected from the diurnal cycle of [CO_2]. At the time indicated by point C, [CO_2] increased at the lower level from 395 ppm to 440 ppm and remained there for one hour. At the upper level, the increase occurred at the same time but [CO_2] decreased immediately. This decrease was more gradual than at the times indicated by points A and B but [CO_2] still reached baseline values before the lower level did.

A close-up of episode A as seen through several measured quantities is presented in **Figure 5.2**. Near the beginning of the episode, there was an increase in wind speed and a rapid change in temperature. CO_2 concentrations exhibited rapid, extreme fluctuations. Unrealistically low (sub-baseline) values of [CO_2] during the spike were likely the result of an instrument issue, with light-deflecting material being in the path of the gas analyser for the reference measurement but out of the path for the actual measurement. At the end of the episode, CO_2 concentrations increased before sharply decreasing, then increased and decreased again, and again, then dropped to its original value.

During this episode, the sudden, sustained change in CO_2 concentration was also evident above the canopy, but not to as large of an extent. The decrease in concentration back to the baseline is more gradual and starts immediately. The wind direction at a height of 5 m where the elevated [CO_2] was sustained shifted from west to north; after the end of the episode they shifted from north back to west.

At the start of the episode, there was a rapid change in temperature, signifying mixing or a front. At the end of the

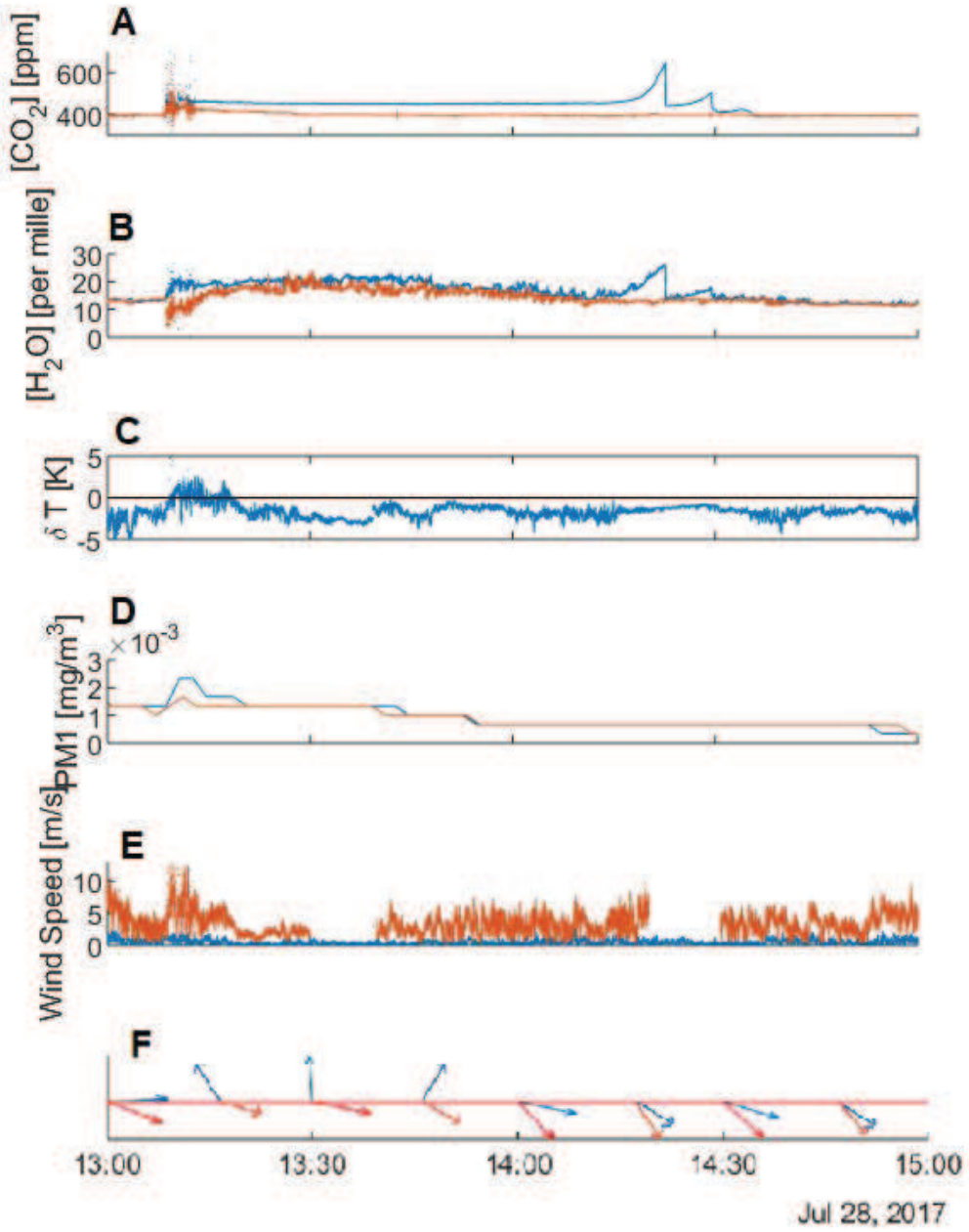

Figure 5.2: A CO_2 episode as analysed through A) Concentration; B) H_2O concentration; C) Temperature difference between the heights of 31 m and 2 m, which may indicate coupling; D) Particle concentration; E) Wind speed; and F) Wind direction. Blue lines are measurements made at a height of 5 m; orange lines are measurements made at a height of 31 m.

episode, the change in temperature was not as sharp as it was at the start of the episode. The temperature changes that are present could be attributed in part to latent cooling from the rainfall in the episode rather than being entirely an advected property of the air mass.

The episode had some hallmarks of a pollution plume. For example, there were elevated [H_2O] and [CO_2] readings, and each episode ended with [CO_2] exhibiting sawtooth-shaped ramps, which are characteristic of the trailing edge of a plume (Stull, 1988). However, it also had some signs against.

For one, [CO_2] below the canopy was greater than above the canopy. Typically, a plume having travelled 20 km from its source would be dispersed vertically such that concentrations over 26 m would not vary by so much. It is, however, possible that the canopy was decoupled and so the CO_2 at the lower level was unable to disperse. Also, the concentration of aerosols was low throughout the episode, as can be seen in **Figure 5.2D**. Even if there were few particles when the plume was emitted, after travelling for 20 km it would contain secondary organic aerosols, although, assuming a growth rate of several nm/h (d'Andrea et al., 2013) the majority of those particles would be smaller than the particle counter's detection limit.

Episode A was contemporaneous with rainfall. Entrainment and wet deposition of gases by the rain could have affected the concentration and mixing in the canopy of CO_2. Furthermore, the sudden concentration change in episode A could be due to a raindrop on the sensor window attenuating the signal measured. However, this interpretation is unlikely for three reasons. One, [CO_2] at the beginning of the episode increases at the same time at the bottom and the top. Raindrops falling onto the windows of both instruments at the same second, while possible, is unlikely. Two, at the end of the episode, the increase in [CO_2] at the bottom was contemporaneous with a slight increase of the same at the top, so if a purported raindrop had evaporated or slid off,

it would have had to have done so on both sensors at the same time. Three, episodes B and C were not associated with rain, so it would be unlikely that water would be in the instrument's path during those episodes.

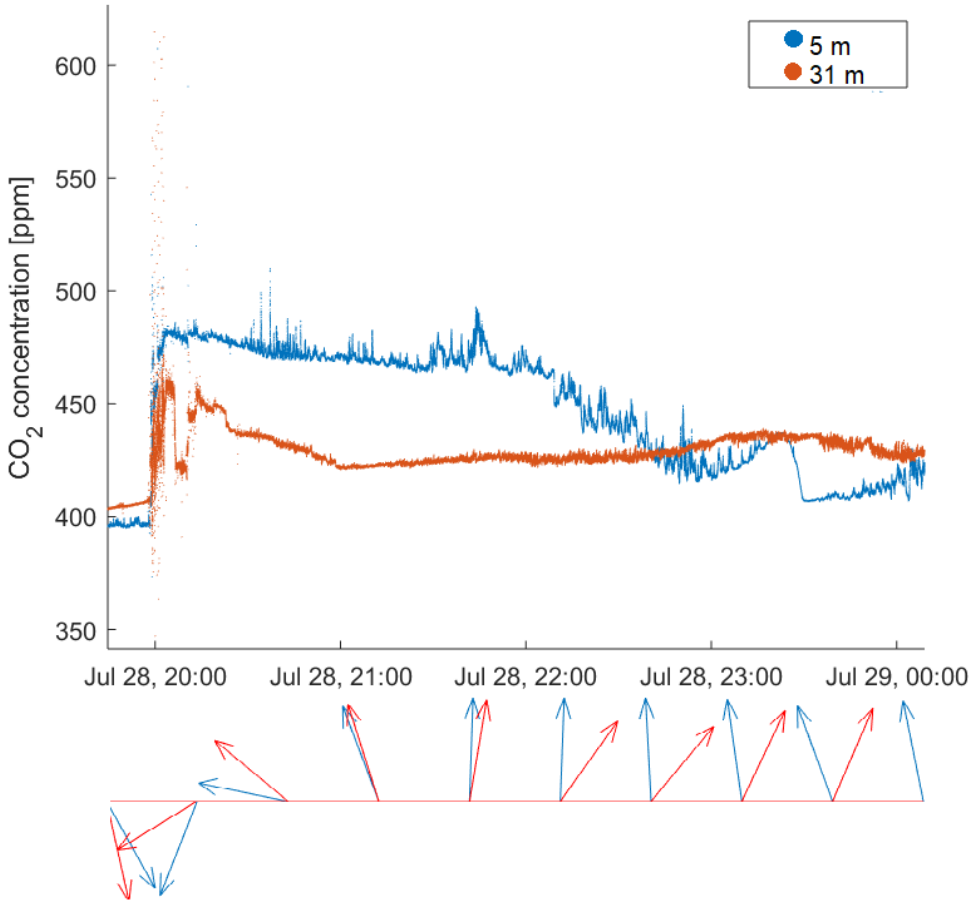

Figure 5.3: Episode B CO_2 concentration at heights of 5 m and 31 m. Note the gradual decrease as opposed to the ramping up and sudden decrease in other episodes.

Episodes B (**Figure 5.3**) and C (**Figure 5.4**) were similar to episode A. Episode B's conclusion did not exhibit the ramping up and subsequent sharp decreases like the other episodes, but rather a gradual decrease over the course of an hour followed by one relatively slow increase and decrease to the baseline. Also, the increase in [CO_2] in episode C is not as sudden as the

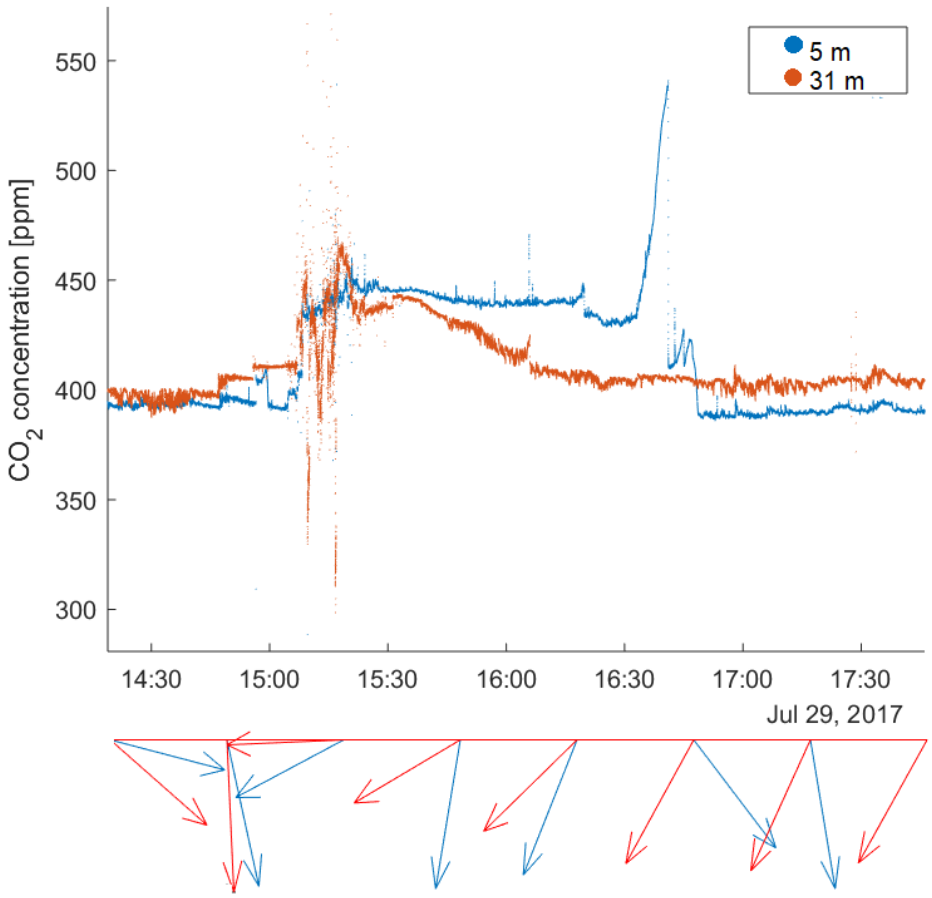

Figure 5.4: Episode C CO_2 concentration at heights of 5 m and 31 m.

increases observed in the other episodes. However, aside from these slight differences, episodes A and B exhibited the same characteristics as episode A analysed in **Figure 5.2.**

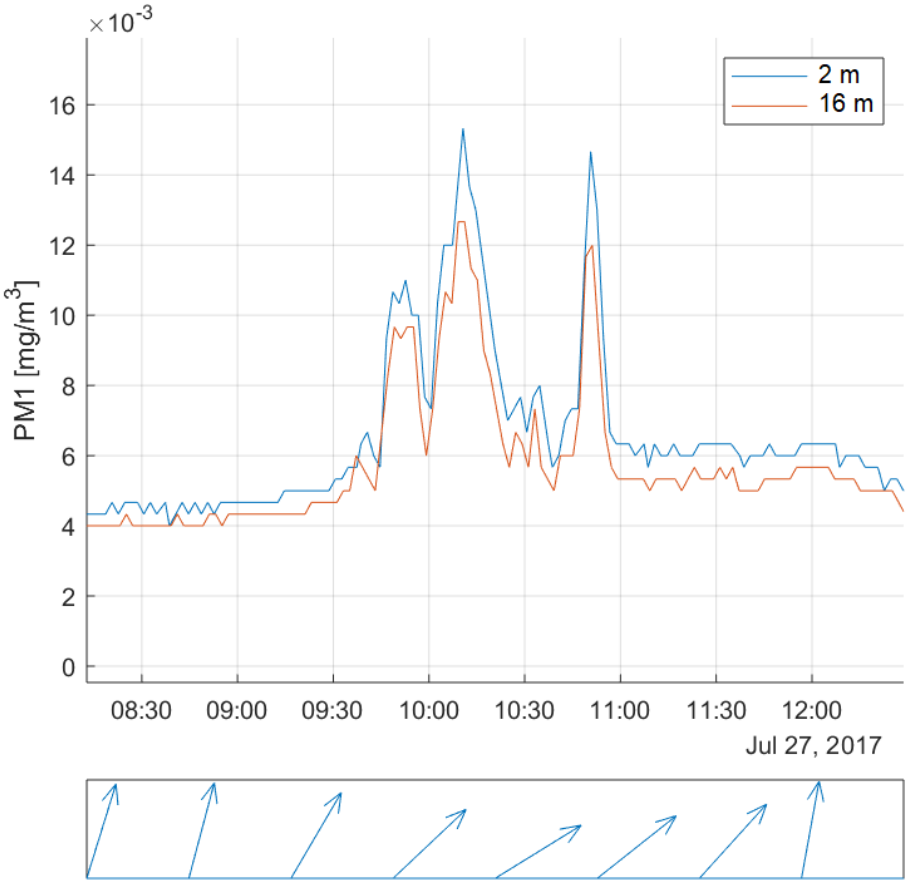

Figure 5.5: Particle counter readings and wind direction during a deposition event. Elevated concentrations of particles were not sustained. Note the slight lag between levels decreasing as the episode went on.

If these episodes did indeed represent the decoupling and subsequent coupling of the canopy, then they would offer a glimpse into how pollutant concentrations behave in the canopy. At a fixed point, one would expect to observe a sharp increase in concentration as deposition begins, followed by a plateau and a series of increases and sharp drops as the canopy is cleared. According to particle counter measurements in the canopy, such

was not the case (**Figure 5.5**). Elevated concentrations of particles were at no point sustained for extended periods of time, instead frequently increasing and decreasing and mixing well with particles above the canopy. This suggests a different deposition mechanism for particles than for CO_2, which is taken up by leaves and brush rather than attaching to canopy elements and the ground.

5.2 Coupling in the canopy

Forest canopies modify mixing and deposition of pollutants. In a forest canopy, turbulent energy is dominated by eddies the length scale of the height of the canopy (Finnigan, 2000). Thus, the mixing of passive scalars such as aerosols is also dominated by those length scales (ibid). In addition, canopies affect the process of deposition, and the crown can also be a deposition surface (Kaimal and Finnigan, 1994).

The extent to which these effects are present depends on the state of coupling in the canopy. When the canopy is not coupled with layers above, it may take longer for a plume above the canopy to mix down below, whereas mixing into the canopy occurs rapidly when the canopy is coupled.

Using $[H_2O]$ as a tracer, we can determine when the canopy is coupled. While H_2O is not entirely a passive tracer, given that its molar mass is different from that of dry air, it is present only in small amounts in the air. The resulting increase in buoyancy is often considered negligable, such that water vapour is sometimes used as a passive scalar to determine coupling in forests (Foken, 2008). **Figure 5.6** shows $[H_2O]$ over a 24-hour period. When $[H_2O]$ values suddenly become close together, we assume that the canopy is coupled, and when the concentrations drift apart, we assume that the canopy is decoupled. For example, point A indicates a time when the canopy is decoupled from the atmosphere above, and point B indicates a time when the canopy is coupled.

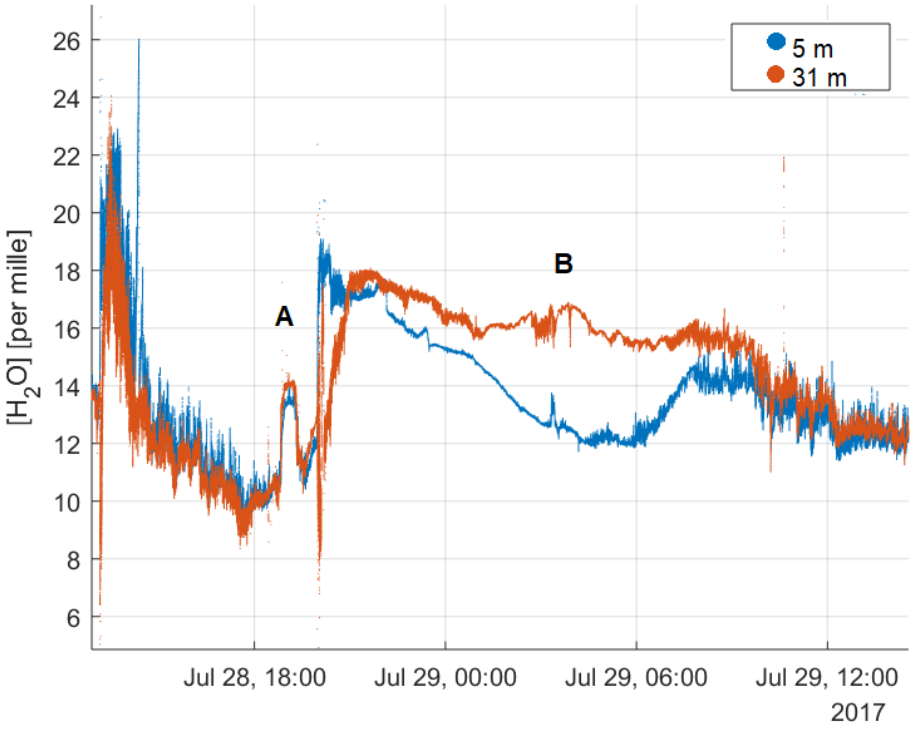

Figure 5.6: Water vapour concentration. At point A, the canopy is considered coupled; at point B, the canopy is considered decoupled.

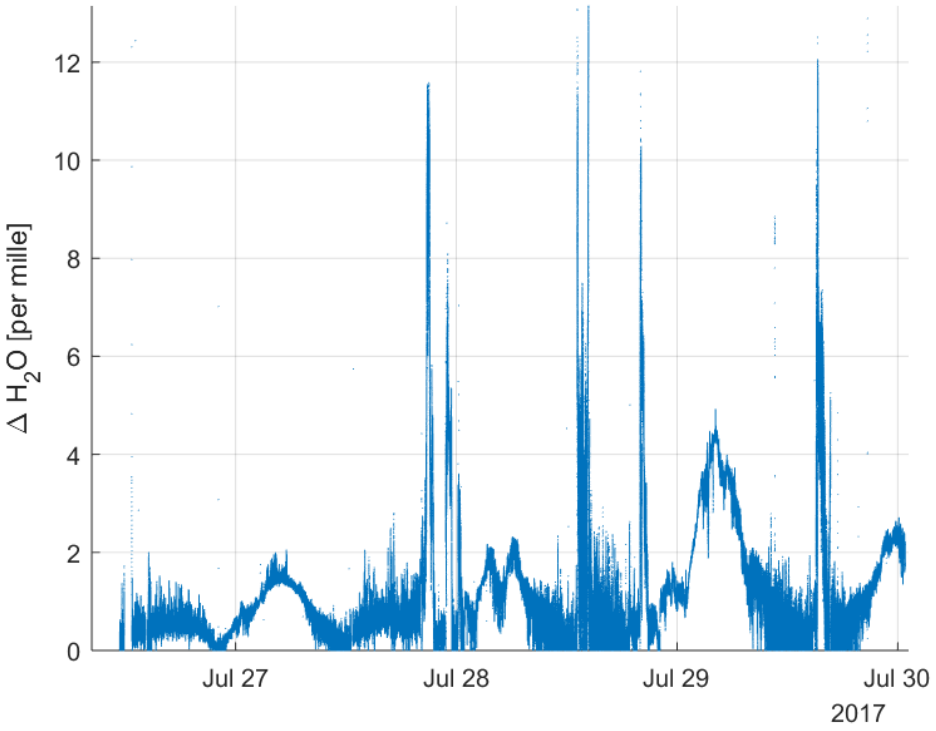

Figure 5.7: The difference of the concentration of water vapour at 31 m and 5 m. From this quantity we can infer the degree of coupling in the canopy.

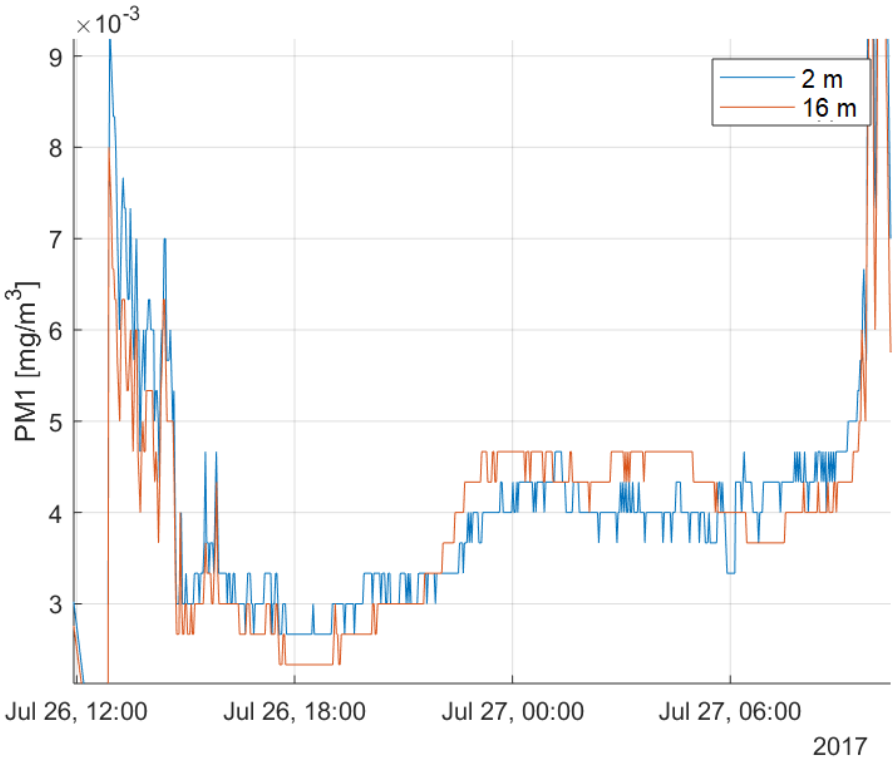

Figure 5.8: Particle counter concentration, showing that the particle counter above the canopy leads the particle counter below.

From this we can produce an estimate of the state of coupling of the canopy by taking the magnitude of the difference between [H_2O] at the different levels. It is shown in **Figure 5.7.** Note the strong diurnal cycle in the coupling. Generally, the canopy is more likely to be coupled with the atmosphere above during the day, and unlikely to be so coupled at night. This is because, during the night, the canopy experiences little turbulent mixing due to stable stratification. During the day, the sun shining leads to heating of the ground and canopy elements, introducing buoyancy to canopy air and inducing mixing. More heating as the day goes on leads to more rapid mixing in the canopy through the early afternoon. As the sun sets, the canopy cools and becomes stable once again.

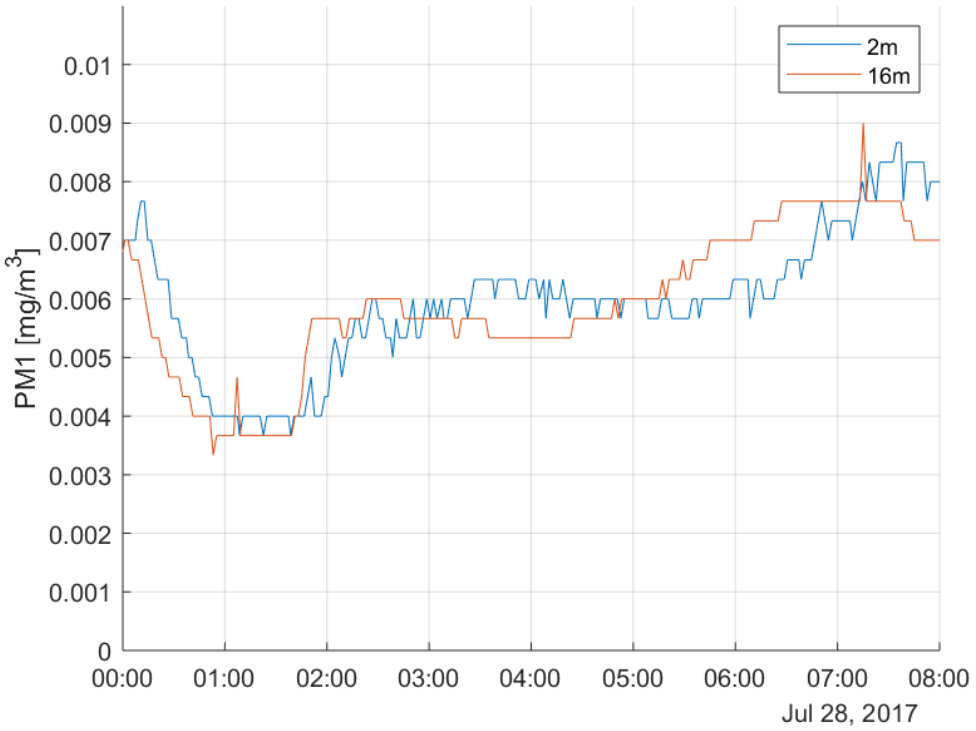

Figure 5.9: Particle counter particle mass concentration during a calm night, showing a long lag between the upper and lower levels.

Using particle counter data from two different levels

(**Figure 5.8**), we find that the aerosol number concentration from the top of the canopy leads the concentration at the bottom of the canopy. The difference between the two levels correlates with the difference in [H_2O] (r=0.72).

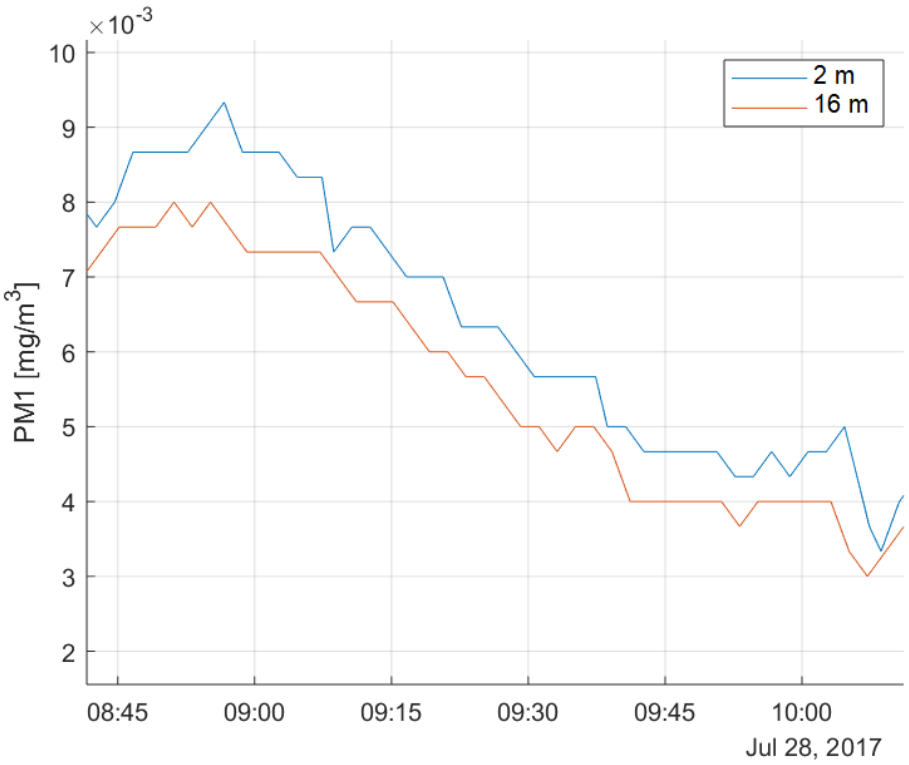

Figure 5.10: Particle counter concentration during a morning where the canopy was decoupled, with lags in concentrations of up to 14 minutes. At 9:30 the canopy became more coupled and the lag decreased to 4 minutes.

Coupling affects the time it takes for pollutants to reach ground level in forests. During a deposition episode on the morning of July 27, the bottom particle counter lagged behind the top particle counter by 2 minutes, this time decreasing as the episode went on to noon (**Figure 5.5**). Also, as can been seen in **Figure 5.9**, the upper particle counter's reading (at the canopy height) preceded the lower one's (near ground level) by 50 minutes during the night.

The degree of coupling is related to the degree of stratification of the canopy. During the night, when the canopy was stratified, it took almost one hour for pollutants to mix down from the canopy; during the afternoon, it took less than two minutes. During a period where the canopy was decoupled during the day, it took 14 minutes for pollutants to mix down to ground level (**Figure 5.10**), compared to a typical mid-day value of less than 2 minutes.

In Gordon et al. (2011), average time lag between particle concentrations at heights of 33 m and 2 m was calculated for different hours of day. During the night, they found that the lag was a median of 120 minutes. During the late afternoon, there was no lag between the two levels. Similarly, in Whitehead et al. (2010), median time lag between the heights of 47 m and the forest floor were 105 minutes in the hour before dawn but under 2 minutes at noon.

The longer mixing times during the night at the Borden forest may have been because of differences between it and the YAJP forest. The YAJP forest is purely coniferous, whereas the Borden forest is mixed. Also, the Borden forest has denser foliage, with an LAI of 4, compared to the YAJP forest with an LAI of approximately 2.

The results measured at YAJP suggest that, like in the other studies discussed above, the forest canopy inhibited exchange more during the night and less during the day. In other words, it was more often decoupled during the night and coupled during the day. This means that plumes during the night take longer to penetrate a canopy at night but readily mix during the day. Since the mixing of aerosols into the forest is a significant source of their deposition, this implies that, over forests, aerosols have a longer lifetime in the atmosphere at night than during the day. In other words, we are more likely to find aged aerosols after a night or a period of decoupling than we are during periods of coupling.

5.3 Downward aerosol fluxes

Fluxes of aerosols into forest canopies are common in areas close to emission sources, like the YAJP site. They are important to characterise for a threefold reason: aerosol deposition affects a forest's health (Matsuda, 2017), forests can be a sink of aerosols so areas downstream receive fewer aerosols, and studying aerosol deposition into a forest canopy can help characterise the deposition into other canopies, like urban canopies (Petroff et al., 2008).

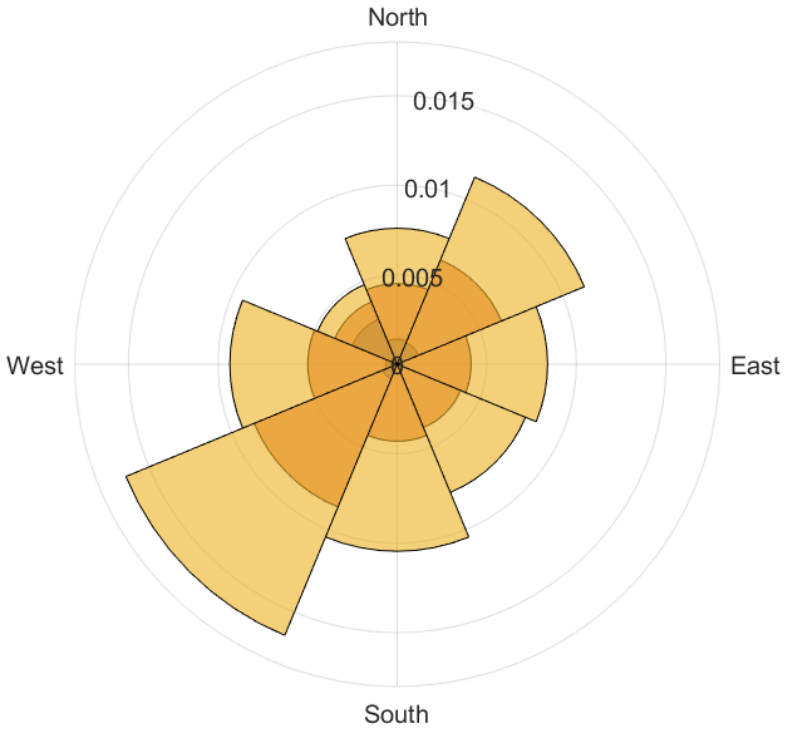

Figure 5.11: Mean PM1 concentration at a height of 16 m by wind direction [mg/m^3] with ± 1 standard error. NE bin has only three datum points. Wind directions have similar mean concentrations except SW and NE.

During the intensive field campaign, several periods of deposition were observed (see **Figure 4.14** for a time-series of particle fluxes). These came from a number of different aerosol

sources. As was previously shown in **Figure 2.3**, aerosols could come from one of a few suspected sources. The mean particle concentration by wind direction is shown in **Figure 5.11**. As expected, southwest winds were associated with higher particle concentrations, probably due to the Syncrude operations, which are a large producer of aerosols. More surprising is the NE quadrant showing high mean particle concentration, but since there were only three datum points from that direction that were not discarded because of the generator, it is likely not significant.

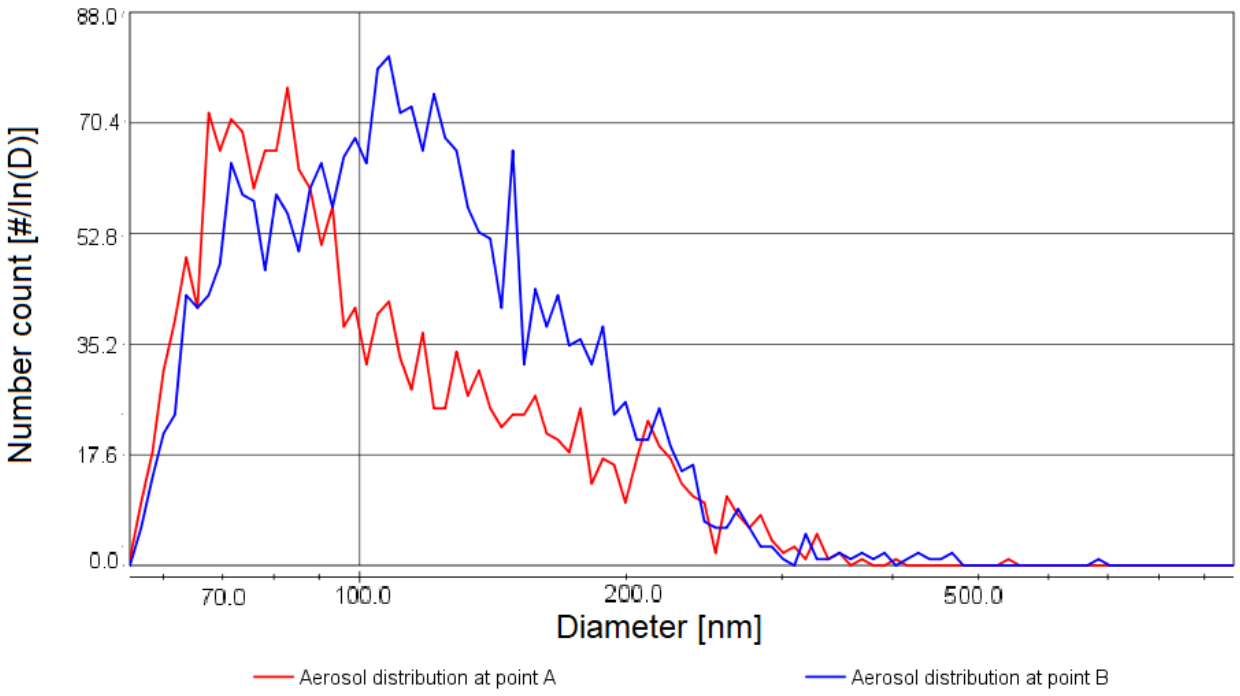

Figure 5.12: Aerosol number distribution by diameter (logarithmic bin sizes). At point B, the distribution has more accumulation particles. Points A and B refer to readings on July 27 at times indicated in **Figure 4.13.**

Another tool that allows us to characterise aerosol fluxes is examination of the size-resolved particle mass deposition, plotted in **Figure 4.13.** Size-resolved particle measurements allow

us to determine possible ages for aerosols. For example, the larger median particle size at point B suggests an aged, chemically mature plume, whereas at point A, the smaller median particle size deposited suggests a younger plume that is coagulating and chemically evolving (Nikonovas et al., 2015). **Figure 5.12** shows a comparison of the size distribution of particles at points A and B.

There was a significant deposition event on the morning of July 27. Aerosols were deposited over the course of 1.5 hours. **Figure 5.5** shows the particle concentration in the canopy as measured by the particle counters along with the wind direction at 31 m. At 09:35, the aerosol number concentration increased sharply for 15 minutes then decreased. It immediately increased again for 30 minutes. 15 minutes after that ended, a third peak of high particle concentration was sustained for 15 minutes before dropping back to its original value. This episode, unlike the smaller episodes of deposition preceding it, was broad in particle size distribution, with a nearly uniform mass of particles deposited between diameters 100 nm and 500 nm.

The likely origin for this plume is Syncrude. Its smoke stacks emit among the most particulate matter and volatile organic compounds in the area (ECCC 2016), and the wind shifted to its direction during the deposition episode. The time-integrated eddy-covariance particle flux into the forest over the course of the 1.5 h long deposition episode was 0.15 $\mu g/m^2$. If we assume that this quantity was distributed evenly inside the canopy, we find that 9.4 ng/m^3 of additional particulate matter was deposited to the forest during the event. This is a small amount compared to the ambient particulate matter mass concentration within the canopy. This indicates that most aerosol flux into the forest was not through vertical turbulent flux. It is possible that horizontal flux into the footprint area could be responsible for the elevated particulate matter concentrations during this episode.

5.4 Upward aerosol fluxes

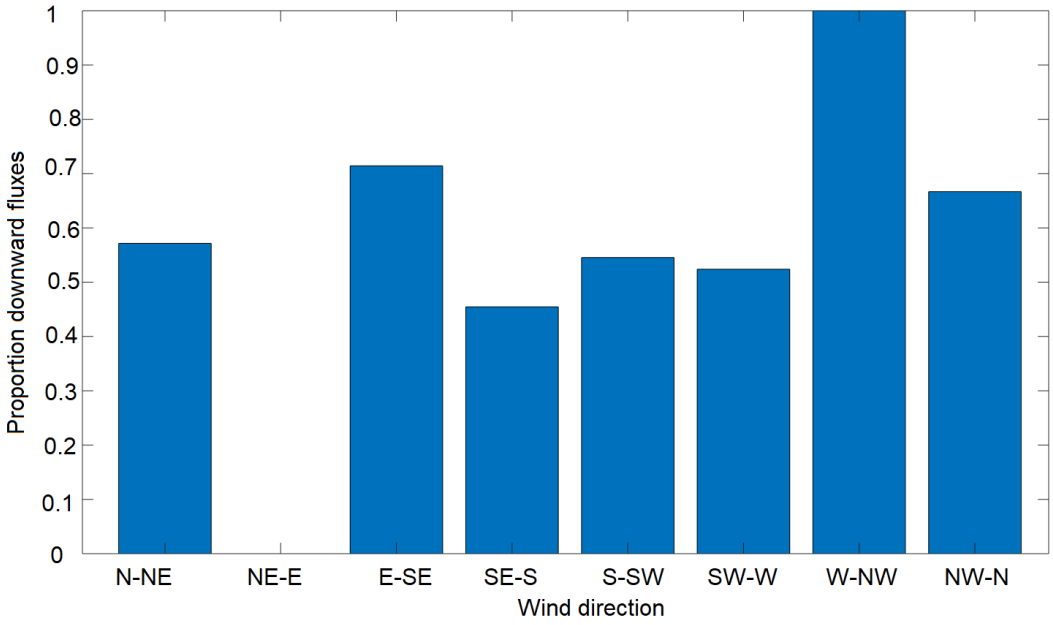

Figure 5.13: Proportion downward flux by wind angle during the intensive field campaign. NE to E bin empty due to lack of data.

In Gordon et al. (2011), fluxes were observed to be upward 60% of the time in a mixed forest in Southern Ontario. During the YAJP campaign in a jack pine forest, particle fluxes were upward a significant amount of the time as well, 82 averaging periods out of 182 periods that had enough turbulence for eddy covariance to be valid. That is, 45% of valid eddy covariance periods had a net upward flux.

Upward fluxes were more prevalent when the wind was blowing from certain directions. Referring to **Figure 5.13**, south to southeast winds are associated with upward fluxes a majority of the time. There are few industrial operations in that direction so fewer downward fluxes are expected, but one would expect more upward fluxes from due west, for example, where there are no smoke stacks.

A significant upward flux episode was present during the

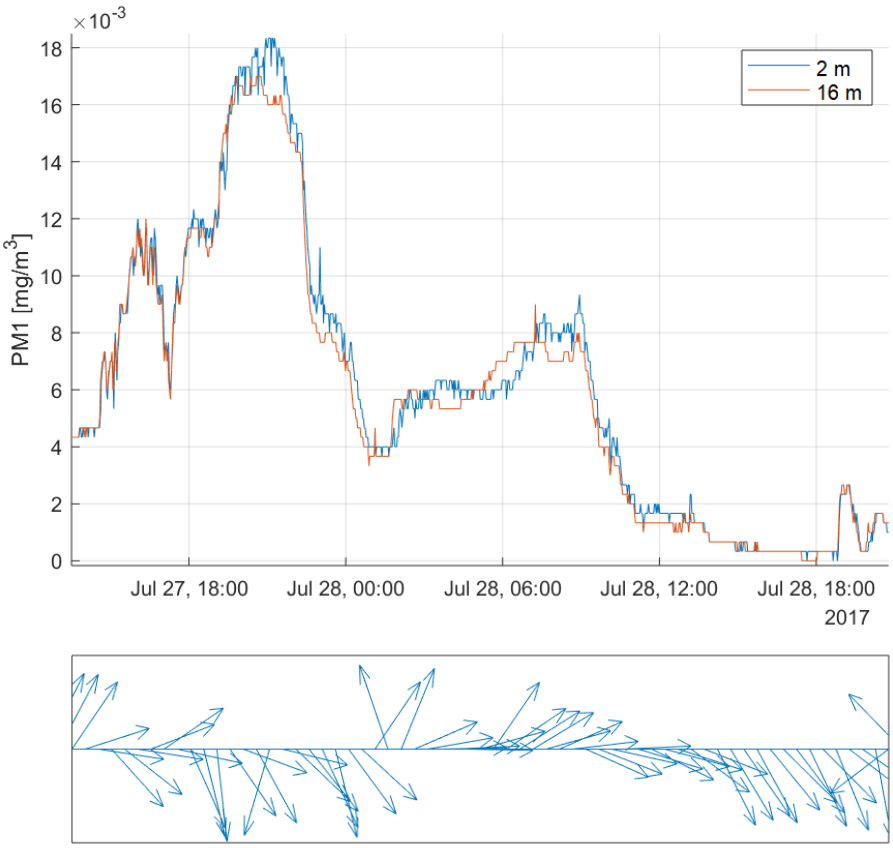

Figure 5.14: Particulate matter concentration and wind direction during and after the upward flux episode.

later half of July 27. The magnitude of this event was almost as large as the downward flux that preceded it. During the event (**Figure 5.14**), the particulate matter concentration in the canopy increased and attained a peak at 16:00. It dropped back down after one hour to its original value but proceeded to rise to 17 $\mu g/m^3$, a concentration greater than occurred during the deposition episode prior. It stayed at that concentration for three hours before dropping over the course of 4 hours to 3 $\mu g/m^3$. After the event, the particulate matter concentration reached zero in the canopy, on the afternoon of July 28, and briefly maintained that level before increasing to a baseline value of 2.5 $\mu g/m^3$.

A likely reason for the upward fluxes is that the concentration of particulate matter within the canopy sometimes exceeded the concentration above, perhaps due to the storage of particles. The source of the higher concentrations in the forest could be due to several factors. For one, clean air could have advected over the site while polluted air stayed in the canopy. However, the wind direction during the upward flux event was north to northwest, which during other periods of the campaign have been associated mainly with downward fluxes. Also, this does not explain why the concentration of particles increased during the upward flux event.

The upward flux episode discussed can also be due to a low plume vertically expanding as it is advected into the forest. It is possible that, if the plume fumigated below the forest canopy, it would advect into the footprint of the YAJP tower, where it would cause an upward aerosol flux. Unfortunately, there are no further indicators to tell if a new plume was continually advected into the forest.

Also possible is a source within the forest. It could stem from the growth of the particles deposited from the previous episode. UHSAS data show that throughout the upward flux episode, the median particle size increased from 110 nm to 180 nm in

diameter (**Figure 4.10**) while mass increased significantly (**Figure 4.11**). The addition of biogenic volatile organic compounds and secondary biogenic aerosols to deposited aerosols could increase the mass of aerosols detectable to our instruments.

It is unlikely that the aerosols in this upward flux episode were formed de novo from biogenic sources. Biogenic aerosols usually form from the nucleation of organic gases. They grow into larger aerosols by combining with each other or with organic gases. They would be too small to register with the campaign's instruments until they had grown to 55 nm in diameter. Such a process takes about 12 hours to grow particles to a detectable size, and usually does not produce particles of diameter greater than 100 nm (eg. Allan et al., 2006). Thus, this mechanism is not a good candidate for the increase in particulate matter mass observed in the study.

5.5 Deposition velocity of aerosols

Deposition velocity is an important parameter in many models of aerosol deposition to canopies. It relates fluxes and concentration gradients for a given species and a given canopy type. It is given by $v_d = -F/C$, where F is flux and C is concentration. Typical values observed for particles 55–1000 nm in a forest canopy are between 1 mm/s and 1 cm/s (e.g. Hicks et al., 2016).

In **Figure 5.15** is a plot of v_d against particle diameter for the study period. **Figure 5.16** shows the same information considering downward fluxes only. There is a minimum at around 200 nm in particle diameter. The increase moving into the lower particle size range is not as great as expected, with v_d increasing only by 13% before falling again around 70 nm in particle diameter. The likely reason is that the UHSAS fails to count approximately 50% of particles of size 60 nm and even fewer at smaller sizes (Cai et al., 2008), whereas it captures a significantly higher proportion of particles at larger sizes.

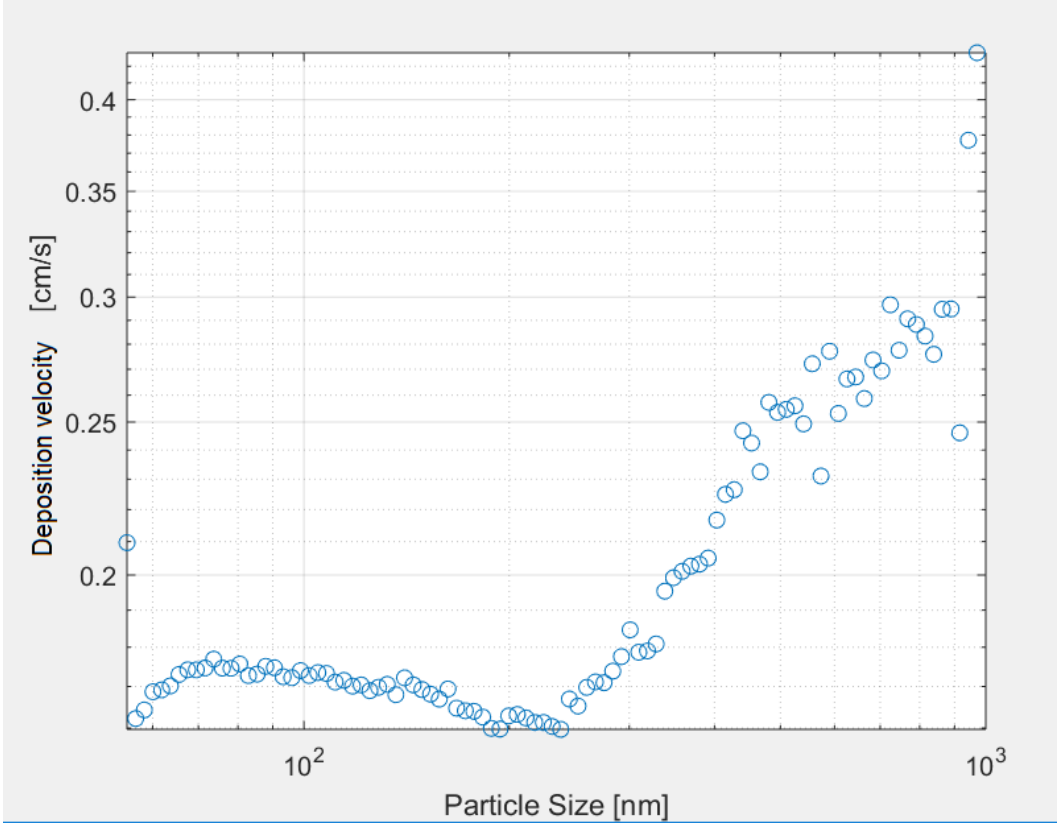

Figure 5.15: Deposition velocity as a function of particle diameter. Includes both upward and downward fluxes. Note the local minimum.

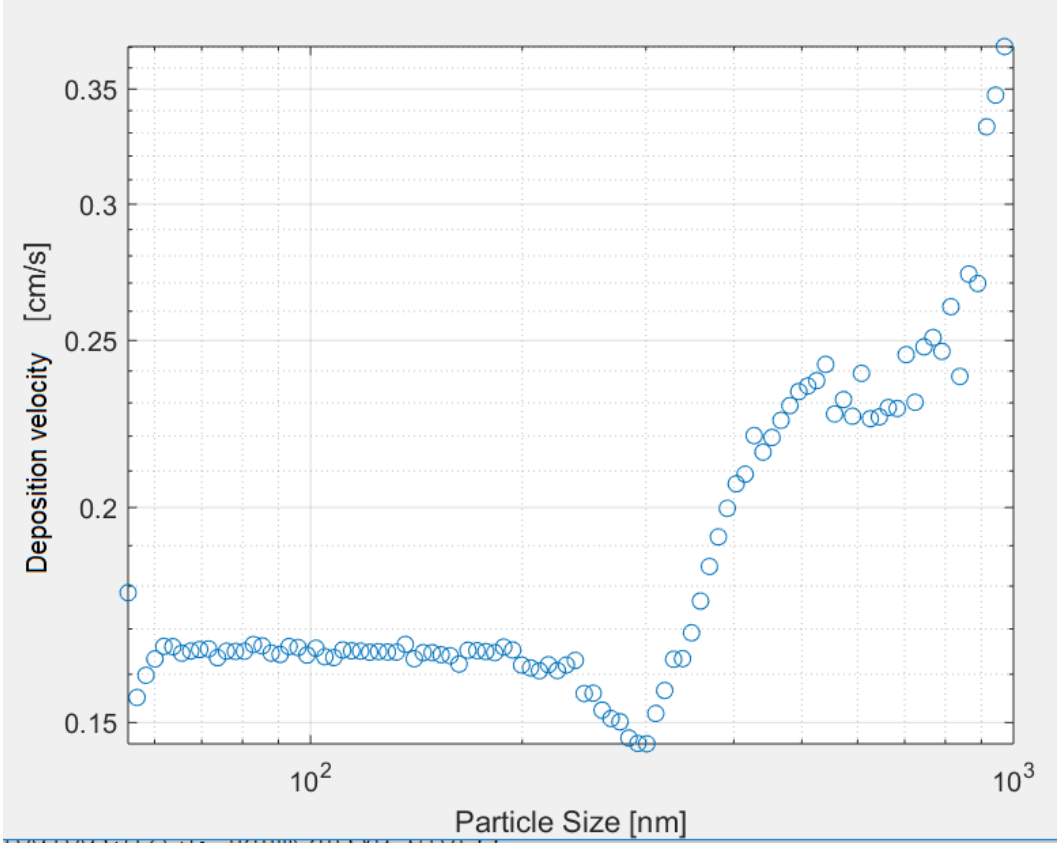

Figure 5.16: Deposition velocity as a function of particle diameter. Includes downward fluxes only.

Petroff et al. (2008) show that existing models (e.g. Zhang et al., 2001; Slinn, 1982) exhibit a local minimum of the deposition velocity of aerosols with particle diameter, but the spread of values among different studies and canopies is substantial. Two models (Davidson et al., 1982, and Petroff et al., 2008) have the minimum in deposition velocity of 2 mm/s at around 150 nm for a forest canopy, similar to the YAJP site, although their model inputs assume a shorter canopy with more foliage.

Observations of deposition velocity at the YAJP site match well with other studies in coniferous forests. For example, in the size range > 100 nm, the data in **Figure 5.15** correspond well with, eg., Gallagher et al. (1997), where observations were made in a spruce forest with h_c = 17 m. Observational data for v_d are scarce at sizes under 100 nm over forests, but Gaman et al. (2004) observed similar deposition rates in a pine forest of particles size 40–100 nm.

Hicks et al. (2016) note in their review that studies in forests exhibiting the minimum in v_d are scarce. However, a minimum in deposition velocity around a particle diameter of 90 nm was observed in Mammarella et al. (2011) in a coniferous Scots pine (Pinus sylvestris) forest. Condensational particle counters collected 5 years of size-resolved particle concentration measurements for eddy covariance flux calculations. Local minima of aerosol deposition velocity with respect to particle diameter were measured at 90 nm and 150 nm. The average deposition velocities in these bins were 1.8 mm/s and 1.9 mm/s respectively, higher values than the minimum of 1.6 mm/s observed at the YAJP site.

6 Conclusions

Eddy covariance measurements of size-resolved particle flux 55-1000 nm were made at $2h_c$ in a sparse jack pine forest in July 2017 in the Oil Sands region of northern Alberta, a region with anthropogenic emissions of aerosols and volatile organic compounds. Also, eddy covariance measurements of H_2O and CO_2 gas fluxes were made at $2h_c$ and $0.3h_c$. High-frequency turbulence measurements were made at $0.3h_c$, $0.6h_c$, and $2h_c$. To supplement high-frequency particle flux and concentration measurements, 2-minute particle mass concentration data were collected at $z = h_c$ and $z = 0.1h_c$.

Over the course of the field campaign, some periods of high particle concentration and deposition into the forest were observed. For example, on July 27, a deposition episode occurred at the YAJP site. During the deposition episode, particulate matter concentrations spiked three times in the span of 90 minutes and rapidly mixed to ground level. The deposition episode was immediately proceeded by an upward flux episode.

At the YAJP site, particle fluxes were upward 45% of the time. This was comparable to Pryor et al. (2011) who observed upward fluxes more than one third of the time, but less than Gordon et al. (2011), who observed upward fluxes 60% of the time. Oftentimes, like on July 27, these fluxes were caused by the clearing out of aerosols stored in the forest from an earlier deposition episode.

Eddy covariance CO_2 flux measurements made during the intensive field campaign are consistent with the results of previous flux studies in forests (e.g. Malhi et al., 1999). Momentum flux values were consistent with other forests (e.g. Bailey et al. eds., 1997). Sensible and latent heat flux values were reasonable but differed from another study in a boreal forest, Jarvis et al. (1997), where the Bowen ratio was lower.

Finally, it was found that forests are decoupled most of the time, meaning aerosols within are stored until mixing occurs.

Mixing was usually due to daytime instability. With nighttime stratification, aerosol concentrations took longer to mix. For example, aerosols took less than two minutes to mix down to the ground from 16 m during the day but took close to an hour to mix during the night.

A minimum in v_d for aerosols with respect to particle diameter, which has been theorised for decades (e.g. Slinn, 1982, c.f. Petroff et al., 2008b) but was only recently observed in a forest (Mammarella et al., 2011), was observed at the YAJP site during the study period. To the author's knowledge, this study is the first to measure v_d for aerosols, an important parameter in modeling deposition of aerosols to forests (Hicks et al., 2016), in the boreal jack pine forest.

Some results like the deposition velocity and gas flux measurements will be useful in models of boreal forests. Some other results, like the spectra and co-spectra, serve as verification of the validity and usefulness of the YAJP forest site. Finally, the effect of the canopy on mixing and deposition was explored. It was found that, depending on the state of coupling within the canopy, the mixing of aerosols and gases was impeded by the presence of the canopy.

The particle size distribution of aerosol plumes was investigated and suggested properties of each plume, such as age. However, we did not examine the composition of aerosols at our site. Therefore, it was not possible to ascertain as to the amount of organic matter in aerosols. A future manuscript will examine the data collected during the June 2018 campaign, which feature [SO_2] measurements, a species emitted primarily by anthropogenic sources (EPA 2018).

References

Adams, E. E. (2012). World Forest Area Still on the Decline. *Earth Policy Institute* <http://www.earth-policy.org/indicators/C56/forests_2012>

Addison, P. A., & Puckett, K. J. (1980). Deposition of atmospheric pollutants as measured by lichen element content in the Athabasca oil sands area. *Canadian Journal of Botany, 58*(22), 2323-2334.

Ahlm, L., et al. (2010). Emission and dry deposition of accumulation mode particles in the Amazon Basin. *Atmospheric Chemistry and Physics*, *10*(21), 10237-10253.

Allan, J. D., et al. (2006). Size and composition measurements of background aerosol and new particle growth in a Finnish forest during QUEST 2 using an Aerodyne Aerosol Mass Spectrometer. *Atmospheric Chemistry and Physics*, *6*(2), 315-327.

Amiro, B. D. (1990). Drag coefficients and turbulence spectra within three boreal forest canopies. *Boundary-Layer Meteorology*, *52*(3), 227-246.

Applied Technologies, Inc. (n.d.). *Operator's Manual for a Three Axis Sonic Anemometer/Thermometer*. Longmont, CO.

Aubinet, M., et al. (Eds.). (2012). *Eddy Covariance: A Practical Guide to Measurement and Data Analysis.* Dordrecht: Sprinter.

Bailey, W., et al. (Eds.). (1997). *Surface Climates of Canada*. Montréal: McGill-Queen's University Press.

Baldocchi, D. D., et al. (1997). Seasonal variation of energy and water vapor exchange rates above and below a boreal jack

pine forest canopy. *Journal of Geophysical Research, 102*(D24), 28939-28951.

Burba, G. (2013). *Eddy covariance method for scientific, industrial, agricultural and regulatory applications: A field book on measuring ecosystem gas exchange and areal emission rates*. Lincoln: LI-Cor Biosciences.

Cai, Y., et al. (2008). Performance characteristics of the ultra high sensitivity aerosol spectrometer for particles between 55 and 800 nm: Laboratory and field studies. *Journal of aerosol science*, *39*(9), 759-769.

Canadian Council of Forest Ministers (2017). Overview: Canada's Forests <http://www.sfmcanada.org/en/canada-s-forests>

Carson, D. J. (1982). Current parametrizations of land-surface processes in atmospheric general circulation models. In *Land Surface Processes in Atmospheric General Circulation Models*, ed. P. S. Eagleson, 67-108. Cambridge: Cambridge University Press.

Cinlar, E. (1975). *Introduction to Stochastic Processes*. Englewood Cliffs: Prentice Hall.

d'Andrea, S. D., et al. (2013). Understanding global secondary organic aerosol amount and size-resolved condensational behavior. *Atmos. Chem. Phys.*, **13**, 11519-11534.

Davidson, C. I., et al. (1982). The influence of surface structure on predicted particle dry deposition to natural grass canopies. In *Long-Range Transport of Airborne Pollutants*, ed. H. C. Martin, 25-43. Dordrecht: Springer.

Denmead, O. T., & Bradley, E. F. (1985). Flux-gradient relationships in a forest canopy. In *The forest-atmosphere interaction*. Dordrecht: Springer.

Droplet Measurement Technologies <dropletmeasurement.com>

(ECCC 2016) Environment and Climate Change Canada, & Alberta Environment and Parks (2016). Joint Oil Sands Monitoring Program Emissions Inventory Compilation Report. Edmonton: Her Majesty the Queen in right of the Province of Alberta.

(EPA 2018) United States Environmental Protection Agency (2018). Sulfur Dioxide Basics. <https://www.epa.gov/so2-pollution/sulfur-dioxide-basics>

Evans, J. (Ed.). (2008). *The Forests Handbook, Volume 1*. Oxford: Blackwell Science.

Finnigan, J. (2000). Turbulence in plant canopies. *Annual review of fluid mechanics*, *32*(1), 519-571.

Foken, T. (2008). *Micrometeorology*. Berlin: Springer.

Gallagher, M. W., et al. (1997). Measurements of aerosol fluxes to Speulder forest using a micrometeorological technique. *Atmospheric Environment*, *31*(3), 359-373.

Gaman, A., et al. (2004). Relaxed eddy accumulation system for size-resolved aerosol particle flux measurements. *Journal of Atmospheric and Oceanic Technology*, *21*(6), 933-943.

Garratt, J. R. (1992). *The atmospheric boundary layer*. Cambridge: Cambridge University Press.

Gordon, M. (2013). *Biogenic Emissions, Modeling of the Boreal Forest in Northern Alberta*. (Report No. KM062-12-1133 4(2)).

Gordon, M. et al. (2011). Aerosol flux measurements above a mixed forest at Borden, Ontario. *Atmos. Chem. Phys.,* **11**, 6773-6786.

Gordon, M., et al. (2015). Determining air pollutant emission rates based on mass balance using airborne measurement data over the Alberta oil sands operations. *Atmospheric Measurement Techniques*, *8*(9), 3745-3765.

Grünwald, T., & Bernhofer, C. (2007). A decade of carbon, water and energy flux measurements of an old spruce forest at the

Anchor Station Tharandt. *Tellus B: Chemical and Physical Meteorology*, *59*(3), 387-396.

Hicks, B. B., et al. (2016). Dry deposition of particles to canopies – A look back and the road forward. *J. Geophys. Res. Atmos.,* **121**:14691-14707.

Jarvis, P. G., et al. (1997). Seasonal variation of carbon dioxide, water vapor, and energy exchanges of a boreal black spruce forest. *Journal of Geophysical Research*, *102*(D24), 28953-28966.

Kaimal, J. C., & Finnigan, J. J. (1994). *Atmospheric boundary layer flows: Their structure and measurement*. New York: Oxford University Press.

Kelley, E. N., et al. (2009). Oil sands development contributes polycyclic aromatic compounds to the Athabasca River and its tributaries. *Proc. Natl. Acad. Sci. U.S.A., 106*(52), 22346-22351.

Kulmala, M., et al. (2001). Overview of the international project on biogenic aerosol formation in the boreal forest (BIOFOR). *Tellus B*, *53*(4), 324-343.

La Roi, G. H. (2018). Boreal zone. *The Canadian Encyclopedia*. Historica Canada. <https://www.thecanadianencyclopedia.ca/en/article/boreal-forest>.

LI-COR, Inc. (2016). *LI-7500RS*. Lincoln, NE.

Liggio, J., et al. (2016). Oil sands operations as a large source of secondary organic aerosols. *Nature*, *534*(7605), 91-94.

Malhi, Y., et al. (1999). The carbon balance of tropical, temperate and boreal forests. *Plant, Cell and Environment*, **22:**715-740.

Mammarella, I., et al. (2011). Long-term aerosol particle flux observations. Part II: Particle size statistics and deposition velocities. *Atmospheric Environment*, **45**:3794-3805.

Matsuda, K. (2017). Dry deposition of aerosols onto forest. In *Air Pollution Impacts on Plants in East Asia*, ed. T. Izuta, 309-322. Tokyo: Springer.

Nikonovas, T., et al. (2015). Smoke aerosol properties and ageing effects for northern temperate and boreal regions derived from AERONET source and age attribution. *Atmospheric Chemistry and Physics*, **15**:7929-7943.

Nilsson, E. D., et al. (2001). Effects of continental boundary layer evolution, convection, turbulence and entrainment, on aerosol formation. *Tellus B: Chemical and Physical Meteorology*, *53*(4), 441-461.

Oke, T. R., et al. (2017). Urban Climates. Cambridge: Cambridge University Press.

Petroff, A., et al. (2008a). Aerosol dry deposition on vegetative canopies. Part I: review of present knowledge. *Atmospheric Environment*, *42*(16), 3625-3653.

Petroff, A., et al. (2008b). Aerosol dry deposition on vegetative canopies. Part II: A new modelling approach and applications. *Atmospheric Environment*, *42*(16), 3654-3683.

Pryor, S. C., et al. (2013). Size-resolved particle fluxes and vertical gradients over and in a sparse pine forest. *Aerosol Science and Technology, 47*(11),1248-1257.

Rissler, J. et al. (2014). Effective Density and Mixing State of Aerosol Particles in a Near-Traffic Urban Environment. *Environ. Sci. Technol., 48*(11), 6300-6308.

Rivas, I. et al. (2017). Identification of technical problems affecting performance of DustTrak DRX aerosol monitors. *Science of the Total Environment*, **584-585**:849-855

Rosner, D. E. et al. (1992). Effects of heat transfer on the dynamics and transport of small particles suspended in gases. *Ind. Eng. Chem. Res.,* **31:**760-769

Rosner, D. E. and Tassopoulos, M. (1991). Correction for sampling errors due to coagulation and wall loss in laminar and turbulent tube flow: direct solution of canonical 'inverse' problem for log-normal size distributions. *Journal of Aerosol Science* **22**:7 843-867

Ross, S. M. (2011). *Introduction to Probability Models.* Oxford: Elsevier.

Rotenberg, E. (2013). Solving the energy dissipation riddle in Yatir. *FluxLetter*, *5*(2), 12-14.

Schotanus, P., et al. (1983). Temperature measurement with a sonic anemometer and its application to heat and moisture fluctuations. Boundary Layer Meteorology **26**:81–93

Sehmel, G. A., & Hodgson, W. H. (1978). *Model for predicting dry deposition of particles and gases to environmental surfaces* (No. PNL-SA-6721; CONF-780611-10). Battelle Pacific Northwest Labs., Richland, WA (USA).

Seinfeld, J. H., & Pandis, S. N. (2006). *Atmospheric chemistry and physics*. Hoboken: Wiley.

Shuttleworth, W. J. (1984). Observations of radiation exchange above and below Amazonian forest. *Q.J.R. Meteorol. Soc.*, **110**:1163-1169.

Sinclair, D., & La Mer, V. K. (1949). Light scattering as a measure of particle size in aerosols: The production of monodisperse aerosols. *Chem. Rev., 44*(2), 245-267.

Slinn, W. G. N. (1982). Predictions for particle deposition to vegetative canopies. *Atmospheric Environment, 16*(7), 1785-1794.

Stull, R. B. (1988). *An introduction to boundary layer meteorology*. Dordrecht: Kluwer Academic Publishers.

Tennekes, H., & Lumley, J. L. (1972). *A first course in turbulence*. Cambridge: MIT press.

Thomas, C., & Foken, T. (2007). Flux contribution of coherent structures and its implications for the exchange of energy and matter in a tall spruce canopy. *Boundary-Layer Meteorol.* **123:**317-337.

Unsworth, M. H, et al. (2004). Components and Controls of Water Flux in an Old-growth Douglas-fir–Western Hemlock Ecosystem. *Ecosystems, 7*(5), 468-481.

Viana, M., et al. (2015). Field comparison of portable and stationary instruments for outdoor urban air exposure assessments. *Atmospheric Environment,* **123**:220-228.

Wang, X., et al. (2009). A novel optical instrument for estimating size segregated aerosol mass concentration in real time. *Aerosol Science and Technology, 43*(9), 939-950.

(WBEA 2018) Wood Buffalo Environmental Association. <wbea.org>

Webb, E. K., et al. (1980). Correction of the flux measurements for density effects due to heat and water vapour transfer. *Quarterly Journal of the Royal Meteorological Society*, **106**:85-100.

Wernert, S. J., ed. (1982). *North American Wildlife*. Pleasantville: Reader’s Digest Association.

Wesely, M. L. and Hicks, B. B. (1977). Some factors that affect the deposition rates of sulfur dioxide and similar gases on vegetation. *J. Air Pollut. Contr. Assoc.* **27**:1110-1116.

Whitehead, J. D., et al. (2010). Aerosol fluxes and dynamics within and above a tropical rainforest in South-East Asia. *Atmos. Chem. Phys.* **10**:9369-9382.

Wilczak, J. M., et al. (2001). Sonic anemometer tilt correction algorithms. *Boundary-Layer Meteorology*, *99*(1), 127-150.

Wolf, A. and Laca, E. A. (2007). Cospectral analysis of high frequency signal loss in eddy covariance measurements. *Atmos. Chem. Phys. Discuss.* **7**:13151-13173.

Yakir, D. (2013). The Yatir forest: Postcards from the edge. *FluxLetter*, *5*(2), 9-11.

Zhang, L., et al. (2001). A size-segregated particle dry deposition scheme for an atmospheric aerosol module. *Atmospheric Environment*, *35*(3), 549-560.

Appendix A Sites

Table A1: Coordinates of meteorological and air quality monitoring tower sites mentioned in this manuscript.

Location	Latitude	Longitude
AMS 13	57°8′ 57" N	111°38′ 32" W
AMS 19	57°14′ 23" N	110°53′ 53" W
AMS 23	57°20′ 56" N	111°38′ 23" W
JP 104	57°7′ 8" N	111°25′ 32" W
YAJP	57°7′ 21" N	111°25′ 35" W